ABSTRACT

Title of dissertation: DFT AND RELATED MODELING OF POST-SILICON VALENCE 4 MATERIALS: SiC AND Ge

Christopher Darmody, 2020

Dissertation directed by: Dr. Neil Goldsman
Department of Electrical and Computer Engineering

Though silicon (Si) is in many ways the material of choice for many electronic applications due in part to its mature processing technology, its intrinsic properties are not always suited for every challenge. Specialized high power and high temperature devices benefit from using semiconductors with a larger band-gap and higher thermal conductivity such as silicon carbide (SiC). Additionally, the 1.1eV bandgap of Si makes it unable to effectively absorb infrared photons so a material with a smaller bandgap, like germanium (Ge), is more suited to the task.

Currently SiC power transistors are commercially available but suffer from poor channel mobility due to interface roughness which limits their performance. To predict the maximum theoretically achievable mobility for different crystallographic interfaces I developed a novel technique for extracting an atomic-roughness scattering rate from an arbitrary atomic surface. The term atomic-roughness here means an interface purely due to the variation of atom species and position without the presence of a crystallographic miscut due to epitaxial growth considerations.

I used Density Functional Theory (DFT) to obtain a perturbation potential from which I can calculate a scattering rate. This scattering rate can then be used in a Monte Carlo simulation to predict mobility for a given field configuration.

In addition to SiC's low channel mobility, SiC p-type dopant species also exhibit an abnormally large ionization energy compared to its n-type dopants and to the primary dopants in many other semiconductors. This fact can cause issues such as unexpectedly high resistance regions at lower operating temperatures - causing the need to dope at significantly higher concentration. To characterize the incomplete ionization fraction p/N_A, I first gathered nearly all existing published data on the ionization energy of aluminum (Al) in 4H-SiC and created an empirical concentration-dependent model of this function. Then I put together a physics-based model of the entire acceptor and valence band system and used my concentration-dependent ionization energy as an input to predict p/N_A. I verify my physics-based model result against a separate experimental dataset derived from nearly-exhaustive literature measurements of Hall mobility and resistivity. Finally, I transform fully temperature-dependent result of p/N_A from a complex numerical computation to a more easily implementable parameterized function with the use of a genetic algorithm.

The remaining part of my work was performed on Germanium which has interesting application in short-wave infrared imaging due its 0.66eV indirect and 0.85 eV direct bandgaps, which corresponds closely to the peak illumination of the "night glow" at 0.75 eV. Optical devices greatly benefit from direct gap band structures to increase photon absorption and emission efficiency. Though Ge is an

indirect gap material, it can be alloyed with a direct gap material, namely tin (Sn), to transition it to a direct gap material at a certain molar fraction. Through DFT calculations I investigate the nature of this transition and determine theoretically the minimum molar fraction needed to achieve a direct bandgap.

DFT AND RELATED MODELING OF POST-SILICON VALENCE 4 MATERIALS: SiC AND Ge

by

Christopher Darmody

Dissertation submitted to the Faculty of the Graduate School of the
University of Maryland, College Park in partial fulfillment
of the requirements for the degree of
Doctor of Philosophy
2020

Advisory Committee:
Professor Neil Goldsman, Chair/Advisor
Professor Aristos Christou
Professor Kevin Daniels
Professor Romel Gomez
Professor Agisilaos Iliadis

Dedication

To my loving parents, James and Jacquie.

Acknowledgments

I would first and foremost like to express my eternal gratitude to my advisor Dr. Neil Goldsman for his years of support, encouragement, and insightful discussions. Without your guidance I would not be where I am today.

Thank you to my thesis defense committee: Dr. Kevin Daniels, Dr. Romel Gomez, Dr. Agis Iliadis, and Dr. Aristos Christou for taking time away from your busy schedules to participate in this important step in my academic life. I would also like to thank Dr. John Melngailis for introducing me to the world of device physics which has become the basis of my graduate studies.

I am also grateful to have had such a great group of colleges and friends who have made my graduate school experience such a joy - Ittai Baum, Yumeng Cui, Xiyang Xiao, Alex Mazzoni, Franklin Nouketcha, Dev Ettisserry, Peiwen He, and Eric Krokos.

Lastly, I would like to thank my family for their loving support. Thanks Mom and Dad for always believing in me.

Table of Contents

List of Tables

List of Figures

List of Abbreviations

μ	Mobility
ν	Velocity
ρ	Mass Density
$\rho(E)$	Density of States (DoS)
n	Mobile Electron Density
p	Mobile Hole Density
N_D	Donor Concentration
N_D^+	Ionized Donor Concentration
N_D^0	Unionized Donor Concentration
N_A	Acceptor Concentration
N_A^-	Ionized Acceptor Concentration
N_A^0	Unionized Acceptor Concentration
E_F	Fermi Energy
ϕ	Single-Electron Wavefunction
Ψ	All-Electron Wavefunction
$\psi_{\mathbf{k}}$	Single-Electron Time-Independent Wavefunction
$\Psi_{\mathbf{k}}$	Single-Electron Temporally and Spatially Dependent Wavefunction
Ai[z]	Airy Function
CMOS	Complimentary Metal-Oxide-Semiconductor
DD	Drift-Diffusion
DFT	Density Functional Theory
DMOS	Doubly-diffused Metal-Oxide-Semiconductor (Transistor)
FET	Field Effect Transistor
GaN	Gallium Nitride
Ge	Germanium
MC	Monte Carlo
MOSFET	Metal-Oxide-Semiconductor Field Effect Transistor
SiC	Silicon Carbide
SiO_2	Silicon Dioxide
Sn	Tin

Chapter 1: Introduction

1.1 Post Silicon Materials

As silicon nears the end of its road map, the semiconductor industry is looking to other materials to continue technological scaling. Despite silicon's many good properties, other less mature materials exist which exhibit better performance in certain regimes. In particular, for high speed integrated circuits electron mobility is the key figure-of-merit which dictates how fast electrons can move within the material. Though the mobility of Si is fairly high, it is surpassed by materials like GaAs and Ge. High mobility materials also facilitate device scaling by allowing physically smaller devices to maintain reasonable ON currents in transistors.

Additionally, Si has a relatively small bandgap among semiconductors regularly researched (Figure 1.1 [3]). Small bandgap materials perform poorly in high temperature and high power applications due to their large intrinsic carrier concentrations which can overwhelm doped carrier distributions and small critical fields which cause avalanche breakdown respectively. One popular wide bandgap material choice is SiC, which boasts not only a large bandgap value, but a higher thermal conductivity than Si, while still being able to grow a native oxide. Research of SiC power devices has been taking place since the 1990s and commercial devices have

been available to consumers since 2003 [13]. Further research is currently being done to improve reliability and performance. Current SiC devices suffer from the presence of interface traps which cause threshold voltage instability [14, 15] as well as surface roughness which decreases channel mobility [1, 14].

In this thesis, I will first discuss my contribution to the study of SiC surface mobility and will follow with a discussion of my atomistic calculations of Ge-Sn alloys. In short, my work involves employing density function theory (DFT) to solve the many-body Schrdinger equation which tells me the electron density and potential everywhere within my constructed crystal systems as well as the band structure. I have created a novel method to extract a perturbation potential due to defects and/or the presence of an interface from this DFT solution. I then calculate what we refer to as an atomic-roughness scattering rate using the calculated atomic-level perturbation potential which is then fed into a Monte Carlo simulation. The Monte Carlo simulation builds up electron velocity and energy distributions due to different scattering rates within a semiconductor and provides as output a field-based mobility. By using this atomic-roughness scattering we avoid approximations typically used when calculating theoretical mobilities in SiC.

The DFT solution to the many-body Schrdinger equation also provides a band structure for the given system. I use this band structure to predict the transition of Ge into a direct-gap material when alloyed with Sn.

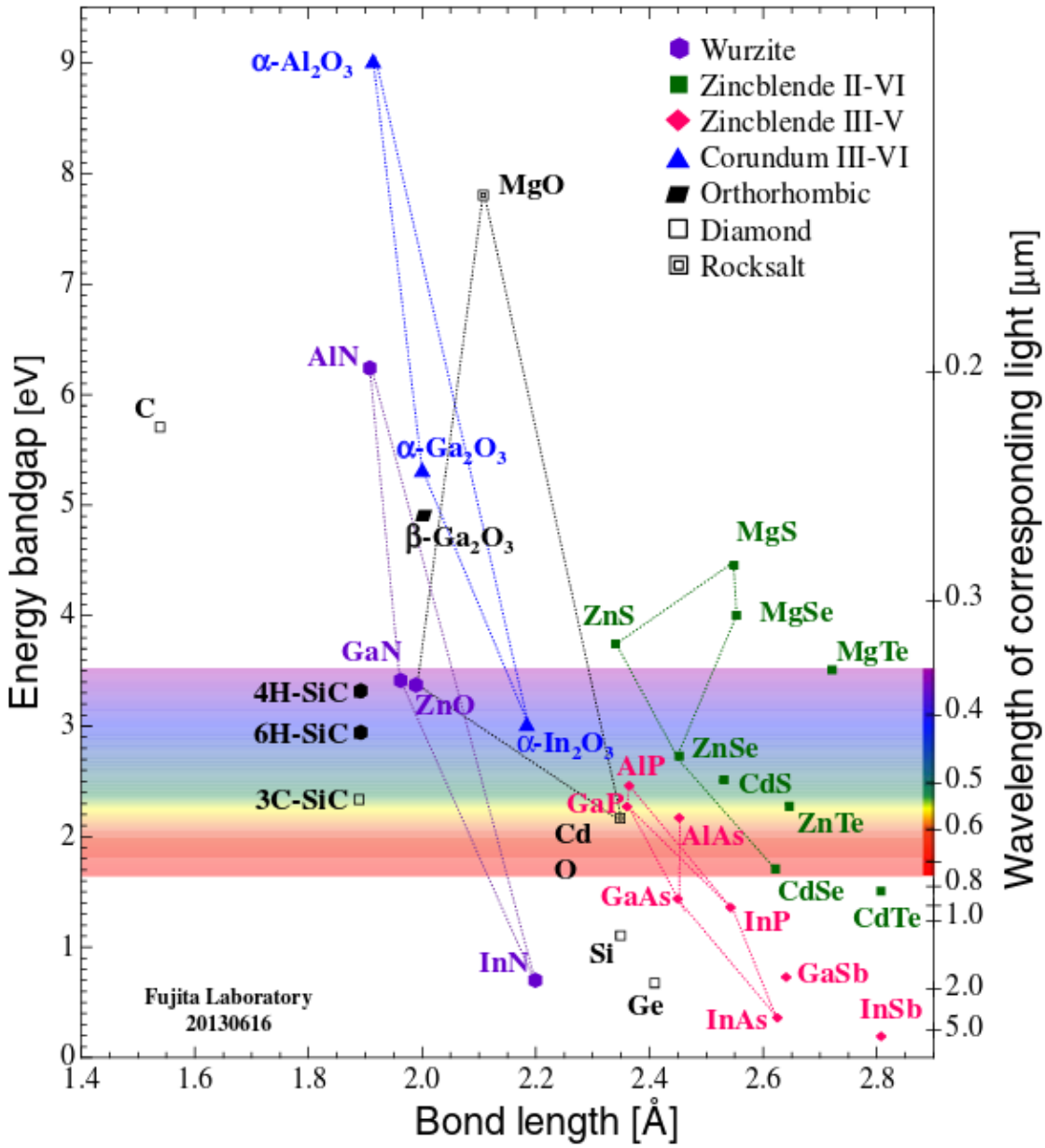

Figure 1.1: Plot of popular semiconductor elements and compounds relating atomic bond length to energy bandgap. The scatter data shows a general trend of smaller bond distances correlate to larger bandgaps. (Figure from [3])

1.2 Overview of Group IV(a) Semiconductors

1.2.1 Properties

Both silicon and germanium are good candidates for integrated electronics due to their ability to thermally grow a native oxide. This allows for the creation of good interfaces with few defects to be used for MOSFET gate oxides, beneath which the sensitive channel resides. The compound semiconductor silicon carbide can also grow a native oxide but it is known to be much more defected due in part to the presence of carbon which must leave the material during the oxidation process.

Elements and compounds higher in a given column of the periodic table (Figure 1.2) tend to have larger bandgaps and decrease as you descend in the column. Large bandgap materials are excellent candidates for high power and high temperature devices because of their large breakdown electric fields and their low intrinsic carrier concentrations respectively. On the other end of the spectrum, small bandgap materials perform poorly in these situations, they tend to have increased mobility which lends them to use in low power and high speed integrated circuits.

Table 1.1 lists various electrical and material properties of the important column IV semiconductors. The materials in the table are arranged from left to right as they appear descending in the periodic table. Different properties tend to increase or decrease across this table, almost without exception, which is a result commonly seen in the periodic table arrangement of the elements. In essence, wide bandgap materials have larger thermal conductivity and breakdown fields, while

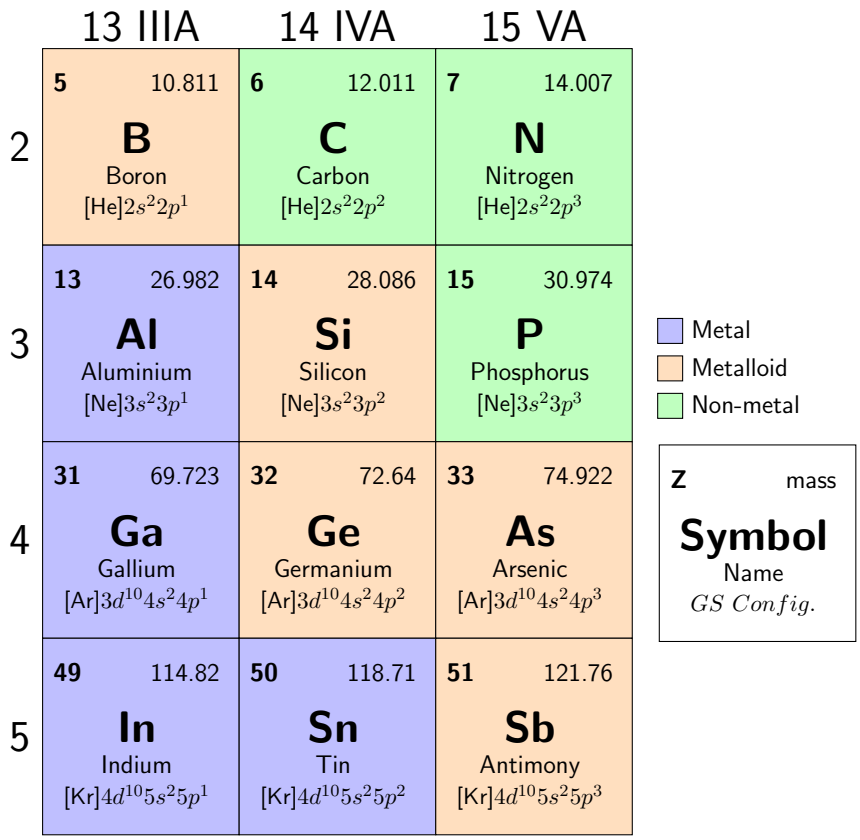

Figure 1.2: Metalloid section of the periodic table where most of the important semiconductor elements reside. Elements in each column have valence 3, 4, and 5 from left to right, and increase in radius from top to bottom.

small bandgap materials have higher mobility and permittivities.

The FCC forms of the first few group IV semiconductors (C, Si, Ge, α-Sn) and all polytypes of SiC are indirect gap materials. In contrast to this, a large number of III-V compound semiconductors are known to be direct gap materials (GaAs, GaSb, InP, InAs, InSb, AlN, GaN, InN). Though generally true, this fact is not readily apparent without performing detailed band structure calculations.

Table 1.1: Material property comparison of Diamond, 4H-SiC, Si, and Ge at 300K (descending in column IV from left to right).

Property	**Diamond [16]**	**4H-SiC**	**Si**	**Ge**
Lattice Structure	FCC	Hexagonal	FCC	FCC
Bandgap E_g (eV)	5.45	3.2	1.1	0.66
Direct Gap E_Γ (eV)	7.3	5-6	3.4	0.8
Breakdown Field (MV/cm)	10	3.0	0.6	0.1
Intrinsic Carrier Concentration (cm^{-3})	10^{-27}	10^{-8}	10^{10}	2×10^{13}
Bulk Electron Mobility (cm^2/Vs)	2200	800	1200	3900
Bulk Hole Mobility (cm^2/Vs)	1600	115	420	1900
Thermal Conductivity (W/cm K)	20	3-5	1.5	0.58
Relative Permittivity	5.7	9.7	11.9	16

1.2.2 Bonding

Also known as the Carbon Group, elements in this column of the periodic table (Figure 1.2) have 4 valence electrons and readily form covalent bonds with 4 neighboring atoms in a tetrahedral arrangement due to sp^3 hybridization. Electrons in these hybridized orbitals exhibit 25% s and 75% p character, which result in the 4-lobed tetrahedral shape that maximizes the separation of the electrons in the surrounding bonds from each other. A spatial visualization of these orbitals is shown in Figures 1.3 and 1.4 below.

In addition to the group IV elements forming tetrahedral bonding structures, it is not unreasonable to assume that compounds of the form AB with one atom of valence 3 and one of valence 5 will do the same but with higher ionicity bonds instead. These tetrahedrons can be arranged differently with respect to each other to give the crystal lattices in which these materials are commonly found. Elemen-

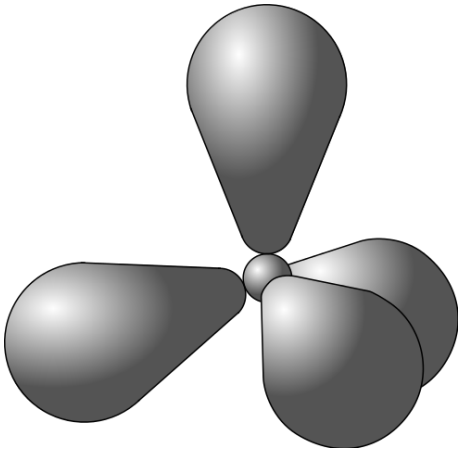

Figure 1.3: Cartoon visualization of the four sp^3 orbital lobes.

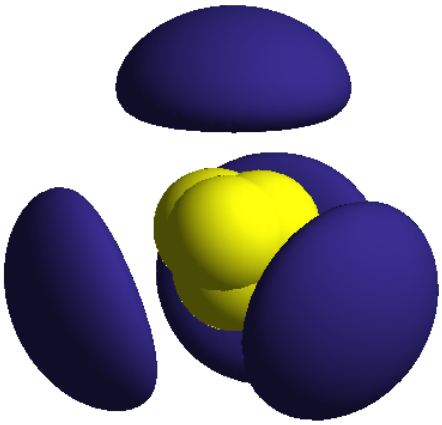

Figure 1.4: Actual form of sp^3 tetrahedron (level set of the wavefunction) showing overlaid orbitals. Yellow and blue colors denote opposite signs the wavefunction.

tal column IV crystals tend to adhere to the face-centered cubic (FCC) diamond lattice structure, while III-IV materials generally form in the analogous zinc-blende structure (FCC) or more rarely the wurtzite (hexagonal) structure [6].

In general, as the atomic radius of an element increases (descending within a column), bonds between nearest neighbor atoms become weaker due to spreading of higher energy valence wavefunctions. Consequentially the atoms become more separated and in turn exhibit smaller bandgap. This effect can be understood by thinking about bringing N identical atoms close enough together for their atomic orbitals to have significant overlap. When this happens, the energy levels of the individual atoms (normally degenerate for like-atoms) must split into bands of N closely-spaced states so as to not violate the Pauli exclusion principle. The amount of band splitting is directly related to the degree of wavefunction overlap. This

causes lower energy orbitals which are confined to the inner core region to split less than the higher energy valence orbitals with a larger spatial extent.

The manner in which this occurs leads to the formation of forbidden energy gaps and determines the value of the bandgap based on the equilibrium atomic spacing and the band occupancies. In addition to the atomic energies broadening into bands, the bands begin to bend and in certain situations merge as orbitals hybridize before ultimately separating again once inter-atomic distance becomes very small.

Energy levels corresponding to wavefunctions of favorable (bonding) charge distributions will tend to decrease with decreasing interatomic distance. Conversely, antibonding energies where electrons are localized away from bonding sites will be increased due to the energetically unfavorable configuration. These antibonding wavefunctions are analogous to high energy molecular orbitals which occur in chains of atoms. By taking linear combinations of the N atomic orbitals, A chain of N atoms gives rise to N possible molecular orbitals which contain from 0 to n-1 nodes between atoms where the density goes to zero. The 0 node solution corresponds to the fully bonding wavefunction and the n-1 node to the fully antibonding wavefunction. The band formation for a chain of 6 atoms is shown in Figure 1.5;

Similarly, in a crystal, the lowest energy level at the bottom of each band corresponds to the in-phase bonding state combination of atomic orbitals and the top level to the fully out-of phase antibonding configuration. Levels in the middle of the band consist of states which are various other combinations of atomic orbitals

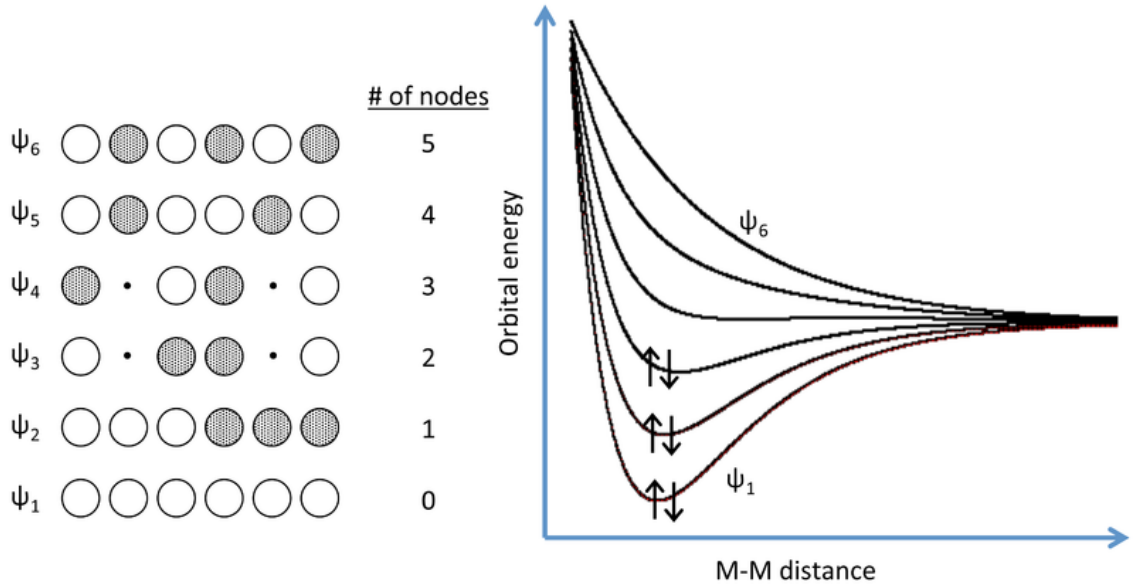

Figure 1.5: Molecular wavefunctions for a linear chain of 6 atoms. Degenerate energies split as interatomic distance decreases due to the interaction of neighboring atomic orbitals. Light and dark circles represent positive and negative orbital lobes respectively. By Tem5psu (Own work) [CC BY-SA 4.0 (http://creativecommons.org/licenses/by-sa/4.0)], via Wikimedia Commons

which smoothly transition between these two extremes.

Once atoms are forced closer to and beyond their equilibrium distance, the hybridized bands ultimately begin to split from each other due to the large Coulombic repulsion of the ions [17]. The widths of the allowed energy bands are limited by the small number of near-neighbor atoms which are close enough for their wavefunctions to significantly overlap. Adding additional atoms to the system only results in further subdividing states within the band such that it closely resembles a continuum of states [18]. The band gap of a material is determined by the degree of separation between the last occupied band refered to as the valence band, and the next higher unoccupied band known as the conduction band. In the case of FCC column IV materials, the valence and conduction bands consist of the bonding sigma band

and the antibonding sigma* band respectively, the formation of which is depicted in Figure 1.6.

1.3 Silicon Carbide

1.3.1 Background and Applications

The world of power electronics is ever growing and at present particularly due to the recent concerns of alternative energy technologies and the commercial emergence of fully-electric vehicles. As Si-based power devices approach their material limits, alternative materials are being researched to take advantage of their different material properties [19]. Typically, wide bandgap semiconductors are the main go-to for use in high power, high temperature devices for their beneficial electrical and thermal properties. SiC is of particular interest due to its ability to form a stable native oxide and the commercial emergence of good quality substrates [20]. Since 2014, the SiC wafer market has grown each year by approximately 21% and is predicted to continue this trend until at least 2020 to reach $110 million [21]. As a whole, the SiC power semiconductor market is projected to exceed $1.6 billion in 2022 [22].

SiC crystals exist in numerous polytypes, meaning each crystal shares the same close-packed layers but differ in the periodic stacking order of these layers. Of the various polytypes, the 6H and 4H variants have seen the most use in electrical device applications. Currently, 4H devices are the dominant among commercial devices due to its higher carrier mobility and low dopant ionization energy [23].

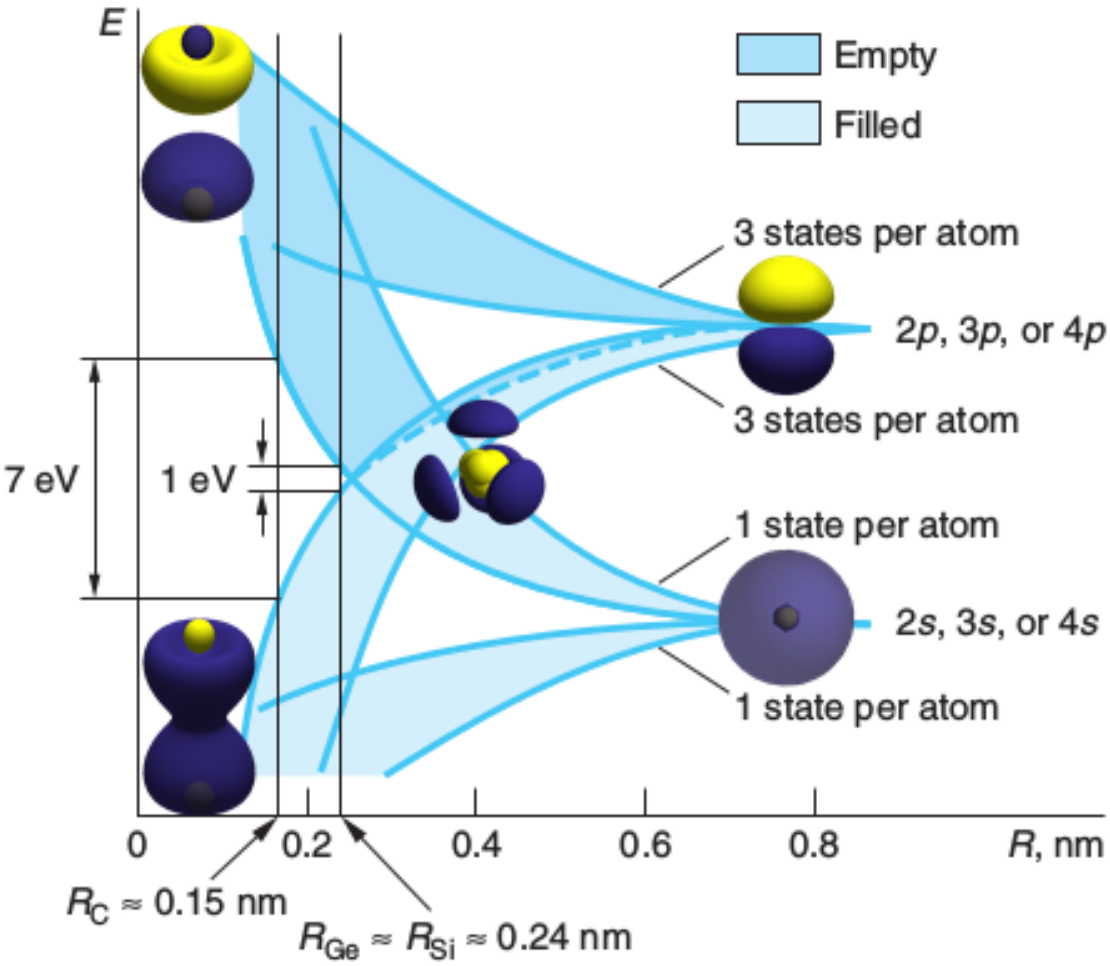

Figure 1.6: Splitting and occupancy of 2s (3s,4s) and 2p (3p,4p) states of carbon (silicon, germanium) as a function of inter-atomic spacing. The distance between the top of the filled band and the bottom of the unfilled band shows formation of various bandgap values at experimental inter-atomic distances. Inset images depict spatial visualizations of the kinds of orbitals found in each band. Orbitals shown: 2s orbital (bottom right), 2p orbital (top right), overlaid hybrid sp^3 orbitals (center), sp^3 sigma bonding orbital (bottom left), and sigma* antibonding orbital (top left). Color represents sign of wavefunction. [4]

In addition to SiC's high thermal conductivity, saturation velocity, and breakdown field, it performs better than Si on-chip due to both its lower on-state resistance, smaller chip area, and higher switching frequency [19,23]. The price paid in increased device costs is outweighed by the improved characteristics and performance gains achieved using SiC.

One key application of SiC is for use in the construction of more energy efficient and power dense DC/DC, DC/AC, AC/DC, and AC/AC converter circuits [23]. In particular, DC/AC inverter circuits are needed in electric vehicles and photovoltaic systems to convert the stored battery power into usable power. DC/DC converters enjoy an increased operating voltage range and a drastic size reduction due to the need for a smaller inductor. For a given peak-to-peak ripple in a DC-DC converter, the inductance value needed is inversely proportional to the switching frequency of the transistor [19]. The properties of SiC allow for high switching frequencies so the size requirement of the inductor is be reduced, thus shrinking the module's overall size [24].

1.3.2 Crystal Structure and Properties

SiC crystals are arranged such that each carbon atom is covalently bonded to four silicons and vise versa in a tetrahedral manner. Because these tetrahedra may be stacked differently, SiC forms what are known as polytype variants. The tetrahedrons create close-packed planes of atoms which vary in their stacking arrangement along the normal direction. The order and periodicity of the stacking

defines the polytype of the crystal which is denoted <number><letter>-SiC, where <number>is the period of the stacking arrangement, and <letter>abbreviates the Bravais lattice of the crystal (C for cubic, H for hexagonal, R for rhombohedral). Figure 1.7 illustrates the stacking arrangement for the most common polytypes, although there are more than 200 known /citeLiu.

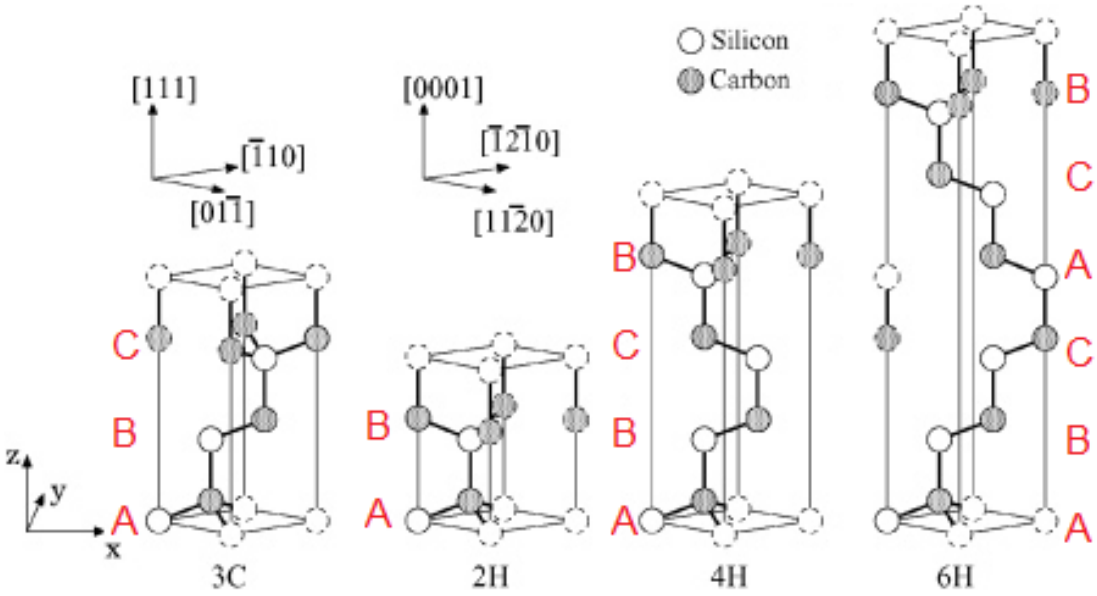

Figure 1.7: SiC polytypes depicting only key atoms forming the bonding chain in the stacking direction. Primitive cells are shown for the hexagonal polytypes and a non-primitive hexagonal cell is used for 3C. Polytypes differ only in the stacking order and periodicity of the close-packed atomic planes. For the cubic variant, this is the {111} plane and for the hexagonal variants, the {0001} plane. (Figure from [5]).

Because the different polytypes of SiC have different atomic arrangements, they differer in their electrical characteristics and electronic structure. Table 1.2 compares the properties of the two most commonly used polytypes of SiC to the industry standard Si. As shown in the table, the 4H variant has a slightly larger bandgap and a greatly increased bulk mobility compared to 6H [22]. The breakdown field of SiC is approximately 5 times larger than in Si, allowing it to hold-off the

much larger voltages seen in power applications. Additionally, SiC exhibits a 2-3 fold larger thermal conductivity so heat can be dissipated from the device more easily, preventing thermal runaway and reducing the need for large costly cooling systems [19]. The increased thermal conductivity in addition to a significantly higher melting temperature also increases the maximum operating temperature of the device and consequentially, a larger maximum current density.

Table 1.2: Electrical property comparison of SiC to Si at 300K. Data from [25]

Property	**6H-SiC**	**4H-SiC**	**Si**
Bandgap E_g (eV)	3.0	3.2	1.1
Breakdown Field (MV/cm) $N_D = 10^{17}$ cm^{-3}	∥c-axis: 3.2 ⊥c-axis: >1	∥c-axis: 3.0 ⊥c-axis: 2.5	0.6
Intrinsic Carrier Concentration (cm^{-3})	10^{-5}	10^{-8}	10^{10}
Bulk Electron Mobility (cm^2/Vs) $N_D = 10^{16}$ cm^{-3}	∥c-axis: 60 ⊥c-axis: 400	∥c-axis: 800 ⊥c-axis: 800	1200
Bulk Hole Mobility (cm^2/Vs) $N_D = 10^{16}$ cm^{-3}	90	115	420
Thermal Conductivity (W/cm K)	3-5	3-5	1.5
Relative Permittivity	9.7	9.7	11.9

Because the most commonly used polytype of SiC in power devices is the 4H variant, the remainder of this thesis will discuss 4H-SiC exclusively. Figure 1.8 shows the hexagonal lattice of 4H-SiC along with the Miller indices of associated directions/planes.

The (0001) Si-face of 4H-SiC is by far the most commonly available wafer type. On this face, Si atoms terminate 100% of the face but other faces have different Si-to-C ratios and packing density. The various atomic structures exhibited by each face causes different electrical transport and oxidation characteristics. Opposite to the Si-

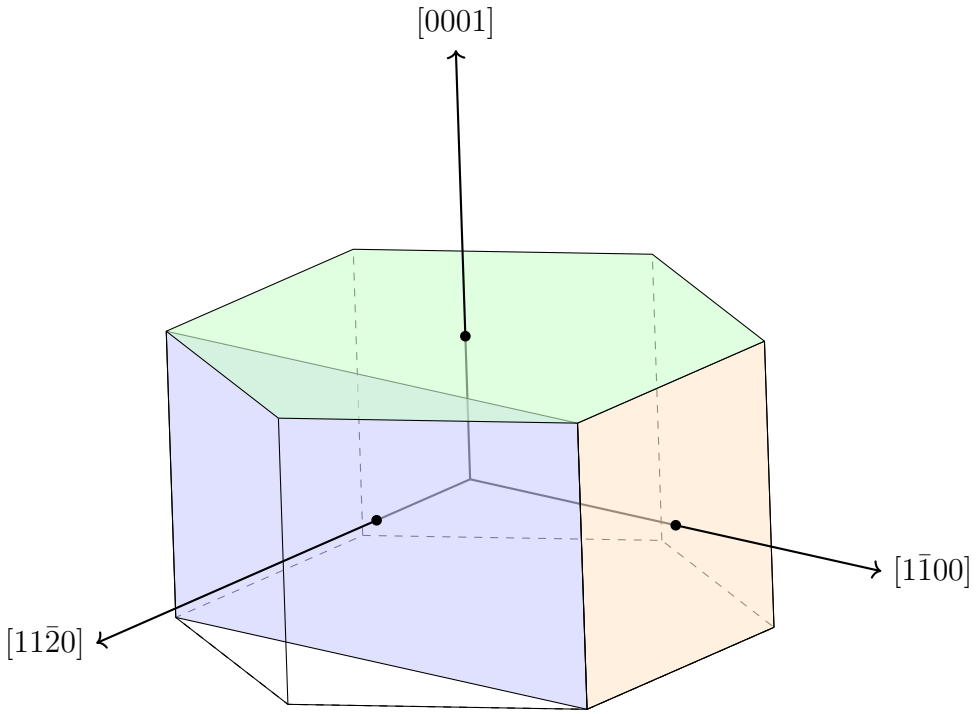

Figure 1.8: Wigner-Seitz cell of hexagonal real-space lattice structure and relevant crystal planes

face is the C-face (000$\bar{1}$) which is terminated completely by C atoms. Perpendicular to these are the a-face (11$\bar{2}$0) and the m-face (1$\bar{1}$00) which are investigated for their use in vertical devices and have an equal number of Si and C atoms. Figure 1.9 shows the stacking arrangement and key faces of the 4H-SiC structure.

In terms of process variation for different faces, the Si-face shows the slowest oxide growth rates which are approximately 12 times slower than the C-face. The a-face growth rate is slightly slower than the C-face but still significantly faster than the Si-face which takes 12 hours to grow 50nm of oxide at 1150°C [22]. As a consequence of different surface morphologies, some faces show greater electron mobility than others. Specifically, the Si-face exhibits the lowest channel mobility (< 10 cm^2/Vs) compared to the a-face mobility (> 25 cm^2/Vs) depending on the

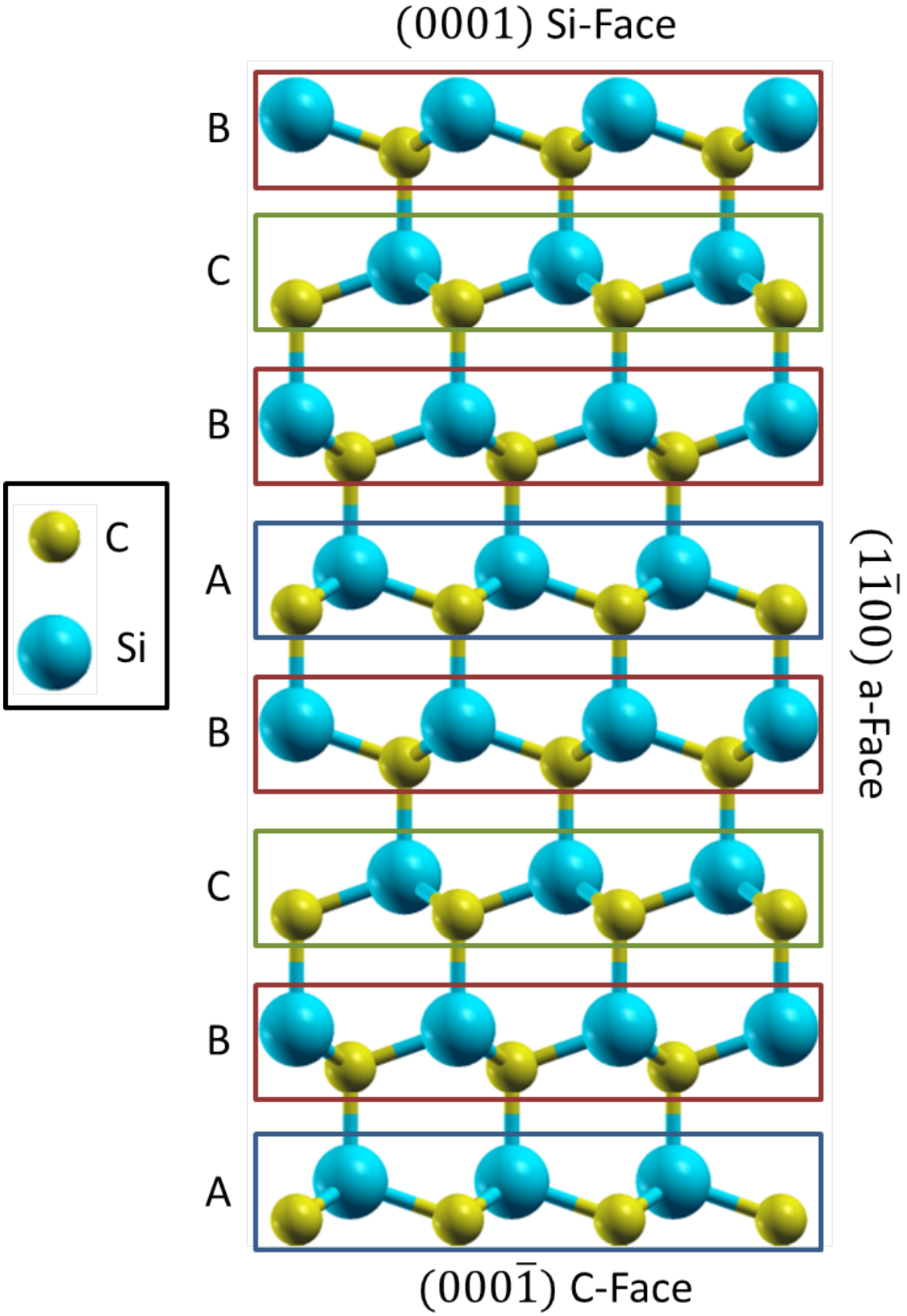

Figure 1.9: 4H-SiC lattice depicting the stacking arrangement and crystal faces

degree of surface passivation [22]. With NO surface passivation these mobilities can be improved to 80 and 125 respectively. A mobility of 90 cm^2/Vs has been achieved on passivated C-face [22]. Despite having the lowest mobility, the Si-face is still commonly used for its superior threshold voltage stability compared to its other faces [26].

1.3.3 Issues in SiC Power Devices

Traditionally, SiC MOSFETs have suffered from low channel mobility due to poor quality SiC-SiO_2 interfaces [19]. In particular, large surface roughness and a high density of interface states increases carrier scattering in the channel, causing the surface mobility to drop approximately 1-2 orders of magnitude from the bulk value [3]. The low mobility of SiC MOSFETs causes devices to have a small transconductance and thus poor gate control of current. Various defects have been detected and characterized by many researchers including [14, 27, 28]. In addition to causing scattering, some defects can cause carrier trapping and threshold voltage instability, leading to reliability issues which is a heavily researched topic [15]. These defects are not passivated by post-metalization H_2 anneals as they are in Si, but NO has been shown to improve interface defect density [14, 22].

1.4 Germanium Photonics: Benefits and Challenges

In addition to SiC I also investigate the optical properties of Ge and its potential use in beyond-silicon integrated electronics at the end of the Si road map.

Germanium is a natural replacement for CMOS due to it's ability to grow a native thermal oxide, a property crucial to form the gate oxide in MOS transistors. Currently, research has been done seeking to integrate Ge into Si CMOS devices. Ge is a decent candidate for integration due because it has the same lattice structure as Si with a different lattice constant. This integration does not come without difficulty however. The lattice mismatch necessitates a high concentration of misfit dislocations at the interface and further challenges exist regarding compatibility of processing growth temperatures [29].

Germanium is known to have an indirect band gap of 0.66eV, allowing it to function as a relatively inefficient detector of short-wave infrared (SWIR) light. Instead of trying to integrate a Ge detector into Si CMOS circuitry, the photonics can be developed on a purely germanium substrate so that both the optics and supporting electronics are both made of Ge. In doing this, we can exploit the beneficial electrical properties of Ge such as its superior (3x) mobility to Si.

In this work, our main focus will be on the study of the Ge band structure and how the conduction band minima change with respect to varying concentrations of Sn in Ge-Sn alloy. By introducing a certain fraction of Sn to the Ge, the bandgap can be transformed from a indirect in nature to direct, allowing for more efficient photon detection. The key to this process is finding the minimum amount of Sn required to transition so that the gap energy is still as close to its original value as possible.

1.5 Research Accomplishments

SiC:

- Performed a self-consistent DFT calculation of a 125 atom ideal 4H-SiC/SiO_2 interface supercell using Quantum ESPRESSO [30].
- Developed a novel technique to extract an interface scattering perturbation potential from DFT calculations. This scattering is due to the aperiodicity caused by the presence of the interface and the atomic roughness therein.
- Calculated a 2D quantized inversion layer scattering rate based on the extracted perturbation potential for use in surface Monte Carlo scattering simulation.
- Reproduced bulk 4H-SiC field-dependent velocity characteristics from Monte Carlo simulations.
- Calculated and compared mechanism-dependent component mobilities important to MOS device mobility including my own proposed atomic-roughness mobility which will be present even in an ideal SiO_2/SiC interface.
- Combined and adapted physics-based models for doped semiconductor systems to calculate theoretical mobile hole to acceptor concentration ratio (p/N_A)
- Gathered, analyzed, and created empirical parameterizations for concentration-dependent data of nearly all existing published Hall mobility, resistivity, and ionization energy data on Al-doped 4H-SiC. I used the ionization energy data as input into my physics-based model. The Hall mobility and resistivity data were used verify my physics-based p/N_A result by using a method which was

first applied to Si.

- Created a more readily usable closed-form expression of my temperature and concentration-dependent p/N_A calculation. The original physics-based model involves iterative numerical techniques to solve a nonlinear system of integrals which is computationally expensive so I developed a genetic algorithm to find the optimal parameters for an expression which reproduces the same two-dimensional p/N_A function but is much more easily implemented.
- Used a variation of my genetic algorithm to parameterize the fully temperature and concentration dependent Al-doped 4H-SiC Hall mobility function based on data from nearly all existing published values. This result should be valid over a larger temperature and doping range than those currently published.

Ge:

- Reproduced key gap energies in the band structure of Ge using a hybrid DFT calculation.
- Calculated band structure for various $Ge_xSn_{(1-x)}$ alloys with various ratios.
- Determined the fraction at which the band structure of the material becomes direct.

1.6 Future Work

Currently, the scale at which my DFT calculations can be performed is significantly limited by the practical memory and processing power constraints of the computer on which I am performing the calculations. This limits the size of the

supercell to the order of about 100 atoms for practical computations. With a more powerful computer, it would be possible to simulate significantly larger supercells which could accommodate interesting defect structures. The issue with trying to simply add a defect to a smaller supercell is that this cell is periodic and thus any defect you add will also be periodic. Without a sufficiently large cell, this defect will have a higher concentration than the real-world analogue which can cause incorrect results due to the defect interacting with itself. Additionally, to simulate aperiodic structures like amorphous oxide, surface roughness, defects, etc., the correlation length of the structure is bounded by the periodicity of the supercell. Therefor, with a larger supercell, a 'less periodic' structure can be simulated.

To extend my research of scattering at the SiC/SiO_2 interface, two main aperiodic structures are prime candidates for a DFT-based study:

First, it would be interesting to simulate a non-pristine interface which contains a real atomic configuration of the miscut roughness and step bunching which recreates an AFM-measured SiC surface. Performing statistical calculations of the RMS roughness height and the autocovariance of the supercell's atomic configuration should be matched to the real measurements. A reverse Monte Carlo algorithm could be used to continually generate random atomic step configurations for the supercell until the toughness statistics match, then an amorphous oxide can be added and structurally relaxed to create the final interface. Even better (but significantly more computationally intensive) would be to simulate the growth of the oxide from the rough miscut surface using a molecular dynamics simulation. Finally, with this supercell structure, the surface-roughness scattering rate of the miscut surface could

be calculated using the methods described in my research and this would give insight as to the impact the miscut roughness has on the SiC MOS channel mobility. Additionally, it would be interesting to directly measure experimentally the channel mobility of MOS structures using identically- produced SiC wafers with varying miscuts.

Second, basal plane dislocations (BPDs) are known to be device-impairing defects in MOS structures. However, device fabricators generally try to transform these dislocations into supposedly less harmful threading edge dislocations (TEDs). The actual effect of the TEDs has yet to be fully studied and characterized, so a DFT study to extract the scattering rate of TEDs would be useful to inform device designers and fabricators how their presence is affecting the MOS channel mobility.

In terms of my work on incomplete ionization, I have extracted and fit with my genetic algorithm the Hall mobility literature data as a function of both temperature and N_A, however the resistivity data is a much more complicated function and I only fit it as a function of N_A at $T = 300K$. To fully check agreement with my temperature-extended theoretical model results of incomplete ionization, a fit of the temperature and N_A dependent resistivity literature data would need to be performed.

Chapter 2: DFT and Electron Transport Modeling and Theoretical Framework

2.1 Many-Body Schrodinger Equation

Determining the properties of a multi-atomic system traditionally involves solving the many-body Schodinger equation. This, however, quickly proves infeasible when the number of atoms increases as the wavefunction quickly becomes a function of far too many coordinates ($3 \times (n + N)$ for n electrons and N nuclei). The time-independent Schrodinger equation itself is an eigenvalue problem which has allowed energy states as eigenvalues and their corresponding wavefunctions as eigenvectors.

$$\left(-\sum_{j=1}^{N}\frac{\hbar^2}{2M_j}\nabla_{R_j}^2-\sum_{i=1}^{n}\frac{\hbar^2}{2m}\nabla_{r_i}^2-\frac{q^2}{4\pi\epsilon_0}\sum_{i=1}^{n}\sum_{j=1}^{N}\frac{Z_j}{\left|\vec{r_i}-\vec{R}_j\right|}+\frac{1}{2}\frac{q^2}{4\pi\epsilon_0}\sum_{i=1}^{n}\sum_{i'\neq i}^{n}\frac{1}{|\vec{r_i}-\vec{r_{i'}}|}+\right.$$
$$\left.\frac{1}{2}\frac{q^2}{4\pi\epsilon_0}\sum_{j=1}^{N}\sum_{j'\neq j}^{N}\frac{Z_jZ_{j'}}{\left|\vec{R}_j-\vec{R}_{j'}\right|}\right)\Psi=E\Psi\left(\vec{r_1},\ldots,\vec{r_n},\vec{R}_1,\ldots,\vec{R_N}\right) \tag{2.1}$$

Because the wavefunction of a system contains within it all of the information knowable about the system, the left-hand side of the equation is a large operator which acts on the wavefunction to extract different energy components. This operator is also known as the Hamiltonian of the system. The Hamiltonian can be broken down into a combination of smaller quantum-mechanical operators which are, in

order: nuclear kinetic energy, electron kinetic energy, electron-nuclei coulombic potential energy (attraction), electron-electron coulombic potential energy (repulsion), nuclei-nuclei coulombic potential energy (repulsion). In this equation M_j, Z_j, and R_j are the mass, atomic number, and position of the jth nuclei and m, q, r_i are the mass, charge, and position of the rth electron.

2.1.1 Born-Oppenheimer Approximation

To begin simplifying the problem, the equation is usually solved in the context of the Born-Oppenheimer approximation, which assumes that because the nuclei are far more massive than the electrons, they move on different time scales and as such, the total wavefunction for the system can be separated into an electronic component and a purely nuclear (vibrational,rotational) component.

$$\Psi_{tot} = \Psi_{electronic} \times \Psi_{nuclear} \tag{2.2}$$

The electronic solution is found by solving the electronic Schrodinger equation with the positions of the nuclei fixed (usually in their equilibrium configuration). By slowly varying the location of the nuclei and re-solving the electronic equation, the electron energy as a function of nuclei positions can be extracted. This term acts as the nuclear potential term and in combination with the nuclear kinetic energy term, is used to form the nuclear Schrodinger equation who's solution results in the nuclear portion of the wavefunction.

2.2 Density Functional Theory

2.2.1 Origins of DFT

The motivation to find a theory such as DFT comes from the immense difficulty of solving a large quantum mechanical system exactly. The majority of the difficulty in solving such systems stems from the high dimensionality of the problem. For a system of N electrons and M nuclei, the total wavefunction is a function of 3(N+M) spatial variables where N and M are on the order of Avogadro's number for a real crystal. A system of this size is effectively impossible to solve given the finite memory and calculation speed of todays computers; even smaller systems of a few hundreds of atoms are impractical to solve within any reasonable amount of time [31]. These restrictions sparked a need for a practical way to solve these systems via a reduction of dimensionality.

Thomas and Fermi in 1927 were the first to propose that the electron density was the fundamental variable defining the quantum many-body system. In making this assumption, calculation of the complicated high-dimensional wavefunction can be ignored and instead the simple 3-dimensional density is used in the calculation. Though their formulation in general proved too crude for accurate calculations, their use of the density as a fundamental variable laid the foundation for the later greatly successful density functional theory (DFT).

Around the same time the Thomas-Fermi model was being developed, another important technique emerged which aimed to approximately solve the many-body

Schrdinger equation. First introduced in 1928 by Hartree [32], this technique became known as the self-consistent field method due to need to iterate solutions to achieve convergence. In this framework, the wavefunction for each electron ψ_i is calculated assuming each electron experiences a total potential created by the atomic nucleus and all other electrons in the system. By starting with an initial guess for the electron density, an approximate potential and Hamiltonian is determined from which the wavefunctions can be solved. These wavefunctions in turn determine an electron density and iteration is performed until the system is solved in a self-consistent manner. The total wavefunction of the complete system in Hartree's case was approximated to be the product of all the one-electron wavefunctions [31].

$$\Psi(\mathbf{r}_1, \mathbf{r}_2, \ldots, \mathbf{r}_N) = \psi_1(\mathbf{r}_1) \cdots \psi_1(\mathbf{r}_N) \tag{2.3}$$

The original Hartree equation is shown in Equation 2.4 where the two potential terms are the external potential $V_{ext}(\mathbf{r})$ created by the atomic nuclei and the potential due to the mean field of all the other electrons. The equation must be solved iteratively because the latter term is function of the other wavefunction solutions.

$$\left(-\frac{1}{2}\nabla^2 + V_{ext}(\mathbf{r}) + \sum_{j \neq i}^{N} \int \frac{|\psi_j(\mathbf{r'})|^2}{|\mathbf{r} - \mathbf{r'}|} d\mathbf{r'} \right) \psi_i(\mathbf{r}) = \epsilon_i \psi_i(\mathbf{r}) \tag{2.4}$$

The total energy of the system, shown in Equation 2.5, is a simple sum of the individual electron energies minus the double counting from the electron-electron Coulombic potential energy term.

$$E^H = \sum_{n=1}^{N} \epsilon_n - \frac{1}{2} \sum_{i \neq j}^{N} \int \int \frac{|\psi_i(\mathbf{r})|^2 |\psi_j(\mathbf{r'})|^2}{|\mathbf{r} - \mathbf{r'}|} d\mathbf{r} d\mathbf{r'} \tag{2.5}$$

Later, Fock and Slater in 1930 showed that by replacing the simple product with a determinate of the single-electron wavefunctions, the resulting total wavefunction automatically satisfies the antisymmetric requirements of the Pauli exclusion principle and treats particle exchange exactly [31, 33, 34]. The determinant construction of the total wavefunction is shown below in Equation 2.6.

$$\Psi(\mathbf{r}) = \frac{1}{\sqrt{N!}} \begin{vmatrix} \psi_1(\mathbf{r}_1) & \cdots & \psi_N(\mathbf{r}_1) \\ \vdots & \ddots & \vdots \\ \psi_1(\mathbf{r}_N) & \cdots & \psi_N(\mathbf{r}_N) \end{vmatrix} \tag{2.6}$$

In 1964, the density functional formalism set forth by Hohenberg and Kohn gave the work done by Thomas and Fermi mathematical grounds on which to stand. The Hohenberg-Kohn Theorem showed that the ground state of an atomic system is fully determined by the density distribution $n(\mathbf{r})$ of the electron [31]. Furthermore, the energy can be written as a *functional* of the density, meaning it takes in the density function as input and returns the total energy (a single value) as output. More specifically, they showed that there exists a universal energy functional $F[n(\mathbf{r})]$ which applies to any and all systems. This powerful proof, along with the proof of a variational principle, allows us to find the ground state by hunting for the density which minimizes the energy. In principle we can even ignore calculating the wavefunction entirely, though some techniques still involve solving for it. By simply working with the density, the dimensionality of the system is reduced from the order of Avagadro's number to only 3 spatial dimensions. Though this theory lays the

groundwork for greatly simplifying the problem, it unfortunately does not give any insight into form of the universal functional. The details of each of these theories are discussed further in Appendix A.

2.2.2 Kohn-Sham Method

Developed in 1965, this formulation of DFT acts as a practical implementation of the Hohenberg-Kohn Theorem (Appendix A.3) by defining a set of component energies, each with a clear physical origin, which sum to approximate the universal energy functional $F[n(\mathbf{r})]$. The central feature of this method involves defining a fictitious system of noninteracting electrons moving in an effective external potential, which gives rise to the same density as the true interacting system. All of the single-particle wavefunctions satisfy a Schrdinger-like equation known as the Kohn-Sham equation (Eqn. 2.7 in atomic units), where the potential term is the Kohn-Sham effective potential - a functional of the density derived from the terms in the energy functional. The lowest N eigenstates of this equation give the N single-particle wavefunctions ϕ_i known as the Kohn-Sham orbitals. The ground state wavefunction of this system can then be exactly written as a Slater determinant of the single-particle wavefunctions to account for anti-symmetry because there is no electron-electron interaction (Eqn. 2.8). The total density can be calculated from the single-electron orbitals using Equation 2.9.

$$-\frac{1}{2}\nabla^2\phi_i(\mathbf{r}) + V_{KS}(\mathbf{r})\phi_i(\mathbf{r}) = \epsilon_i\phi_i(\mathbf{r}) \tag{2.7}$$

$$\Psi(\mathbf{r}) = \frac{1}{\sqrt{N!}} \begin{vmatrix} \phi_1(\mathbf{r}_1) & \cdots & \phi_N(\mathbf{r}_1) \\ \vdots & \ddots & \vdots \\ \phi_1(\mathbf{r}_N) & \cdots & \phi_N(\mathbf{r}_N) \end{vmatrix} \tag{2.8}$$

$$n(\mathbf{r}) = \sum_{i}^{N} \phi_i^*(\mathbf{r})\phi_i(\mathbf{r}) \tag{2.9}$$

Taking the expectation of the universal functional with the full Kohn-Sham Slater determinate wavefunction gives us insight to the forms of terms in the total Kohn-Sham energy functional $E_{KS}[n]$ with which we aim to approximate the true functional $F[n]$.

$$E^{KS}[n(\mathbf{r})] = T_S[n] + E_{ext}[n] + E_H[n] + E_X[n] + E_C[n] \tag{2.10}$$

$$E^{KS}[n(\mathbf{r})] = -\frac{1}{2}\sum_{i}^{N} \int \phi_i^*(\mathbf{r})\nabla^2\phi_i(\mathbf{r})d\mathbf{r} + \int V_{ext}(\mathbf{r})n(\mathbf{r})d\mathbf{r} + \frac{1}{2}\int\int \frac{n(\mathbf{r})n(\mathbf{r'})}{|\mathbf{r}-\mathbf{r'}|}d\mathbf{r}d\mathbf{r'}$$
$$-\frac{1}{2}\sum_{i,j}\int\int \frac{\phi_i^*(\mathbf{r})\phi_i(\mathbf{r'})\phi_j^*(\mathbf{r'})\phi_j(\mathbf{r})}{|\mathbf{r}-\mathbf{r'}|}d\mathbf{r'}d\mathbf{r} + E_C[n(\mathbf{r})]$$

Here, $T_S[n]$ represents the 'single particle' or non-interacting kinetic energy which is why it can be calculated using a simple sum over all of particle's wavefunctions. $E_{ext}[n]$ is the external energy which comes from any external potential, such as the Coulombic attraction to ionic cores of atoms. $E_H[n]$ is the Hartree energy caused by the Coulombic repulsion of all other electrons. $E_X[n]$ is the exchange energy due to Pauli's principle and the antisymmetry of the wavefunction. These are the terms which have tractable expressions. The final term $E_C[n]$ represents the correlation energy, which can be thought of as an error term. The correlation energy

contains all energy differences between our constructed non-interacting system and the true system energy functional $F[n]$ and accounts for about 10% of the total energy of a system. This correction energy accounts for the self-interaction error within E_H as well as the difference in the kinetic energy between the fully interacting and non-interacting system. The error in E_H for the interacting system comes from the fact that when the integral is solved for a 1-electron system, it does not identically equal 0, meaning the electron is interacting with itself so a cancellation term is needed. Exchange energy can also been seen as the effective repulsion of electrons with parallel spins due to the Pauli exclusion principle, and the Correlation energy due to interaction of electrons with anti-parallel spins.

The total energy functional of the Kohn-Sham method depends on the approximations made in formulating E_C. Additionally, given the computational expense associated with evaluating E_X, the two terms are often combined and approximated together as one E_{XC} term. Although DFT is exact in theory, we do not know the form of the universal functional - specifically the E_C term, so approximations to this introduce error and cause the method to be an approximation in practice.

Working backwards from the energy functional, we can generate the effective Kohn-Sham potential needed in the Kohn-Sham equation by taking the functional derivative of the external, Hartree, exchange, and correlation energies with respect to the density. These potentials represent the Coulombic ion potential, the Coulombic electron-electron interaction potential, and quantum-correction potential respec-

tively.

$$V_{KS}(\mathbf{r}) = V_{ext}(\mathbf{r}) + \frac{\delta E_H}{\delta n(\mathbf{r})} + \frac{\delta E_{XC}}{\delta n(\mathbf{r})} = V_{ext}(\mathbf{r}) + V_H(\mathbf{r}) + V_{XC}(\mathbf{r}) \tag{2.11}$$

$$V_{KS}(\mathbf{r}) = V_{ext}(\mathbf{r}) + \int \frac{n(\mathbf{r'})}{|\mathbf{r} - \mathbf{r'}|} d\mathbf{r'} + V_{XC}[n(\mathbf{r})]$$

Because the exchange-correlation potential V_{XC} depends on the density $n(\mathbf{r})$, itself depending on the orbitals $\phi_i(\mathbf{r})$, which in turn depend on the potential V_{KS}, solutions to the Kohn-Sham equation must be found iteratively to achieve self-consistency.

2.3 DFT Calculation Results

Figure 2.1 shows the calculated band structure from my DFT simulation using the open source software Quantum Espresso [30] with the PBE functional [35] and pbe-hgh psudopotentials from http://www.quantum-espresso.org. The resulting constant-energy ellipses of these minima calculated from this DFT computation are shown in Figure 2.2.

Notoriously, DFT tends to underestimate the band gap of semiconductors due to the approximations associated with the form of the energy functional (which actually contains discontinuities), and possibly due to an inevitability of the Kohn-Sham theory itself [36]. However, band structures resulting from DFT calculations still give useful insight into the structure of the actual bands and are often used in theory-based calculations.

For the purposes of creating a scattering theory, the important conduction band valleys are the two which lay nearly degenerate at the M point. The resulting

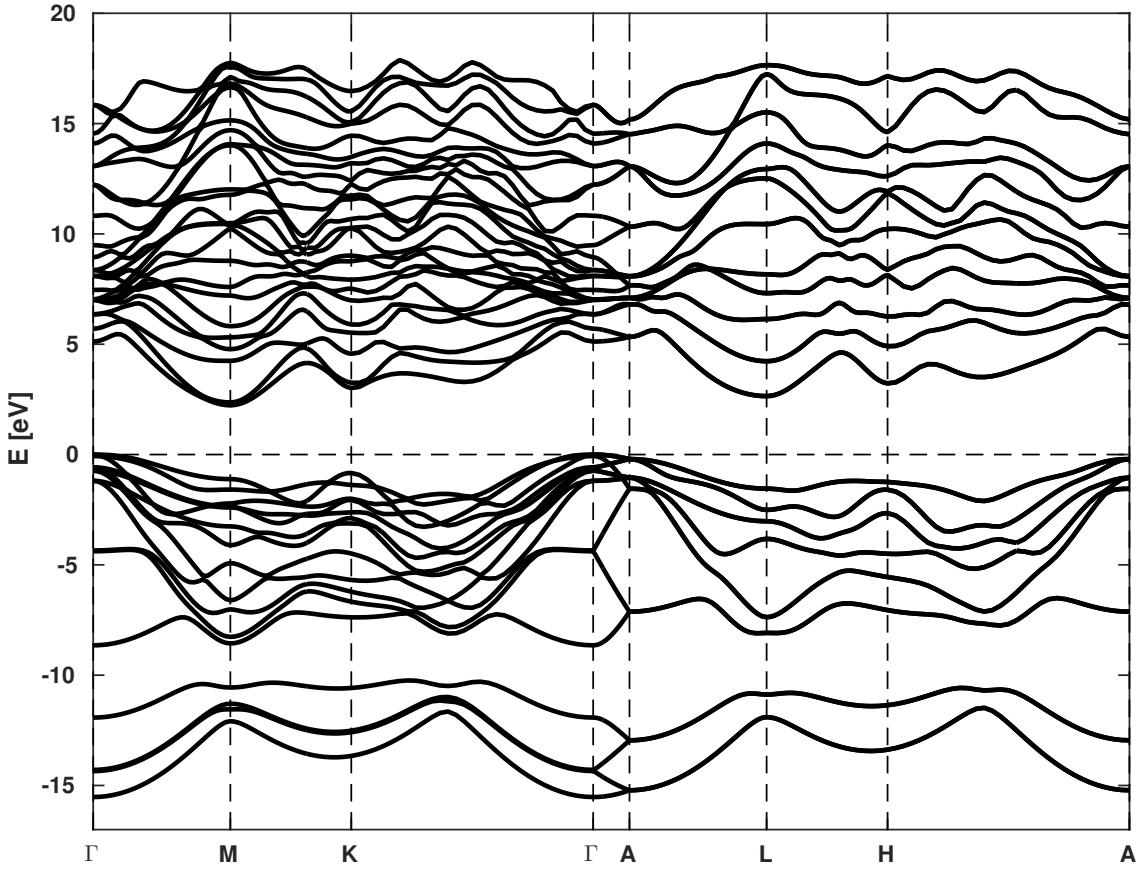

Figure 2.1: Theoretical band structure of 4H-SiC calculated with DFT.

gap energies and extracted effective masses of the DFT calculation are provided in Tables 2.1 and 2.2 respectively, where they are compared to the experimental values. In Chapter 3, this band structure calculation will be developed into a band model to be used in scattering rate calculations and Monte Carlo scattering simulations.

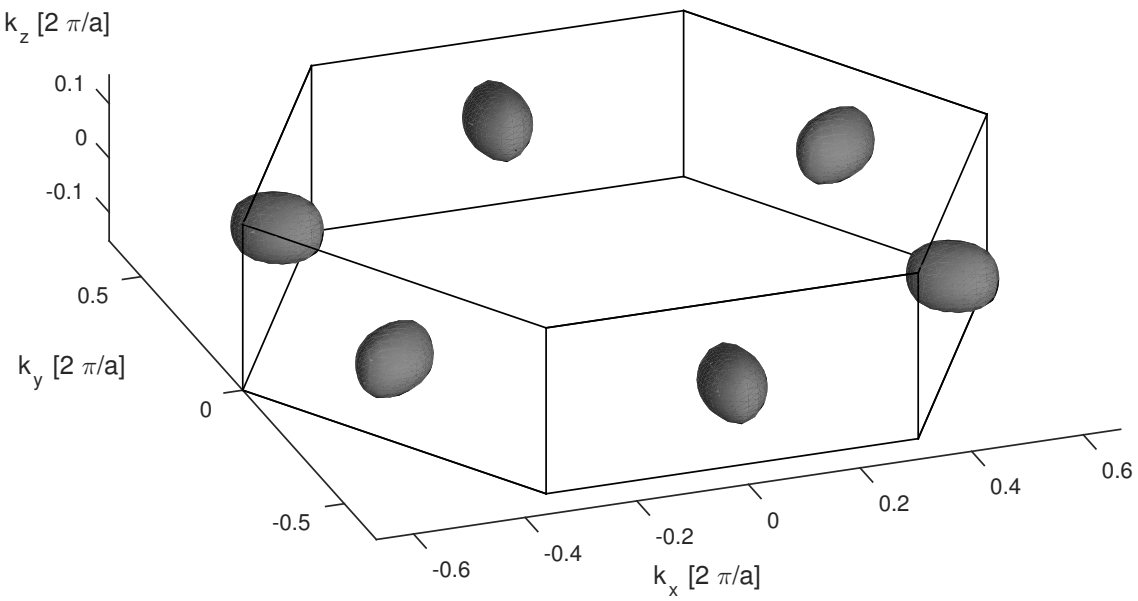

Figure 2.2: Constant energy ellipses for the lowest conduction band minimum at the M point, calculated using DFT.

Table 2.1: Comparison of calculated energy gap values of 4H-SiC to those found in the literature.

Gap [eV]	**Calc.**	**Lit.** [7, 8]
E_g (E_M)	2.23	3.23
E_{sM}	0.13	0.12
E_L	2.65	4
E_Γ	5.12	5-6
E_{cr}	0.07	0.08
E_{so}	≈0	0.007

Table 2.2: Comparison of extracted effective masses in the M valley from my DFT calculation to the experimentally measured values.

Mass [m_0]	**Calc.**	**Exp.** [37]
$E_{M-\Gamma}$	0.56	0.58
E_{M-K}	0.39	0.31
E_{M-L}	0.31	0.33

Chapter 3: Atomic-Level Electron Transport

3.1 Perturbation Scattering Theory

Now that we have set up a way to solve the quantum many-body problem through DFT, we need to lay the framework required to understand electron transport within a crystal. By understanding the electron transport of a material, electrical characteristics can be predicted and possibly improved by changing the atomic structure. In this chapter, I will first discuss existing perturbation scattering theory including Fermi's Golden Rule from which my results are derived and known scattering rate results. Then I will explain the technique for how I calculated my own atomic-roughness scattering rates for the best-case SiC-SiO_2 interface based on density functional theory calculations.

The primary difference between traditional Si MOS and emerging SiC MOS technology is the quality of the semiconductor-oxide interface. The poorer quality of the SiC/SiO_2 interface leads to significantly lower mobility due to surface roughness scattering and trapped interface charge scattering [38,39]. The treatment of scattering in SiC proceeds similarly to that of Si, but with a different number of equivalent valleys and with focus on different dominant scattering mechanisms. In this study, I apply the standard method of perturbation scattering theory to determine the scat-

tering rates for the various important mechanisms in SiC. Additionally, I introduce a new mechanism deemed intrinsic atomic-roughness scattering not previously investigated. This new mechanism is calculated in the form of a deformation potential scattering using data extracted from DFT simulations to model the interruption of atomic potential periodicity due to the presence of the interface.

When an electron is moving in a crystal, any number of deviations from a perfect crystal at 0K can cause a perturbation and thus a scattering event. Fig. 3.1 shown below illustrates the family tree of scattering mechanisms which are considered in various semiconductors.

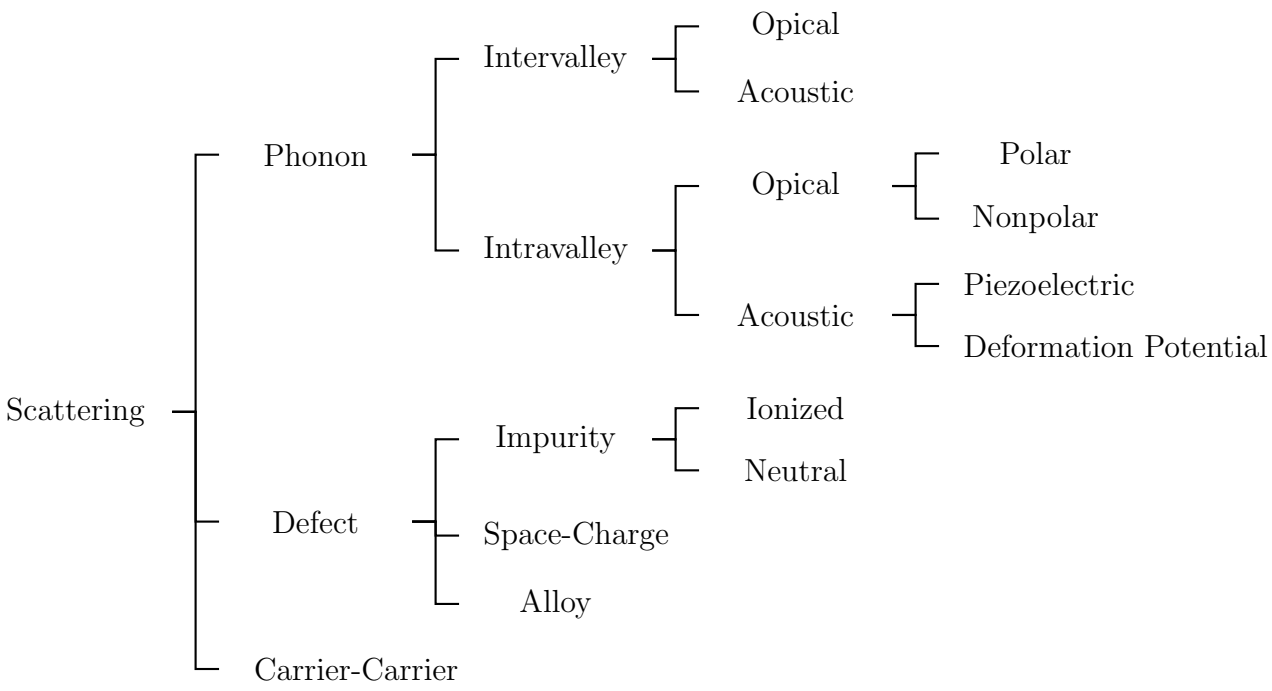

Figure 3.1: Classification of scattering mechanisms in semiconductors. Taken from [6]

These deviations can be treated using the method of perturbation theory,

which treats phonon, impurity, and other interactions as small deviations to the local potential an electron experiences. The perturbation potential changes the Hamiltonian of the system slightly and perturbation theory allows us to determine the resulting eigen energies and wavefunctions from the original solutions. The theory can then be extended to give a scattering rate for an electron in a given state based on the perturbation.

The first order time-dependent quantum perturbation theory is derived as follows. First we start with a general time-dependent Schrdinger equation which all single-electron wavefunctions must obey.

$$i\hbar\frac{\partial\Psi_{\mathbf{k}}(\mathbf{r},t)}{\partial t} = H_0\Psi_{\mathbf{k}}(\mathbf{r},t) \tag{3.1}$$

We also start with an initial unperturbed Hamiltonian H_0 with associated energies $E_{\mathbf{k}}^{(0)}$ and wavefunctions $\psi_{\mathbf{k}}$, for which the solution's are known, as they appear in the time-independent Schrdinger equation.

$$H_0\psi_{\mathbf{k}}^{(0)} = E_{\mathbf{k}}^{(0)}\psi_{\mathbf{k}}^{(0)} \tag{3.2}$$

We can write the corresponding time-dependent solution of the initial wavefunction as:

$$\Psi_{\mathbf{k}}^{(0)}(\mathbf{r},t) = \psi_{\mathbf{k}}^{(0)}(\mathbf{r})e^{-iE_{\mathbf{k}}^{(0)}t/\hbar} \tag{3.3}$$

We now define a perturbed Hamiltonian H as it differs from the initial Hamiltonian H_0 by an arbitrary scaling constant λ times a perturbation Hamiltonian H'.

$$H = H_0 + \lambda H' \tag{3.4}$$

Solutions to any Hamiltonian form a basis, so we can write the solution of the perturbed system as a linear combination of the orthonormal set of solutions of the unperturbed Hamiltonian. The coefficients needed in the sum are in general time-dependent and represent the time variation in the wavefunction due to the perturbation.

$$\Psi(\mathbf{r},t) = \sum_{\mathbf{k}} c_{\mathbf{k}}(t)\Psi^{(0)}_{\mathbf{k}}(\mathbf{r},t) = \sum_{\mathbf{k}} c_{\mathbf{k}}(t)\psi^{(0)}_{\mathbf{k}}(\mathbf{r})e^{-iE^{(0)}_{\mathbf{k}}t/\hbar} \tag{3.5}$$

Substituting this form of the wavefunction into the perturbed Schrdinger equation and canceling terms yields:

$$i\hbar\sum_{\mathbf{k}} \frac{\partial c_{\mathbf{k}}(t)}{\partial t}\psi^{(0)}_{\mathbf{k}}(\mathbf{r})e^{-iE^{(0)}_{\mathbf{k}}t/\hbar} = \lambda\sum_{\mathbf{k}} H' c_{\mathbf{k}}(t)\psi^{(0)}_{\mathbf{k}}(\mathbf{r})e^{-iE^{(0)}_{\mathbf{k}}t/\hbar} \tag{3.6}$$

Multiplying both sides of this equality by the complex conjugate of the wavefunction for another state $\psi^{(0)*}_{\mathbf{k'}}(\mathbf{r})e^{iE_{\mathbf{k'}}t/\hbar}$, we then integrate both sides over all $\mathbf{r}$ resulting in Equation 3.7. Here I've replaced the unperturbed wavefunction in state k with $|\mathbf{k}\rangle$ and the wavefunction for state k' with $\langle\mathbf{k'}|$ using bra-ket notation.

$$i\hbar\frac{\partial c_{\mathbf{k'}}(t)}{\partial t} = \lambda\sum_{\mathbf{k}} c_{\mathbf{k}}(t)\,\langle\mathbf{k'}|\,H'\,|\mathbf{k}\rangle\, e^{i[E_{\mathbf{k'}}-E^{(0)}_{\mathbf{k}}]t/\hbar} \tag{3.7}$$

The expression $\langle k'|\,H'\,|k\rangle$, also known as the matrix element of the perturbation potential represents the transition amplitude between the two states. It's explicit form is shown in Equation 3.8 and resembles an expectation energy calculation of the perturbation but uses two different states in the expression.

$$\langle\mathbf{k'}|\,H'\,|\mathbf{k}\rangle = \int \psi^{(0)*}_{\mathbf{k'}}(\mathbf{r})H'\psi^{(0)}_{\mathbf{k}}(\mathbf{r})d\mathbf{r} \tag{3.8}$$

Assuming the coefficients $c_{\mathbf{k}}(t)$ vary slowly with time for a weak perturbation, we can express them as a power series in λ.

$$c_{\mathbf{k}}(t) = c_{\mathbf{k}}^{(0)} + \lambda c_{\mathbf{k}}^{(1)}(t) + \lambda^2 c_{\mathbf{k}}^{(2)}(t) + \cdots \tag{3.9}$$

By substituting Equation 3.9 into Equation 3.7 and equating the powers of λ on both sides we develop a system of equations proportional to increasing powers of λ which represent different order approximations which can be successively evaluated.

$$i\hbar \frac{\partial c_{\mathbf{k'}}^{(0)}}{\partial t} = 0 \tag{3.10}$$

$$i\hbar \frac{\partial c_{\mathbf{k'}}^{(1)}}{\partial t} = \sum_{\mathbf{k}} \langle \mathbf{k'} | H' | \mathbf{k} \rangle c_{\mathbf{k}}^{(0)} e^{i[E_{\mathbf{k'}} - E_{\mathbf{k}}^{(0)}]t/\hbar}$$

$$i\hbar \frac{\partial c_{\mathbf{k'}}^{(2)}}{\partial t} = \sum_{\mathbf{k}} \langle \mathbf{k'} | H' | \mathbf{k} \rangle c_{\mathbf{k}}^{(1)} e^{i[E_{\mathbf{k'}} - E_{\mathbf{k}}^{(0)}]t/\hbar}$$

$$\vdots \tag{3.11}$$

Assuming the electron exists in a single unperturbed state such that at time $t = 0, c_{\mathbf{k}_i}^{(0)}(0) = 1$ and all other coefficients are 0. With this assumption, to first-order, the coefficient is determined by Equation 3.12, where the perturbation is assumed to be harmonic in nature such that $H' = V' e^{-i\omega t}$.

$$c_{\mathbf{k'}}^{(1)}(t) = \frac{1}{i\hbar} \int_0^t \langle \mathbf{k'} | V' | \mathbf{k}_i \rangle e^{i[E_{\mathbf{k'}} - E_{\mathbf{k}_i}^{(0)} \mp i\hbar\omega]t'/\hbar} dt' \tag{3.12}$$

$$c_{\mathbf{k'}}^{(1)}(t) = \frac{1}{i\hbar} \langle \mathbf{k'} | V' | \mathbf{k}_i \rangle \frac{e^{i[E_{\mathbf{k'}} - E_{\mathbf{k}_i}^{(0)} \mp \hbar\omega]t/\hbar} - 1}{i(E_{\mathbf{k'}} - E_{\mathbf{k}_i}^{(0)} \mp \hbar\omega)/\hbar}$$

$$c_{\mathbf{k'}}^{(1)}(t) = \frac{1}{i\hbar} \langle \mathbf{k'} | V' | \mathbf{k}_i \rangle e^{i\xi t} \frac{\sin(\xi t)}{\xi t} t$$

$$\xi = (E_{\mathbf{k'}} - E_{\mathbf{k}_i}^{(0)} \mp \hbar\omega)/2\hbar \tag{3.13}$$

The probability of the electron being in state k' at time t is given by $|c_{\mathbf{k'}}(t)|^2$

and the transition rate from state k_i to state k' is given by

$$S(\mathbf{k}_i, \mathbf{k'}) = \lim_{t\to\infty} \frac{|c_{\mathbf{k'}}(t)|^2}{t} \tag{3.14}$$
$$S(\mathbf{k}_i, \mathbf{k'}) = \lim_{t\to\infty} \frac{|\langle \mathbf{k'}| V' |\mathbf{k}_i\rangle|^2}{\hbar^2} \left[\frac{\sin(\xi t)}{\xi t}\right]^2 t$$

The squared sinc function term $\left[\frac{\sin(\xi t)}{\xi t}\right]^2$ in the limit as t goes to infinity acts like a Dirac δ-function because the width of the peak becomes very thin. Additionally, instead of integrating to 1, it integrates to π/t when ξ it taken from $-\infty$ to ∞. This observation allows us to replace the term in Equation 3.14 with $\delta(\xi)\pi/t$, which acts as an energy conservation enforcement term in Equation 3.15. The resulting equation illustrates Fermi's golden rule, showing the transition probability from one state to another due to a perturbation is proportional to the matrix element squared. The upper sign in the δ-function corresponds to the emission of a photon with energy $\hbar\omega$, and the lower to the absorption.

$$S(\mathbf{k}_i, \mathbf{k'}) = \frac{2\pi}{\hbar} |\langle \mathbf{k'}| V' |\mathbf{k}_i\rangle|^2 \delta\left(E_{\mathbf{k'}} - E^{(0)}_{\mathbf{k}_i} \mp \hbar\omega\right) \tag{3.15}$$

This result holds true for simple harmonic perturbations which are otherwise constant in time. The calculation also only considers elastic interactions of the electron and phonon. From this transition probability the scattering rate can be determined by multiplying by the number of states per unit volute $(\Omega/(2\pi)^3)$ and integrating over all final states. The delta function will pick out all eligible final states which satisfy energy conservation.

$$W(\mathbf{k}_i) = \frac{\Omega}{(2\pi)^3} \int_0^{2\pi}\int_0^{\pi}\int_0^{\infty} S(\mathbf{k}_i, \mathbf{k'})(k')^2 sin(\theta) dk' d\theta d\phi \tag{3.16}$$
$$W(\mathbf{k}_i) = \frac{\Omega}{\hbar(2\pi)^2} \int_0^{2\pi}\int_0^{\pi}\int_0^{\infty} |\langle \mathbf{k'}| V' |\mathbf{k}_i\rangle|^2 \delta\left(E_{\mathbf{k'}} - E^{(0)}_{\mathbf{k}_i} \mp \hbar\omega\right) (k')^2 sin(\theta) dk' d\theta d\phi$$

Figure 3.2 shows an example of the scattering system in consideration, where initially the electron is in state k. The electron scatters and absorbs a phonon with wavevector q and ends in state k' which is separated by an angle θ from k.

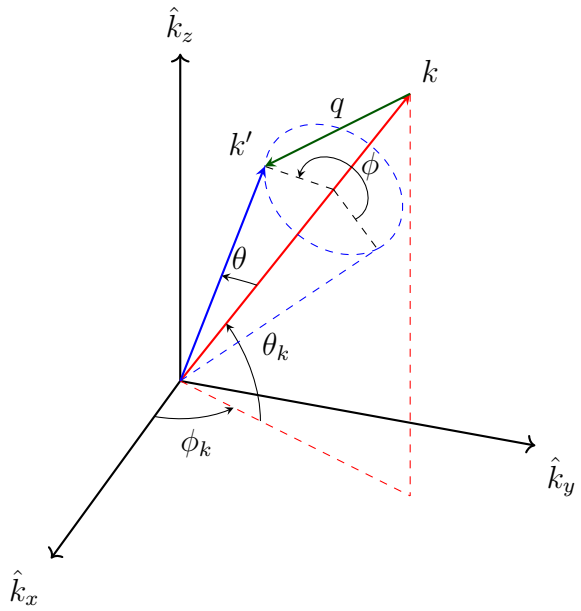

Figure 3.2: Illustration of initial vector **k** scattering to a different state **k'** via the absorption of a phonon with wavevector q. Note: θ is in general not in the same plane as θ_k, which is simply used to define the position of **k**.

3.2 Scattering and Transport Model

Due to the charge of the electron, when an electric field is applied to a semiconductor, electrons in the conduction band experience a force and thus an acceleration in the direction opposite to that of the field. This motion is interrupted by scattering events which we treat as instantaneous events that change the wavevector of the electron. The scattering at each event is caused by one of the many mechanisms shown previously in Figure 3.1 which consist of various phonons representing lattice distortions as well as other lattice perturbations. To study the transport of electrons

in this system, we rely on the semi-classical Monte Carlo method to stochastically simulate an electron as it is accelerated and scattered through the band structure of the crystal. By following the motion of a single electron as it scatters and changes energy, we can build up statistics of velocity and energy which ideally represent the ensemble of electrons simultaneously moving within the crystal. The Monte Carlo method is considered semi-classical because though the scattering mechanisms are treated quantum-mechanically using Fermi's Golden Rule, the free-flight transport between events is treated using classical particle dynamics. As the electron drifts in the electric field, the wavevector changes in time, obeying Equation 3.17 and where the velocity is given by Equation 3.18.

$$\frac{dk}{dt} = \frac{-qF}{\hbar} \tag{3.17}$$

$$V(k) = \frac{1}{\hbar}\frac{dE(k)}{dk} \tag{3.18}$$

The band structure on which the electrons move form energy surfaces within the Brillouin Zone (BZ) of the crystal. The BZ is defined to be the Wigner-Seitz cell constructed for the crystal's reciprocal lattice. By construction, 1^{st} BZ represents all points in reciprocal space closest to an arbitrary reciprocal lattice site. The shape of this zone partitions all of reciprocal space in a periodic fashion and contains every unique wavevector (k-vector) which correspond to the allowed states within the crystal. Associated with these states are quantized energies forming the band structure. By reducing the zone by all symmetries of the crystal, we obtain what is

known as the irreducible wedge which contains the non-redundant information of the energy bands. The edges and vertices of this wedge correspond to highly symmetric points and directions of the reciprocal lattice. To plot the full band structure, a four dimensional plot would be required, so instead a representative sample of the zone is taken by following the edges of the irreducible wedge to form a path between the high symmetry points. The allowed energies at each k-vector are plotted against the distance traveled along the path. Fortunately, the band extrema almost always lay along these symmetry directions so the band gap as well as important valleys of the conduction band and other features of the energy landscape are revealed in this manner.

In contrast to the familiar Si which has a diamond crystal structure and fcc lattice, the most electrically significant polytypes of SiC have a wurtzite crystal structure which correspond to a hexagonal lattice. The BZ of the hexagonal lattice is simply a hexagonal prism. A depiction of the hexagonal BZ is shown in Figure 3.3 along with it's irreducible wedge and high-symmetry points which are visited in band structure diagrams.

The band structure for 4H-SiC is known to have its conduction band minimum at the M point, making it an indirect gap material with 6 equivalent minima in the BZ. In general, it is common to approximate the energy dispersion relation near the conduction band minima to be parabolic such that energy E is proportional to the squared magnitude of the wavevector k. However, in wide bandgap semiconductors like SiC where electric fields allow carriers to gain energy such that they reside away

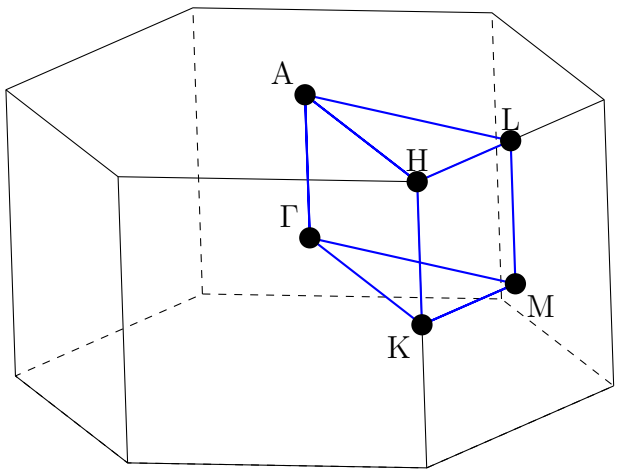

Figure 3.3: Brillouin Zone of a hexagonal lattice.

from the band minimum, a non-parabolicity factor α is introduced as in Equations 3.19 and 3.20 to better account for the true shape of the bands.

$$\gamma(E) = E(1+\alpha E) = \frac{\hbar^2 k^2}{2m^*} \qquad \text{(spherical)} \tag{3.19}$$

$$\gamma(E) = E(1+\alpha E) = \frac{\hbar^2}{2}\left(\frac{k_l^2}{m_l^*} + \frac{2k_t^2}{m_t^*}\right) \qquad \text{(ellipsoidal)} \tag{3.20}$$

For many semiconductors including SiC, the constant energy surfaces are ellipsoidal and have a different masses depending on the direction of the field relative to the valley. These masses are denoted as the longitudinal effective mass m_l aligned radially out from the center of the BZ to the location of the valley, and transverse effective mass m_t for transport in the plane perpendicular to the longitudinal direction.

From my full band structure calculation showed previously in Figure 2.1, we can extract a simplified band model containing only the important energy minima of the conduction band and the maximum of the valence band. These important

bands are shown in Figure 3.4, taken from [8].

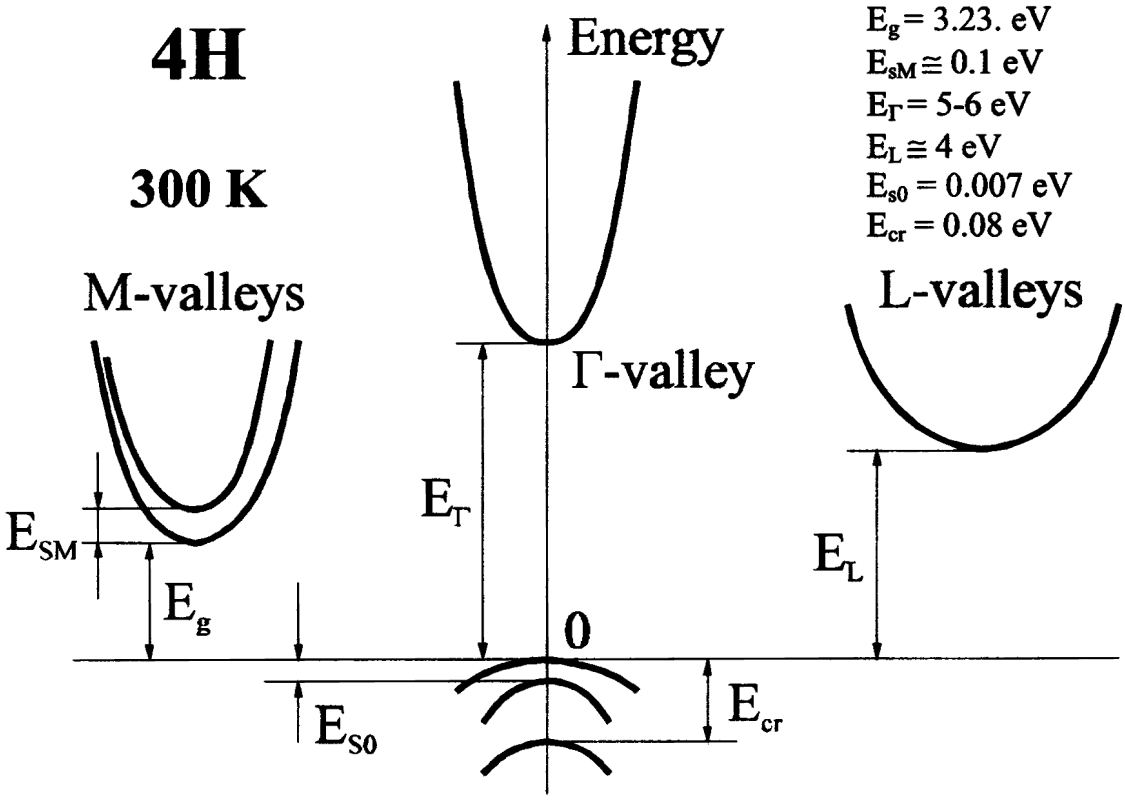

Figure 3.4: Simplified band illustration for 4H-SiC with associated energies from literature [7] (Figure from [8]).

Due to the small difference in energy of the two lowest bands in the M valley, we will initially treat this as a doubly degenerate valley as a first approximation, so scattering rates are multiplied by a factor of 2 because of the doubling of the density of states. Additionally, the calculated overlap integrals of the wavefunctions from the minimum at any one M valley to the other 5 equivalent M valleys are small (0.005, 0.162, 0.016, 0.162, 0.005) and expected to be similarly small for points near the minimum [40]. This indicates that there is little optical intervalley scattering compared to intravalley scattering so we will approximate the value of the overlap to be 1 when scattering within a valley and 0 when scattering to other valleys.

The Monte Carlo simulation I performed in this work uses deformation potential values fitted by Hjelm et al. [41] as well as the corresponding phonon temperatures and other physical constants which are reproduced in Table 3.1. The phonon temperatures are related to the phonon energies and frequencies via Equation 3.21.

$$E_{ph} = \hbar\omega_{ph} = k_B T_{ph} \tag{3.21}$$

Table 3.1: Phonon and material properties taken from the model used by Hjelm [40]

Parameter	**Value**
Acoustic Deformation Potential $\boldsymbol{D_A}$ (eV)	19
Polar-optical Phonon Temperature (K)	1393
Nonpolar Optical Deformation Potential $\boldsymbol{D_t K}$ (eV/cm)	12e8
Nonpolar Optical Phonon Temperature (K)	989
Density $\boldsymbol{\rho}$ (g/cm^3)	3.2
Velocity of Sound $\boldsymbol{\nu_s}$ (cm/s)	13.73e5
M Valley Longitudinal Effective Mass $\boldsymbol{m_l}$	0.29
M Valley Transverse Effective Mass $\boldsymbol{m_t}$	0.42
Nonparabolicity of M valley $\boldsymbol{\alpha}$ (eV^{-1})	0.4

3.3 Scattering Rate Calculations

Electrons moving under the influence of an applied field accelerate until they are scattered into a different state from one of numerous mechanisms. Each scattering event corresponds to the emission or absorption of a phonon which allows for the change in the electron's momentum. Because phonons are bosons, their occupancy is determined by Bose-Einstein statistics and the associated distribution function in Equation 3.22 often appears in the scattering rate formulae for different

mechanisms.

$$N_q(x) = \frac{1}{e^x - 1} \tag{3.22}$$

As the electron travels through the crystal scattering, its energy is constantly changing which affects the number of states available for it to scatter into and thus the probability of scattering in the first place, making each scattering rate a function of electron energy. Additionally, the various scattering mechanisms considered all have different perturbation potentials which correspond to different energy-dependent scattering rate formulae. For simple formulae, the integrals may have a closed form which can be trivially implemented into the Monte Carlo code. However, some of the rate formulae involve complex integrals which must be evaluated numerically. The calculations can then be stored into a lookup table and referenced at each iteration to speed up the computation. In the following sections I only include scattering rate formulas for the dominant mechanisms in SiC.

3.3.1 Acoustic

Acoustic phonons represent acoustic vibration modes of atoms in the crystal. These phonons are generally lower frequency than other phonons and arise due to thermal excitations.

The scattering probability for acoustic phonons is calculated to account for inelastic scattering with ellipsoidal equienergy surfaces and nonparabolic bands. The derivation of which is given in the landmark paper by Jacoboni and Reggiani [42],

and the result shown in Equations 3.23 and 3.24.

$$P_A^{ab}(E) = \frac{m_d^{1/2}(k_BT)^3 D_A^2}{2^{5/2}\pi\hbar^4 v_s^4 \rho}\gamma(E)^{-1/2}\times \left[(1+2\alpha E)\int_{x_{1,a}}^{x_{2,a}} N_q(x')x'^2dx' + 2\alpha k_b T\int_{x_{1,a}}^{x_{2,a}} N_q(x')x'^3dx'\right] \quad (3.23)$$

$$P_A^{em}(E) = \frac{m_d^{1/2}(k_BT)^3 D_A^2}{2^{5/2}\pi\hbar^4 v_s^4 \rho}\gamma(E)^{-1/2}\times \left[(1+2\alpha E)\int_{x_{1,e}}^{x_{2,e}} [N_q(x')+1]x'^2dx' - 2\alpha k_b T\int_{x_{1,e}}^{x_{2,e}} [N_q(x')+1]x'^3dx'\right] \quad (3.24)$$

Here, the upper equation is the probability for phonon absorption and the lower for phonon emission. The limits for integration are derived from the energy and momentum conserving delta function and are shown in Table 3.2. The associated integrals are evaluated numerically to take into account the exact form of N_q.

Table 3.2: Limits of integration used in acoustic phonon scattering probability calculations. Here, $C(\alpha) = 4E_s/(k_BT(1-4\alpha E_s))$ and $E_s = m_d v_s^2/2$

Absorption	**Emission**	**Condition**
$x_{1,a} = C(\alpha)\left[\sqrt{E_s}(1+2\alpha E) - \sqrt{\gamma}\right]$ $x_{2,a} = C(\alpha)\left[\sqrt{E_s}(1+2\alpha E) + \sqrt{\gamma}\right]$	$x_{1,e} = N/A$ $x_{2,e} = N/A$	$\gamma < \frac{E_s}{1-4\alpha E_s}$
$x_{1,a} = 0$ $x_{2,a} = C(\alpha)\left[\sqrt{\gamma} + \sqrt{E_s}(1+2\alpha E)\right]$	$x_{1,e} = 0$ $x_{2,e} = C(\alpha)\left[\sqrt{\gamma} - \sqrt{E_s}(1+2\alpha E)\right]$	$\gamma > \frac{E_s}{1-4\alpha E_s}$

3.3.2 Non-Polar Optical Scattering

Non-polar optical scattering corresponds to excitations of a polar optical vibration mode of the crystal. These modes are generally excited by interaction with light.

Analytically, the scattering rate for optical phonons is given by Equation 3.25, a result also derived in the Jacoboni and Reggiani paper [42]. Here, the resulting equation is formulated to account for ellipsoidal, nonparabolic bands. This scattering rate is used to account only for intravalley scattering and intervalley scattering is regarded as small enough to be neglected.

$$P_{op}(E) = \frac{(D_t K)^2 m_d^{(3/2)}}{\sqrt{2}\pi\hbar^3\rho\omega_{op}} \begin{bmatrix} N_{op} \\ N_{op}+1 \end{bmatrix} \sqrt{\gamma(E \pm \hbar\omega_{op})}\,[1 + 2\alpha(E \pm \hbar\omega_{op})] \tag{3.25}$$

3.3.3 Polar Optical Scattering

Polar optical phonons are excitations of the polar optical modes of a lattice and occur when different atoms in the primitive unit cell of an ionic semiconductors vibrate out of phase with each other. This oscillation causes an alternating electric field and changing potential that can scatter carriers. The analytical expression shown in Equation 3.26 is taken from [43].

$$P_{pop}(E) = \frac{e^2\sqrt{m_d}\omega_{pop}}{\sqrt{2}\hbar}\left(\frac{1}{\kappa_\infty} - \frac{1}{\kappa_0}\right)\frac{1+2\alpha E'}{\sqrt{\gamma(E)}} F_0(E,E') \begin{bmatrix} N_q \\ N_q+1 \end{bmatrix} \tag{3.26}$$

Here, $E' = E \pm \hbar\omega_{pop}$ corresponding to energy after emission or absorption of the phonon. The other terms are calculated as:

$$F_0(E,E') = C^{-1}\left\{A \ln\left|\frac{\gamma^{1/2}(E)+\gamma^{1/2}(E')}{\gamma^{1/2}(E)-\gamma^{1/2}(E')}\right| + B\right\}$$

$$A = \{2(1+2\alpha E)(1+\alpha E') + \alpha[\gamma(E)+\gamma(E')]\}^2$$

$$B = -2\alpha\gamma^{1/2}(E)\gamma^{1/2}(E')\{4(1+\alpha E)(1+\alpha E') + \alpha[\gamma(E)+\gamma(E')]\}$$

$$C = 4(1+\alpha E)(1+\alpha E')(1+2\alpha E)(1+2\alpha E')$$

3.4 Novel Interface Atomic Roughness Scattering

3.4.1 Existing Surface Roughness Model

In this work, I investigate the inclusion of a novel scattering mechanism to model the most fundamental scattering due to the break in periodicity at an ideal semiconductor-oxide interface which will be referred to as atomic roughness scattering. Presently, the rather large scattering contribution in SiC at the interface is caused by surface roughness scattering [44]. The surface roughness is modeled as a series of bunched steps with size range around 1 to 5 nanometers [27]. Steps form due to the presence of a crystallographic miscut of around 4-8° which enables the growth of homoepitaxial layers in the c-direction without the need for the presence of screw dislocations [45]. The steps in conjunction with the gate-induced surface field perpendicular to the interface cause a perturbation to the potential that electrons in the channel see as defined by Equation 3.27.

$$\Delta\phi(x,y,z) = \frac{d\phi(z)}{dz}\Delta z(x,y) \tag{3.27}$$

Here, the model assumes the simple form of the surface perpendicular field times the height of the steps. From the form of the perturbation, we can see that at higher surface fields the level of interaction and thus the rate of scattering increases. At high surface fields this mechanism is predicted to dominate in 4H-SiC MOSFETs [27]. In the typical implementation of this mechanism, a roughness power spectrum

is introduced, and assumes the form given by [44]:

$$S(q) = \frac{\pi \Delta^2 L^2}{\left[1 + \frac{q^2 L^2}{2}\right]} \tag{3.28}$$

In this standard but relatively simplistic model, Δ represents the average step amplitude and L is the correlation length or the standard deviation of the step separation. This power spectrum corresponds to an exponential autocovariance function given in Equation 3.29 [44, 46] and the transition rate in Equation 3.30. The values of Δ and L are fitted to experimental data by [27] to be 3.5nm and 7nm respectively and account for the distribution of nano and macro-scale steps.

$$\Re_\delta = \langle \delta(\mathbf{r}), \delta(\mathbf{r} - \mathbf{r'}) \rangle = \Delta^2 e^{-r/L} \tag{3.29}$$

$$S(k, k', z) = \frac{2\pi^2 e^2 \Delta^2 L^2 F_\perp^2(z)}{\hbar \left(1 + \frac{q^2 L^2}{2}\right)} \delta(E - E') \tag{3.30}$$

3.4.2 My Perturbation and DFT-Based Model: Calculation and Scattering Rate Results

In our investigation of surface roughness scattering, we have decided to study the fundamental scattering for an ideal 4H-SiC/SiO_2 interface that exists despite the presence of a miscut. Scattering arising due to the miscut can be integrated into the theory later as an additive potential. In our model, inversion layer electrons have their energies quantized into subbands of a quantum well near the interface so that motion is restricted to the plane of the interface. The scattering mechanism is treated using the well-known perturbation potential form given earlier in Equation 3.16. In this work, we developed a novel technique for extracting the actual form of

this potential from a series of DFT calculations, rather than an approximation, and should be applicable to any conceivable interface. To extract the perturbation, we first perform a relaxation calculation on a 4H-SiC/SiO_2 interface supercell (Figure 3.5) to determine the energetically favorable atomic configuration. Then we perform another relaxation of a pure 4H-SiC bulk structure. The converged DFT calculations result in a value of the potential everywhere inside each of the supercells. We take the potential field from each calculation and align the bulk potential with the potential far away from the interface, then by subtraction we determine the potential difference the electron experiences due to the presence of the interface. The perturbation potential function varies in the plane of the interface based on the location of the bulk atoms and the oxide atoms. The perturbation decays to zero with depth into the bulk of the semiconductor as the effect of the presence of the interface on the periodic bulk potential diminishes.

Figure 3.6 shows the extracted potential at the interface which we take to be the average height of the first oxygen layer. The potential here contains all constituent potential components found in the Kohn-Sham Hamiltonian: ionic, Hartree (electron-electron), and exchange-correlation.

Subtracting this interface potential from the periodic bulk potential, we obtain a perturbation potential, shown in Figure 3.7. The deep wells in the figure, shown in blue, correspond to the oxygen atom locations. The regularly spaced yellow potential barriers are the inverted carbon atom wells, showing where the carbon atoms of the

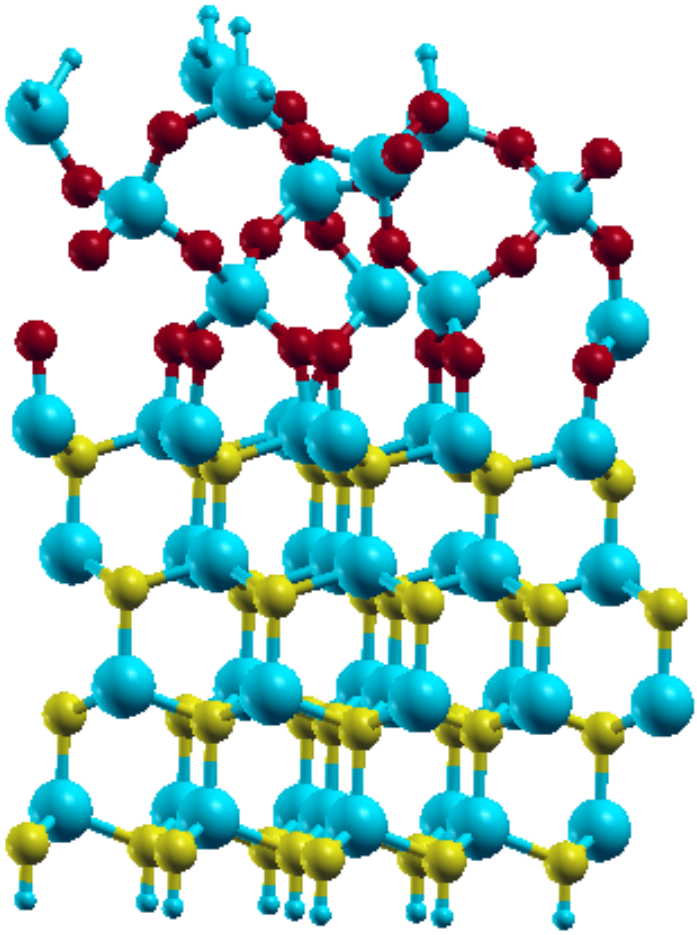

Figure 3.5: 4H-SiC/SiO_2 interface supercell created by [9], used to extract calculated potential.

bulk would be if the bulk continued past the interface. Since the scattering rate depends on the square of the perturbation potential, the choice of sign is arbitrary.

To evaluate the matrix element given in Equation 3.8, we need to assume a form for the initial and final states of the electron. Because this scattering is occurring in the channel at the surface of a MOSFET device, there exists a mesoscopic scale potential well due to band bending near the semiconductor surface and the presence of a band offset between the semiconductor and insulator. The shape of the well is regularly approximated in literature to be triangular and the channel

electrons which reside there are confined only in the z dimension towards the bulk crystal [44,47]. The electrons in the well act similarly to a particle in a box, residing in discrete energy states known as subbands which occur on top of the crystal band structure, shown in Figure 3.8.

From these assumptions, we use separation of variables to break the Schrdinger equation into an equation with only x and y dependence, and an equation with purely z dependence. The resulting x and y dependent equation takes the form of a free electron equation so the electronic wavefunction in the x,y (interface) plane is taken to be a plane wave. In the z dimension, the standard analytical solution for a particle in an infinite triangular well is used [47]. The solutions are known to consist of Airy functions (Ai[z]), shifted to contain the appropriate number of zeros for each subband energy level [48]. The full form of the wavefunction is shown in Equation 3.31 and associated subband energies (referenced to the conduction band energy E_C) in Equation 3.32.

$$\Psi_n = \frac{1}{\sqrt{\Omega}} e^{i(k_x x + k_y y)} \psi_n(z) \tag{3.31}$$

$$\psi_n(z) = A_n \cdot \mathrm{Ai}\left[-\left(\frac{2m^* eF}{\hbar^2} \right)^{(1/3)} \left(z - z_i - \frac{E_n}{eF} \right) \right] \Theta(z_i - z)$$

$$A_n = \frac{1}{\sqrt{\left(\frac{\hbar^2}{2m^* eF}\right)^{(1/3)} \mathrm{Ai}'\left[-\left(\frac{3\pi}{2}\left(n - \frac{1}{4}\right)\right)^{(2/3)} \right]}}$$

$$\mathrm{Ai}[\xi] = \frac{1}{\pi} \int_0^\infty \cos\left(\frac{t^3}{3} + \xi t \right) dt$$

$$E_n = \left(\frac{e^2 \hbar^2 F^2}{2m^*} \right)^{(1/3)} \left(\frac{3\pi}{2} \left(n - \frac{1}{4} \right) \right)^{(2/3)} \tag{3.32}$$

Here, Ω is the interface area, k_x and k_y are the 2d wavevector components of

the electron in the plane of the interface, A is for Airy function normalization, F is the surface electric field value, z_i is the interface location, n is the subband index, and Θ is the Heaviside function. The wavefunctions here are the solutions obtained for an infinite triangular well of slope F with an infinite conduction band offset. The actual offset for a 4H-SiC/SiO_2 system is experimentally determined to be 2.7eV, which is quite large compared to the subband energies for typical surface field values ($E_1 = 0.18eV@F = 1MV/cm$) so the approximation is quite reasonable.

Substituting our assumed form of the wavefunctions into Equation 3.15 results in the transition rate S(k,k') from state k to state k' shown in Equation 3.33. The delta function in this equation contains the total energy conservation condition and assumes that the energy of the phonon in the exchange is negligible, as is typically done for deformation potential interactions. To obtain the total scattering rate $W_{2D}(k_{||}, n)$ out of state k, we sum over all eligible final states k' as shown in Equation 3.34.

$$S(k_{||}, k'_{||}, n, n') = \frac{2\pi}{\hbar\Omega} \iint_{\Omega} \int_{z_i}^{\infty} \left| e^{-i(k'_x x + k'_y y)} \psi^*_{n'}(z) \Delta V(x, y, z) e^{i(k_x x + k_y y)} \psi_n(z) \right|^2 \delta\left(\frac{\hbar^2 |k'_{||}|^2}{2m^*} + E_{n'} - \frac{\hbar^2 |k_{||}|^2}{2m^*} - E_n \right) dz dy dx \quad (3.33)$$

$$W(k) = \frac{\Omega}{(2\pi)^2} \sum_{n'} \int S(k_{||}, k'_{||}, n, n') d\mathbf{k'}_{||} \quad (3.34)$$

The delta function in Equation 3.33 which enforces energy conservation in turn imposes allowed magnitudes of $k'_{||}$, shown in Equation 3.35, depending on the initial

and final subband energies.

$$k'_{\shortparallel} = \sqrt{(k_{\shortparallel})^2 + \frac{2m^*}{\hbar^2}\left(E_n - E_{n'}\right)} \tag{3.35}$$

After computing the transition rate for a given initial state $k_{\shortparallel}, n$, we see that the allowed final states lay in concentric rings in the k_x, k_y plane. This happens because when the electron scatters to a higher subband, it gains potential energy and must lose kinetic energy to conserve total energy, thus its $|k_{\shortparallel}|$ must shrink. Conversely, when the electron scatters to a lower energy subband, it loses potential energy and gains kinetic energy, creating the larger rings. It is also possible for electrons to have kinetic energy too small, such that the energy required to scatter to the next higher band is larger than the amount of kinetic energy available to be lost, making this a forbidden transition. Figure 3.9 shows the transition rates which are calculated for all allowed $k'_{\shortparallel}$, given the initial state in the second subband $(n = 2)$ with initial kinetic energy of 1eV.

To determine the total scattering rate out of our given initial state, we simply integrate the transition rates over the rings of allowed states, and then sum over all rings. The calculation has been performed for various surface fields and shows the 2D atomic roughness scattering rate as a function of electron energy in Figure 3.10. The discontinuities in the scattering rate arise when the electron gains enough energy to access each higher subband which increases the scattering probability by increasing the number of available states. It is worth noting that the scattering rate calculated with the traditional combined empirical surface model is proportional to the square of the gate field at the interface $(F_{\perp}^2)$ [39, 44, 49–52], and the same

holds for my first-principles calculated scattering rates. This result is confirmed by plotting the log of the scattering rate against the log of the field, shown in Figure 3.11, where the exponent is given by the slope of resulting straight lines. From the results of my scattering rate calculations, we see that the intrinsic atomic-roughness scattering rates come out to be between 1×10^{11} and 5×10^{11} per second for a range of typical gate-induced surface fields from 0.1 MV/cm to 1.0 MV/cm.

3.4.3 Comparison of Intrinsic and Extrinsic Mobilities

Component mobilities due to different mechanisms add according to Matthiessen's rule. In Equation (3.36) total mobility μ_{Tot} is separated into its intrinsic (μ_{int}) and extrinsic (μ_{ext}) components. The intrinsic mobility is itself comprised of material-dependent mobilities such as the bulk (μ_B), surface phonon (μ_{SP}), and atomic-scale surface roughness (μ_{AR}). Extrinsic mobility components are associated with process-dependent issues such as the Coulombic scattering from interface traps (μ_C), and the surface roughness (μ_{SR}) mainly due to nanometer-scale interface steps resulting from a crystallographic miscut included to promote homoepitaxial growth. The bulk mobility term is included with the intrinsic terms because we are focused on interface issues, independent of the substrate doping. Note that in previous works the CESRM scattering approach inherently lumps together all non-Coulombic interface effects, and we calculate this value for comparison. The extrinsic miscut steps and the bunching thereof are the largest roughness features present in calculations fit to experimentally measured interfaces, so to a good approximation, we consider this

Table 3.3: Important component mobilities at the SiC/SiO_2 interface for T=300K

$\mu\ cm^2/Vs$	$E_\perp\ MV/cm$		
	0.1	0.5	1
μ_B	1070		
μ_{SP}	1470	560	400
μ_{AR}	4.4×10^7	1.8×10^6	4.8×10^5
$\boldsymbol{\mu_{int}}$	**620**	**370**	**290**
μ_{SR}	350	14	4
μ_C	429	447	591
$\boldsymbol{\mu_{ext}}$	**193**	**14**	**4**
$\boldsymbol{\mu_{Tot}}$	**147**	**13**	**4**

term to be purely extrinsic [51].

$$\frac{1}{\mu_{Tot}} = \frac{1}{\mu_{int}} + \frac{1}{\mu_{ext}} = \tag{3.36}$$
$$(\frac{1}{\mu_B} + \frac{1}{\mu_{SP}} + \frac{1}{\mu_{AR}}) + (\frac{1}{\mu_C} + \frac{1}{\mu_{SR}} + \cdots)$$

To show their relative contributions to the total mobility, the other predominant scattering mobilities present at the SiC/SiO_2 interface are quantified and then compared. These mobilities are presented in Table 3.3 and consist of values calculated based on models and data from Potbhare et al. [1]. The details of these calculations are shown in Appendix C. Note that the total mobility measured experimentally is highly dependent on oxide quality, the interface state density and the surface roughness profile. The values calculated here are representative of a typical device and are also consistent with the component mobilities found by Uhnevionak et al. [52]. In table 3.3, intrinsic mobilities are separated from extrinsic mobility components.

For the highest gate fields we used, the total intrinsic mobility μ_{int} becomes approximately 290 cm^2/Vs, significantly higher than the corresponding extrinsic mobility μ_{ext} of 4 cm^2/Vs. At lower fields, the intrinsic mobility is approximately 620 cm^2/Vs compared to the extrinsic mobility of 193 cm^2/Vs. The important observation here is that by reducing the mobility limiting effects of the extrinsic terms, mobility improvements on the order of 4 to 70 times can be expected, depending on the field. These benefits, however, hinge on future improvements in fabrication techniques with special care taken to minimize the extrinsic scattering effects. One key method of reducing extrinsic surface roughness is likely to come from eliminating the 4° to 8° Si-face miscut which gives rise to surface steps and step bunching. Though the practice of including a miscut is ubiquitous for growing homoepitaxial layers in industry, it is expected to be a major source of mobility limiting surface scattering, especially at high gate fields.

On-axis homoepitaxial growth of SiC has been a topic of research with some successes, in particular the C-face $(000\bar{1})$ of 4H-SiC seems to be the easiest to control the polytype [53], though success has also been seen on the Si-Face (0001) where spiral growth is mediated by screw-dislocations [54,55]. These on-axis growth techniques are also shown to reduce the basal plane dislocation density and improve epitaxial layer quality [53,54] but island growth using these techniques may prevent extrinsic surface roughness from being eliminated completely. Other works have investigated the effect of transport versus miscut angle and also found that mobility generally improves when miscuts are reduced. While the more conventional [56] Si-face is considered in this work, experiments have been done with electron transport

along on the C-face [56, 57] and a-face $(11\bar{2}0)$ [58, 59].

In the C-face experiment by Fukuda et al. [57], higher surface roughness was confirmed to exist by TEM images for larger miscut angles. MOSFETs fabricated on substrates with a vicinal 0.8°off-angle cut showed peak field-effect channel mobility of 92.3 cm^2/Vs compared to 84.5 cm^2/Vs for 8°off-angle devices [57]. Hijikata et al. [56] also concluded from C-face experiments that smaller off-angle devices should lead to better device performance.

Harada et al. [58] performed mobility measurements on trench MOSFETs fabricated on 0.7° C-face vicinal wafers where the channel plane was aligned at various angles relative to the a-face. A peak mobility of 160 cm^2/Vs was achieved when the channel was aligned to the the a-face, compared to the lowest mobility of 110 cm^2/Vs angled half way between a-faces.

Experiments were also performed on trench devices fabricated on wafers with a 8°surface miscut-angle. The deviation from vertical trench sidewalls compounds with the wafer miscut angle resulting in the channel plane deviating further from the exact a-face plane. Under these conditions Harada found the peak mobility to reduce from 160 cm^2/Vs to 70 cm^2/Vs [58]. Yano et al. [59] found similar results, reducing their peak mobility from 66 cm^2/Vs to a low of 6 cm^2/Vs for the greatest channel misalignment.

The aforementioned experimental work argues that channel misalignment to important crystallographic planes reduces channel mobility. These results are congruent with our calculations which predict much higher mobility if miscut-induced surface roughness is reduced.

3.5 Conclusion

In this work I classified the traditional mobility terms into intrinsic and extrinsic components, where the intrinsic are purely due to inherent material properties, and the extrinsic are due to electron scattering arising from device fabrication. In particular, the intrinsic components are separated from the extrinsic components of surface roughness mobility, which have previously been computed by lumping these components together. The intrinsic surface roughness is due to atomic-scale potential-variation and the presence of the interface, while the extrinsic is largely due to the wafer miscut generating nanometer-scale steps and step bunches.

I found that the intrinsic mobility of the 4H-SiC/SiO_2 interface is much larger than the extrinsic mobility. This is especially apparent with respect to surface roughness scattering, where extrinsic mobility due to miscut roughness is orders of magnitude lower than intrinsic surface mobility due to atomic-scale roughness. This result is found to be largely insensitive to the magnitude of the perturbation, where even if the perturbation is doubled, the extrinsic surface roughness dominates the degradation of mobility. This result argues for further developing on-axis (or close to on-axis) MOS technology for SiC. Experimental results support this conclusion as well [56–59].From these experiments, evidence is clear that deviations from ideal crystallographic planes create longer-range disorder and increased surface roughness. In summary, we conclude that the interface of SiC/SiO_2 does not intrinsically lead to low mobility and that process-induced imperfections are the cause of the interface mobility degradation experimentally observed.

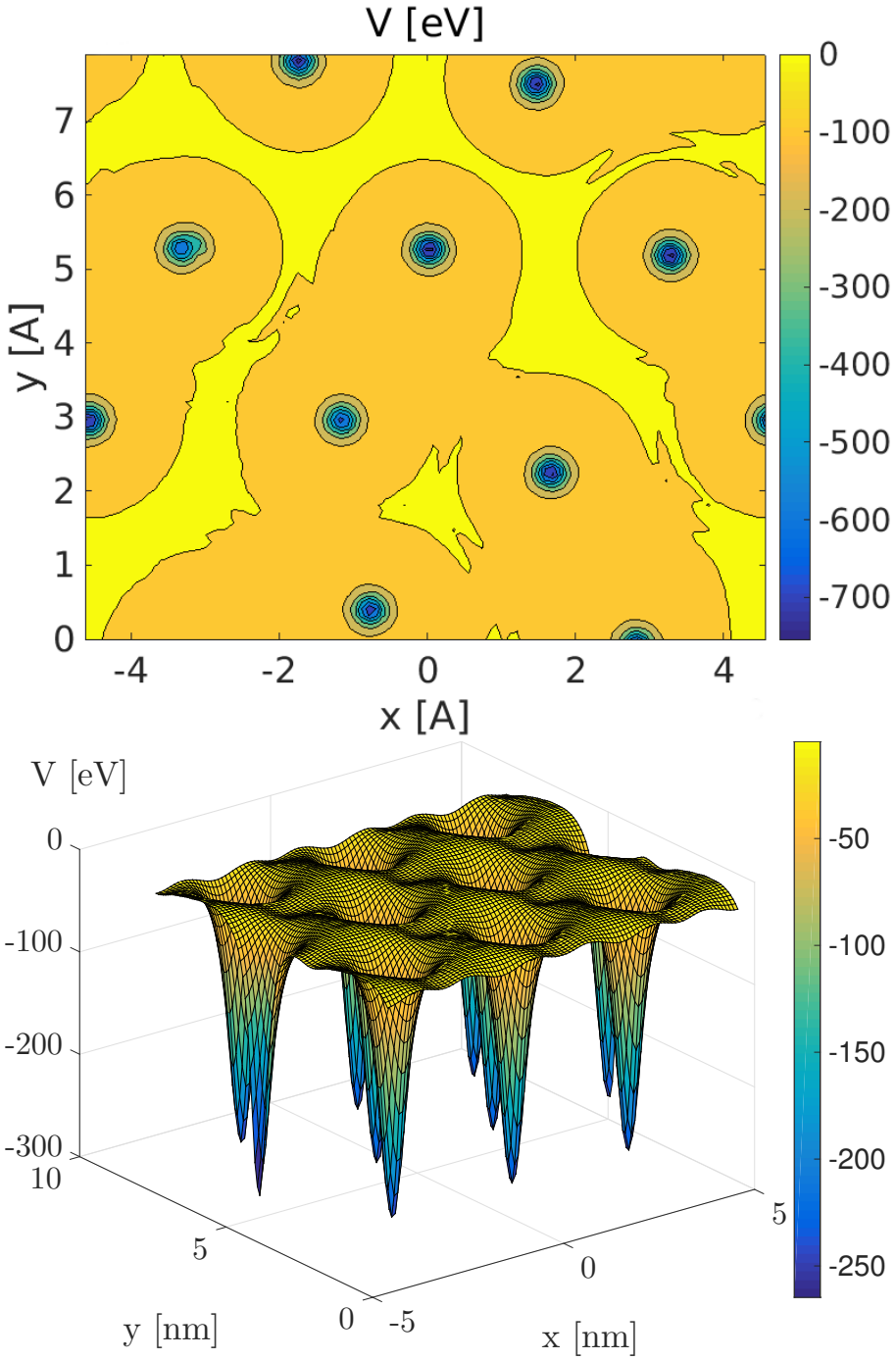

Figure 3.6: Interface potential taken at the semiconductor-insulator interface. The blue (well) areas depicted are within the oxygen atoms.

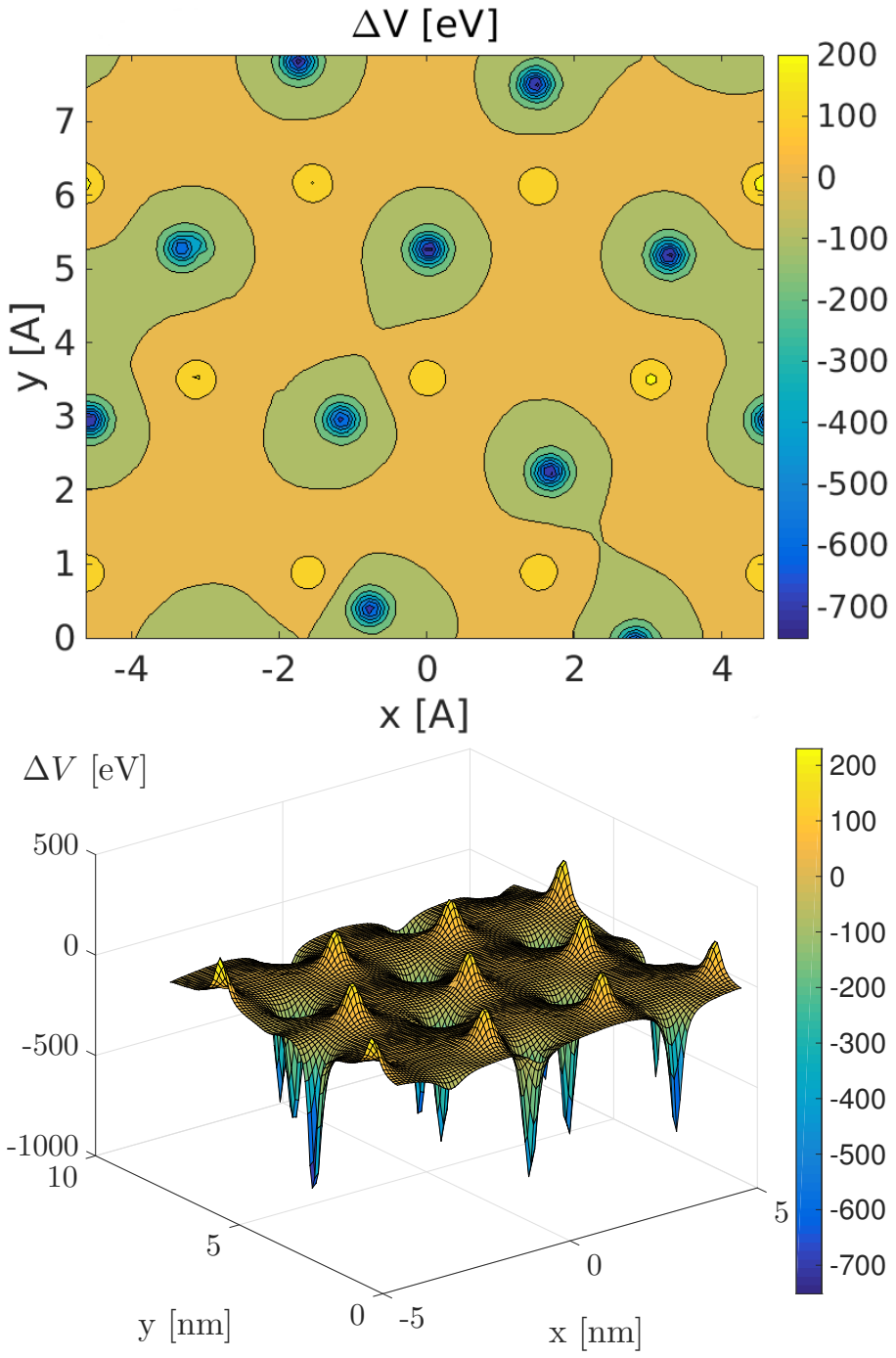

Figure 3.7: Interface perturbation potential taken at the semiconductor-insulator interface. The blue (well) areas are the oxygen atoms, and the yellow (peak) areas are where the carbon sites are located if the bulk continued beyond the interface.

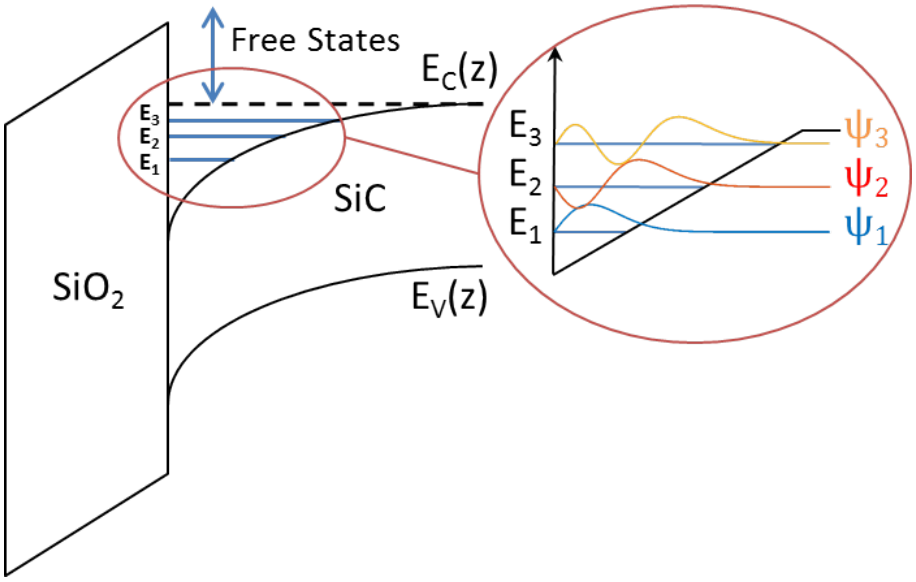

Figure 3.8: Real-space band extrema cartoon depicting the well structure which forms at the SiC-SiO_2 interface when a channel is formed. The subbands are enumerated 1, 2, 3... and exist as states found only within the well near the surface. On the right, the triangular approximation to the well is made and the corresponding approximate wavefunctions are shown which increase in number of nodes with energy.

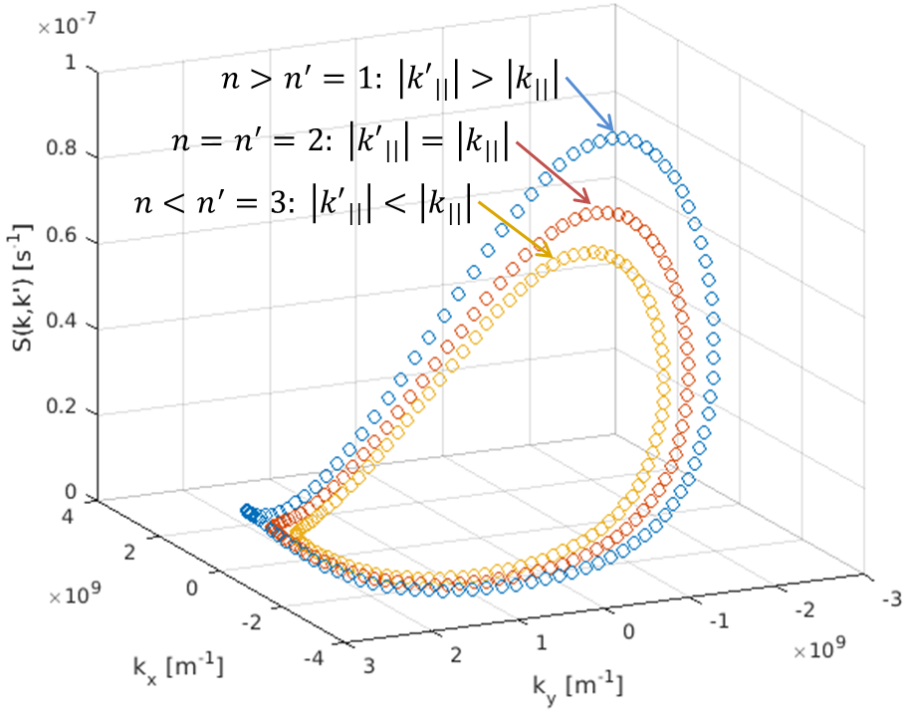

Figure 3.9: Calculated transition rates for electrons due to atomic-roughness scattering with DFT-extracted interface perturbation potential. Initial state has 1eV of kinetic energy and is in the second subband of a triangular well with surface field of 1MV/cm. Scattering within the second subband is shown in red, scattering to the third subband in orange, and to the first subband in blue.

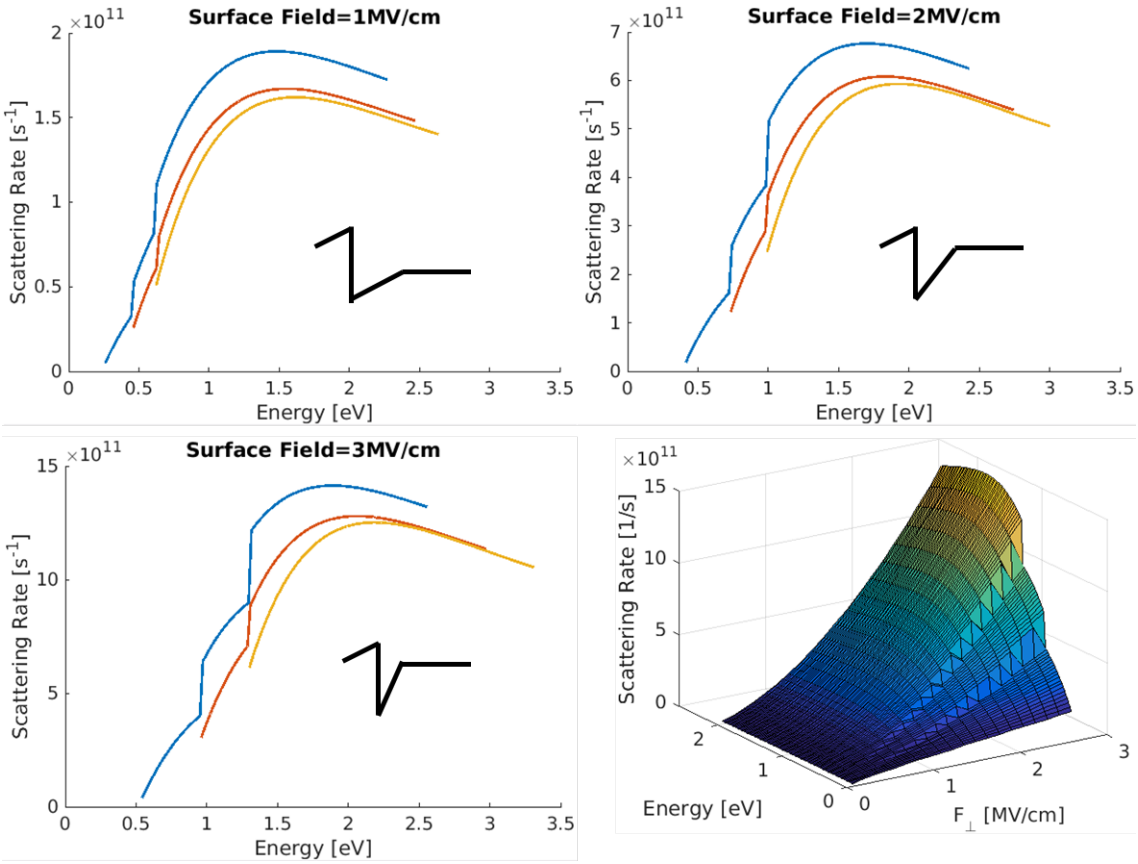

Figure 3.10: 2D atomic roughness scattering rates for electrons in the 1^{st} (blue), 2^{nd} (red), and 3^{rd} (orange) subbands. The x axis shows total energy of the electron, so each curve begins at the corresponding subband energy for the given field. Insets show the relative shape of the triangular well that each plot represents. Bottom right plot contains both energy and field variation.

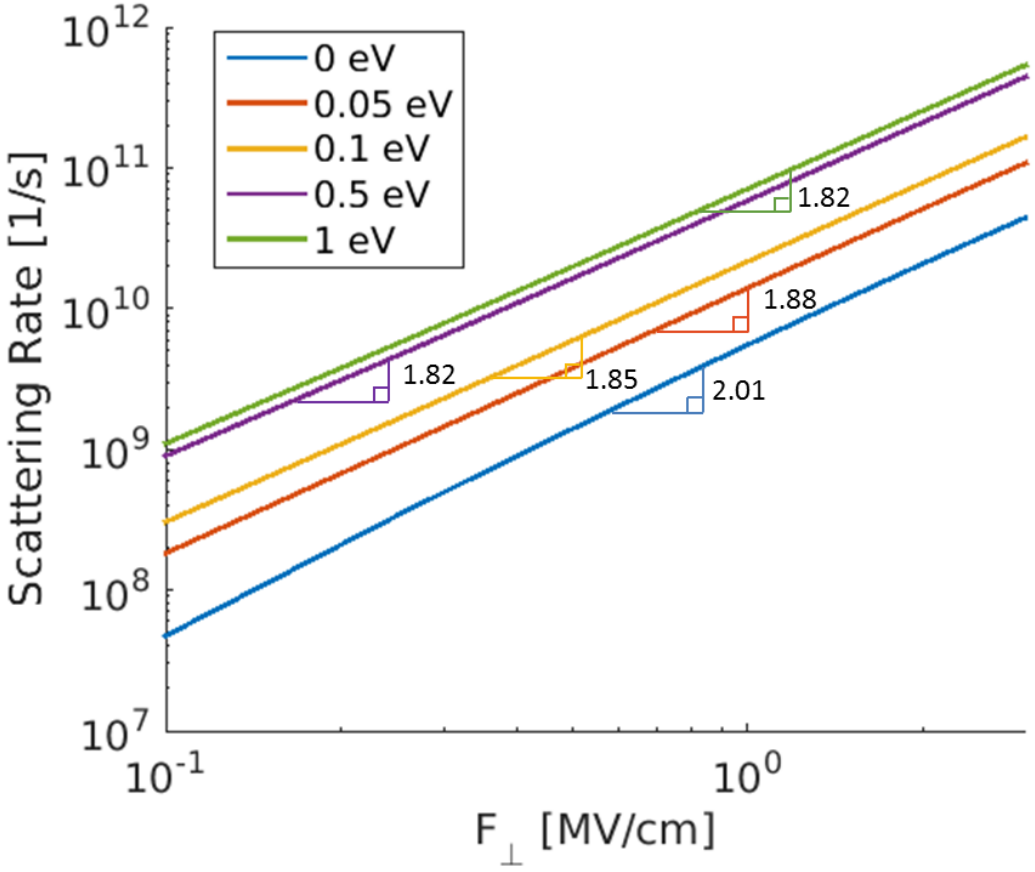

Figure 3.11: Field-dependent scattering within the 1^{st} subband for electrons with various kinetic energies.

Chapter 4: Incomplete Ionization in p-Type SiC

4.1 Background and Introduction

This work is motivated in part to further the understanding of p-type SiC devices, and ultimately to aid in the development of SiC CMOS devices. Presently, more attention is being paid to making advances in n-type SiC devices. In this work, I sought to investigate issues related to p-type SiC. In particular, I analyze the degree of incomplete ionization which becomes an important effect at higher doping concentrations that exist in p-type and CMOS devices. My major contributions in this area include aggregating and analyzing almost all existing published resistivity, Hall mobility, and ionization energy data on Al-doped 4H-SiC, and using this information to verify my physics-based formulation of the incomplete ionization. I also extend this incomplete ionization fraction calculation to higher temperatures and developed an easy-to-use parameterization of the temperature and concentration-dependent ionization fraction by using a genetic algorithm. As a small aside, I have also used the genetic algorithm to optimally parameterize the experimental Hall mobility data over a larger range of temperatures and doping concentrations and using more data than those that are currently published.

Dopant atoms are used in semiconductor devices to add mobile electrons (using donors) and mobile holes (using acceptors) which act as charge carriers. To simplify

device simulations/calculations, the assumption is sometimes made that all dopant atoms are ionized. As a consequence, this assumption implies that all acceptors have captured an electron from the valence band ($N_A = N_A^-$) and all donors have donated an electron to the conduction band ($N_D = N_D^+$) and as such, each dopant atom contributes one charge carrier (barring electron-hole recombination effects and assuming this is an uncompensated semiconductor). In a real physical system, the energy needed to ionize these dopant atoms mainly comes from thermal energy which follows a Maxwell-Boltzmann distribution under no applied field. Based off this distribution, some portion of the dopant atoms will inevitably remain unionized due to the non-zero probability of electrons having energy less than the ionization energy. The degree of incomplete ionization depends on not only the temperature, but also on the ionization energy of the state, and the conduction/valence band density of states for donors/acceptors respectively.

For the case of p-type 4H-SiC, unfortunately, all acceptor dopant species have large ionization energies. As a result of this fact, a greater degree of incomplete ionization is expected in p-type SiC than in its n-type counterpart or in other materials like Si and Ge [60]. Consequently, this effect must be treated more carefully in SiC in order to accurately model mobile hole densities for given doping and temperature conditions.

Of the acceptor dopants, aluminum (Al) is arguably the most favorable as it has the highest solid solubility [10, 61–66] and lowest ionization energy at around $190 - 230$meV [10, 65–72]. The other two main acceptor dopants are Ga which has an ionization energy of approximately $250 - 270$meV and B with two levels -

one around 300meV from Si lattice site occupation and one around 650meV due to defect-related complex known as the D-center [10, 65–70, 73–79]. SiC doping levels are illustrated in Figure 4.1.

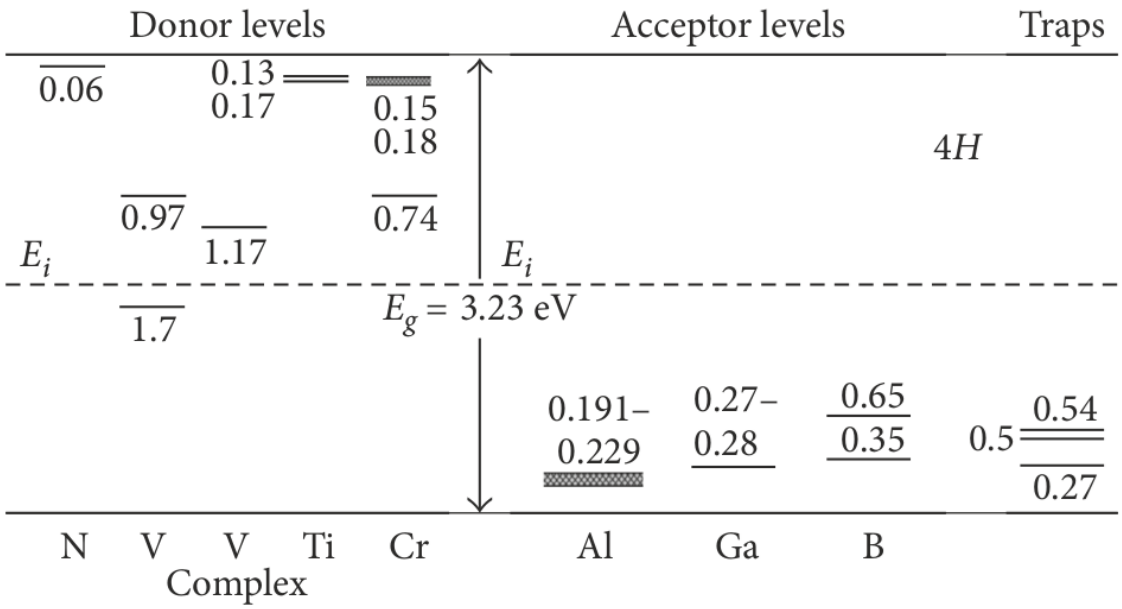

Figure 4.1: Doping levels in 4H-SiC.

For comparison, the most common n-type dopants in SiC also introduce two levels each: $40-70$meV and $90-130$meV for nitrogen (N) as well as $40-50$meV and $80-100$meV for phosphorous (P) [68, 71, 72, 79–88]. P-type dopants in Ge have an ionization energy of merely 10meV and for Si $45-73$meV [10, 68, 89–91]. Various dopant levels in Ge, Si, and GaAs are shown in Figure 4.2.

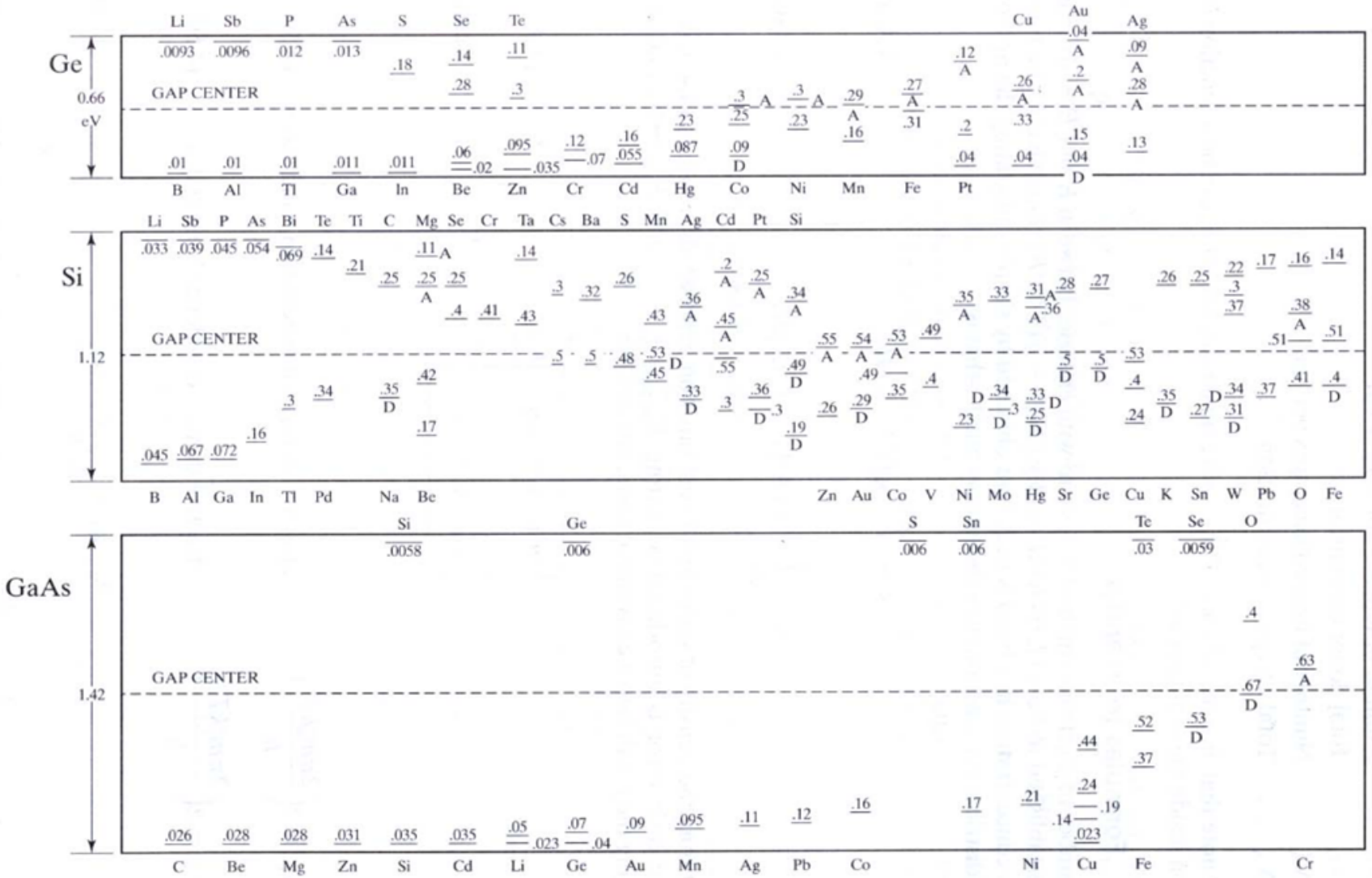

Figure 4.2: Doping levels in Ge, Si, and GaAs.

4.2 Standard Incomplete Ionization Formulation

In materials like Si, where incomplete ionization is often neglected, if it is included, it is generally done so in an approximate manner to ease computational complexity. The standard approximations made usually include using a single discrete impurity energy level (generally also treated to be independent of the doping concentration) and applying Maxwell-Boltzmann quantum-state occupation statistics in lieu of the true Fermi-Dirac statistics for fermions. These approximations become worse for higher doping concentrations when the dopant wavefunctions start to overlap and the semiconductor approaches degeneracy.

Under these assumptions we can calculate the ratio of mobile holes to acceptor atoms p/N_A by invoking the charge neutrality condition and manipulating the resulting equation to remove the dependence on the Fermi level (an unknown quantity) and obtain an algebraic expression.

To begin, we will first make assumptions about the physical system which result in a single impurity level. This means we treat the dopant atoms as far apart and non-interacting i.e. no wavefunction overlap. This assumption is better for low-doped samples because the average distance between nearest-neighbor dopant atoms goes as $N_A^{(-1/3)}$. The discrete dopant energy levels form an acceptor density of states in the bandgap, which, at sufficiently low doping concentrations, takes the approximate form of a delta-function at the dopant energy level E_A.

$$\rho_i(E) = N_A \delta(E - E_A) \tag{4.1}$$

This density of states must integrate to the total acceptor density N_A because there are N_A atoms and thus N_A total discrete energy states. We will see later that this acceptor density of states function spreads out and becomes more complex when more physical and quantum-mechanical effects are accounted for.

Now we can compute the total number of ionized acceptors by multiplying the acceptor density of states by the occupancy probability function, then integrating over all energies. For the occupancy of acceptor states, we use a modified Fermi-Dirac function which includes the degeneracy $g_A = 4$ of acceptor state occupancy. The four-fold degeneracy comes from the choice of spin-up or spin-down electron occupying the acceptor state, as well as the choice to create a heavy or light hole in the valence band due to the degeneracy at the valence band maximum (Γ-point) in 4H-SiC. This is described in further detail in section B.2.

$$N_A^- = \int_{-\infty}^{\infty} \rho_i(E) f_A(E) dE \tag{4.2}$$

$$f_A(E) = \frac{1}{1 + g_A \exp\left(\frac{E - E_F}{k_B T}\right)} \tag{4.3}$$

Carrying out the integration:

$$N_A^- = \int_{-\infty}^{\infty} \frac{N_A \delta(E - E_A)}{1 + g_A \exp\left(\frac{E - E_F}{k_B T}\right)} dE \tag{4.4}$$

$$N_A^- = \frac{N_A}{1 + g_A \exp\left(\frac{E_A - E_F}{k_B T}\right)} \tag{4.5}$$

The analogous calculation is also performed to calculate the number of holes in the valence band, except we use the valence band density of states $\rho_v(E)$ defined for $-\infty \leq E \leq E_V$. The $1 - f(E)$ term comes from the fact that holes stem from

unoccupied valence band states rather than filled states.

$$\rho_v(E) = \frac{4\pi(2m_p^*)^{3/2}}{h^3}\sqrt{E_V - E} \tag{4.6}$$

$$f(E) = \frac{1}{1 + \exp\left(\frac{E-E_F}{k_BT}\right)} \tag{4.7}$$

$$p = \int_{-\infty}^{E_V} \rho_v(E)(1 - f(E))dE \tag{4.8}$$

$$p = \frac{4\pi(2m_p^*)^{3/2}}{h^3}\int_{-\infty}^{E_V} \frac{\sqrt{E_V - E}}{1 + \exp\left(\frac{E_F-E}{k_BT}\right)}dE \tag{4.9}$$

In this standard formulation, we approximate the Fermi-Dirac occupancy distribution $f(E)$ with the Maxwell-Boltzmann which is a valid when $E_F - E_V \gtrsim 3k_BT$ i.e. non-degenerate doping scenarios when the Fermi level is at least a few k_BT away from the valence band edge. This will allow us to obtain a closed-form solution to an otherwise non-analytic expression.

$$1 - f(E) = \frac{1}{1 + \exp\left(\frac{E_F-E}{k_BT}\right)} \approx \exp\left(\frac{E - E_F}{k_BT}\right) \tag{4.10}$$

$$p \approx \frac{4\pi(2m_p^*)^{3/2}}{h^3}\int_{-\infty}^{E_V} \sqrt{E_V - E}\exp\left(\frac{E - E_F}{k_BT}\right)dE \tag{4.11}$$

Equation 4.11 has an exact solution which can be written using N_V, the effective density of states in the valence band which depends on the hole effective mass in the valence band m_p^*:

$$p \approx N_V \exp\left(\frac{E_V - E_F}{k_BT}\right) \tag{4.12}$$

$$N_V = 2\left(\frac{2\pi m_p^* k_BT}{h^2}\right)^{(3/2)} \tag{4.13}$$

Now we must apply the charge-neutrality condition. For our system, we assume no donor counter doping, and since intrinsic carrier concentration n_i is so small

in 4H-SiC, we can also neglect the equilibrium electron concentration.

$$p + N_D^+ = n + N_A^- \tag{4.14}$$

$$p = \frac{n_i^2}{p} + N_A^- \tag{4.15}$$

$$p \approx N_A^- \tag{4.16}$$

The resulting charge neutrality equation states that the hole concentration must equal the ionized acceptor concentration. This result stands to reason as the majority of holes are created by promoting electrons from the valence band to the acceptor states rather than to the conduction band due to the much larger energy difference. In general, both of these terms are functions of the unknown Fermi-level E_F, as exhibited in Equations 4.5 and 4.12. By making the Maxwell-Boltzmann occupation statistics approximation (low doping limit), however, the governing equations can be manipulated to explicitly remove the E_F dependence and provide a closed-form solution of only known quantities. We can rewrite Equation 4.5 in terms of the hole concentration given in Equation 4.12, and apply the charge neutrality condition in Equation 4.16 leaving us with a quadratic equation for the solution of the hole concentration p.

$$N_A^- = \frac{N_A}{1 + g_A \exp\left(\frac{E_V - E_F}{k_B T}\right) \exp\left(\frac{E_A - E_V}{k_B T}\right)} \tag{4.17}$$

$$N_A^- = p = \frac{N_A}{1 + \frac{g_A p}{N_V} \exp\left(\frac{E_A - E_V}{k_B T}\right)} \tag{4.18}$$

$$p = \frac{N_A}{1 + \frac{p}{2\gamma}} \tag{4.19}$$

Finally solving the quadratic and introducing the auxiliary variable of known quantities γ:

$$p = -\gamma + \sqrt{\gamma^2 + 2\gamma N_A} \tag{4.20}$$

$$\gamma = \frac{N_V}{2g_A} \exp\left(-\frac{\Delta E_A}{k_B T}\right) \tag{4.21}$$

$$\Delta E_A = E_A - E_V \tag{4.22}$$

As a reminder, N_A is the acceptor doping density, N_V is the valence band effective density of states, ΔE_A is the acceptor ionization energy, and g_A is the acceptor state degeneracy equal to 4 in 4H-SiC.

For other materials where n_i is not small (or for very high temperatures), one must solve a cubic equation to calculate the hole concentration:

$$p^3 + 2\gamma p^2 - (2\gamma N_A + n_i^2)p - 2\gamma n_i^2 = 0 \tag{4.23}$$

For those curious, this has the closed form solution:

$$p = \frac{1}{3\sqrt[3]{2}}\left[\sqrt{4x^3 + y^2} + y\right]^{(1/3)} - \frac{\sqrt[3]{2}}{3}\frac{x}{\left[\sqrt{4x^3 + y^2} + y\right]^{(1/3)}} - \frac{2\gamma}{3} \tag{4.24}$$

$$x = -6N_A\gamma - 4\gamma^2 - 3n_i^2 \tag{4.25}$$

$$y = -36N_A\gamma^2 - 16\gamma^3 + 36\gamma n_i^2 \tag{4.26}$$

A comparison of the quadratic solutions (dashed) to the full cubic solutions (solid) are shown in Figure 4.3. The more accurate cubic solutions have three characteristic regions. For the lowest temperatures, we see the freeze-out region where incomplete ionization occurs due to the lack of thermal energy needed to ionize all of the acceptor atoms and create mobile holes. In the middle temperature region, the mobile

hole concentration equals the total acceptor doping and remains fairly constant. This region of stability extends over a larger temperature range for higher acceptor doping. This is the region where devices should normally aim to operate within. Finally, at extremely high temperatures, the intrinsic carrier concentration starts to dominate and the material is said to be intrinsic because the hole concentration equals the intrinsic carrier concentration independent of the doping.

Plotted in a different manner, Figure 4.4 shows the plot of p/N_A which shows incomplete ionization as a fraction. From this plot we can also determine as general trend that incomplete ionization occurs more severely for higher doping concentrations. This can be a problem for MOS-type devices which often have body/channel doping in the range 10^{16}cm^{-3} to 10^{18}cm^{-3} where the conductivity of that region could be significantly less than predicted assuming complete ionization.

For degenerate doping, some issues arise that this simplified model can not handle. Most importantly, the Maxwell-Boltzmann statistics will overpredict occupancy of valence band states because it allows more than one electron to occupy a single spin-state which is forbidden for Fermions. To solve this problem we need to use the full Fermi-Dirac distribution in the hole concentration calculation. Additionally, as doping increases, so too does the number of mobile holes in the valence band. These holes, however, are not uniformly distributed throughout the crystal. Instead, they will arrange themselves preferentially around acceptor ions via Coulombic attraction, leading to an increasing amount of screening of the acceptor atom's potential [92]. This, in turn, leads to a lower ionization energy because the

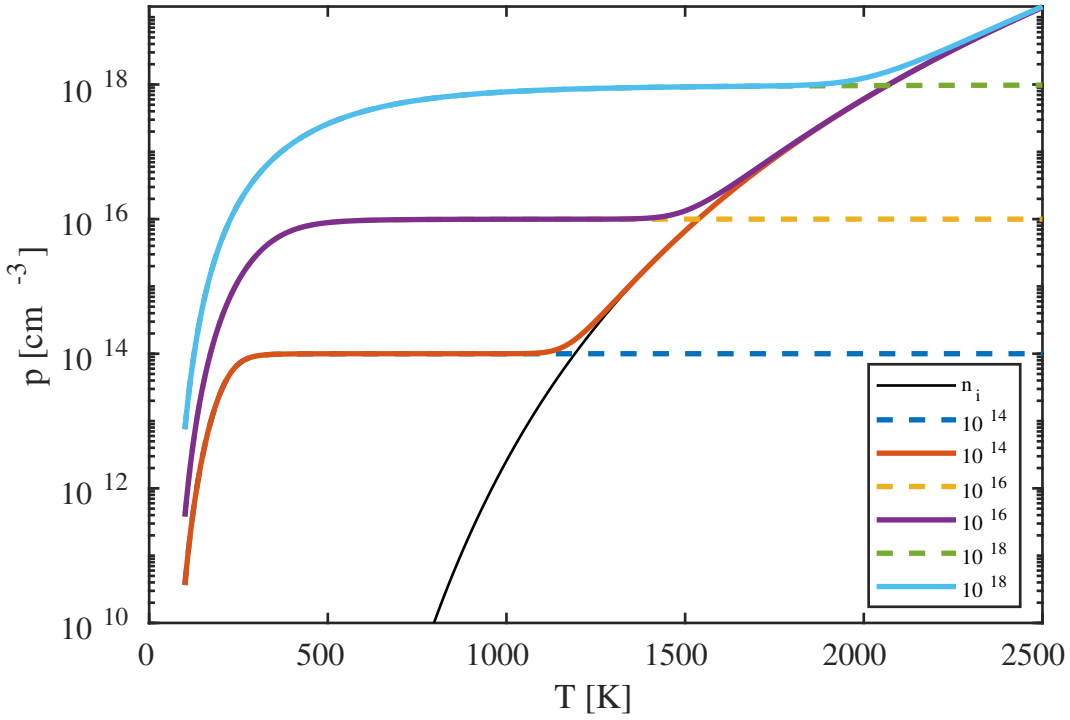

Figure 4.3: Hole concentration calculated using the standard incomplete ionization model for various N_A doping. Dashed lines show the quadratic solution which ignores n_i and the solid lines show the cubic solution which includes it. Calculated for 4H-SiC with $\Delta E_A = 200$meV.

average depth of the potential well decreases, as shown in Figure 4.5. This doping concentration dependent ionization energy can also be included into the simplified incomplete ionization model.

Increasing doping concentration also leads to interactions among dopant atoms because the average distance between atoms shrinks as $N_A^{-1/3}$. Once these atoms become close enough such that their valence state wavefunctions overlap, the degeneracy of their individual ionization energies must be lifted - leading to a quantum-mechanical broadening of the acceptor density of states. This effect combined with the lowering of the average ionization energy due to screening can lead to overlap

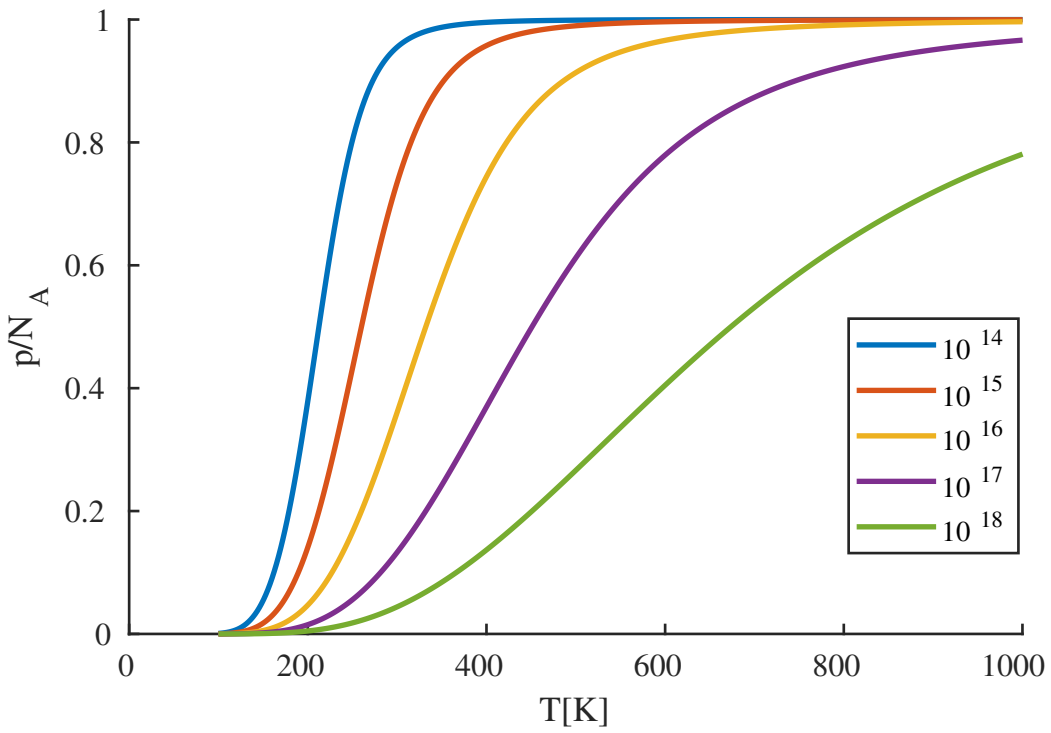

Figure 4.4: p/N_A calculated for different doping concentrations as a function of temperature for 4H-SiC with $\Delta E_A = 200$meV.

of the acceptor states with the valence band. Lastly, the as the doping concentration increases the material as a whole becomes more disordered. These randomly distributed dopants will randomly form clusters leaving local regions of greater-than-average density of acceptors and other regions of less-than-average density. The Coulombic charge created by these ionized atoms causes a shift in the local potential which will change with position about its equilibrium mean value. This locally fluctuating potential which changes on a mesoscopic scale causes the local band structure to shift above and below its equilibrium state. Because the density of states is a value averaged over the entire volume of the crystal, this effect leads to a smearing of the states. Finally, at high enough doping concentration, the acceptor

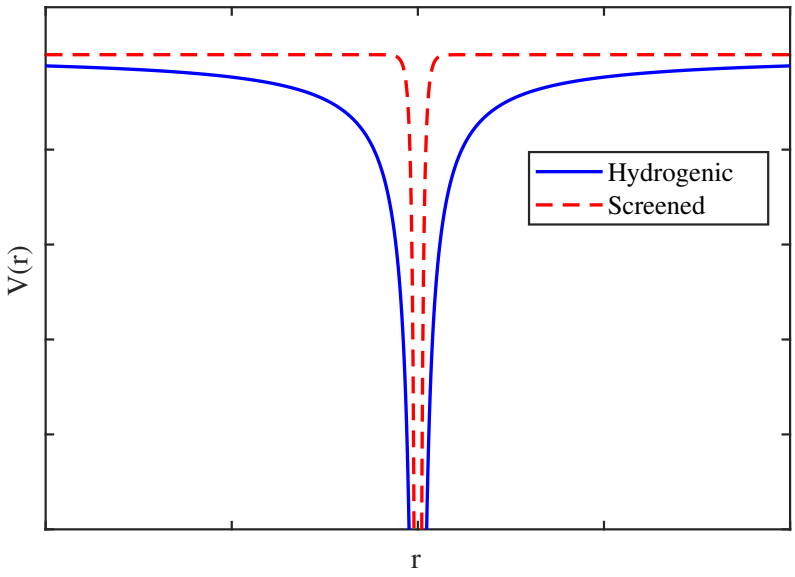

Figure 4.5: Coulombic potential of impurity atom core. the solid line is the bare hydrogenic $1/r$ potential and the dashed line is the screened potential under the effects of mobile carriers redistributing themselves.

density of states can evolve into a quasi-continuous band which supports a conduction mechanism parallel to valence band transport. This type of conduction is often referred to as impurity conduction and includes various mechanisms: Mott conduction, Anderson conduction, nearest neighbor hopping, and variable range hopping. These effects will be included in our advanced theoretical model of incomplete ionization in p-type 4H-SiC.

It is also possible for dopants to substitute inequivalent lattice sites which have different ionization energies due to the different forms of the local lattice potential. In 4H-SiC, Al preferentially substitutes Si atoms in the lattice but there are two inequivalent Si atom sites which are denoted as the hexagonal h and the cubic k site. For visualization of this effect, refer to Figure 4.6. We know that all SiC lattices are formed by combining arrangements of tetrahedrally bonded Si and C atoms. Each Si is bonded to 4 C atoms and vice-versa. For 4H-SiC when two tetrahedra are joined in an interpenetrating manner (vertex to center), there are two arrangements which occur. The hexagonal site is formed when the configuration makes a more mirror-symmetric structure where the external atoms lie on the vertices of triangular prism. The cubic site is formed when one tetrahedra is rotated 60°about the connection axis leaving the external atoms to lie on the vertices of a triangular antiprism. The number and type of inequivalent lattice sites present in a SiC crystal depends on its polytype. For 3C-SiC, every site is a cubic site and in 6H-SiC, there is one hexagonal site and two different cubic sites as shown in Figure 4.7.

To include the effects of different dopant site ionization energies, the total

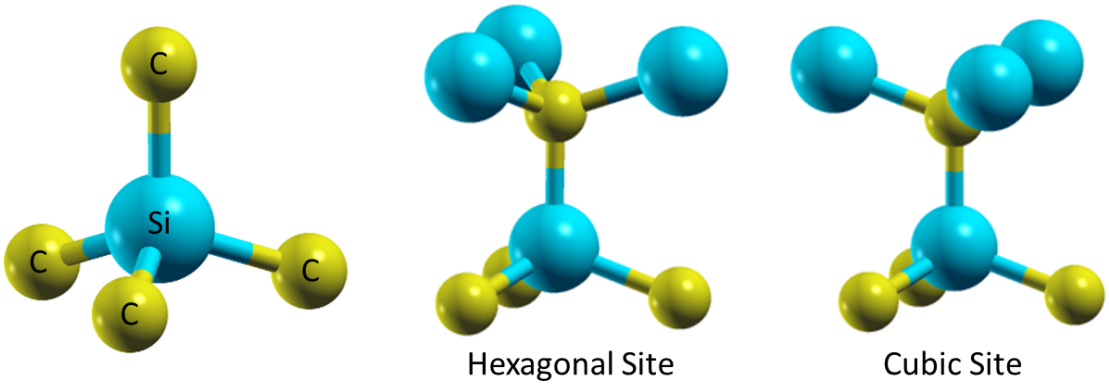

Figure 4.6: Local arrangement of atoms leading to inequivalent lattice sites in 4H-SiC.

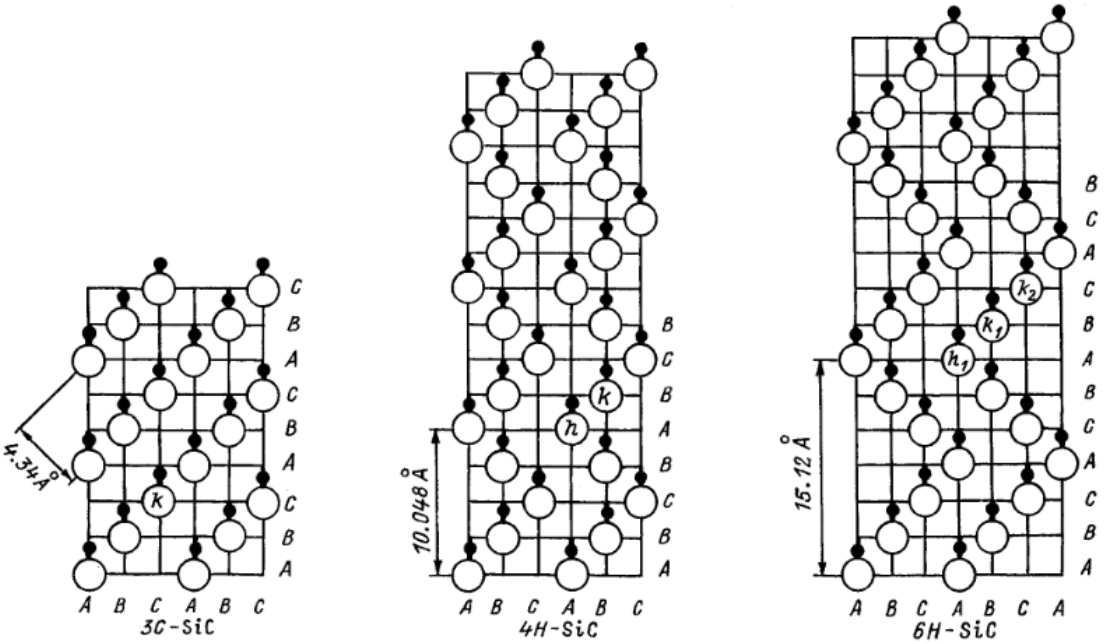

Figure 4.7: Inequivalent sites (h=hexagonal, k=cubic) labeled in SiC polytypes. The black circles represent carbon atoms and the white circles represent Si atoms.

ionized dopant concentration is split into a sum. The fraction of atoms in each doping site is denoted with f_h and f_k and are usually taken to be $\frac{1}{2}$. Equation 4.27

also leads to a cubic solution for the hole concentration.

$$N_A^- = \frac{f_h N_A}{1 + g_A \exp\left(\frac{E_{Ah} - E_F}{k_B T}\right)} + \frac{f_k N_A}{1 + g_A \exp\left(\frac{E_{Ak} - E_F}{k_B T}\right)} \tag{4.27}$$

$$p = \frac{f_h N_A}{1 + \frac{p}{2\gamma_h}} + \frac{f_k N_A}{1 + \frac{p}{2\gamma_k}} \tag{4.28}$$

$$\gamma_x = \frac{N_V}{2g_A} \exp\left(-\frac{\Delta E_{Ax}}{k_B T}\right) \tag{4.29}$$

$$f_k = 1 - f_h \tag{4.30}$$

$$p = \frac{1}{3\sqrt[3]{2}} \left[\sqrt{4x^3 + y^2} + y\right]^{(1/3)} - \frac{\sqrt[3]{2}}{3} \frac{x}{\left[\sqrt{4x^3 + y^2} + y\right]^{(1/3)}} - \frac{2(\gamma_h + \gamma_k)}{3} \tag{4.31}$$

$$x = 6(f_h N_A(\gamma_k - \gamma_h) - N_A\gamma_k + 2\gamma_h\gamma_k) - 4(\gamma_h + \gamma_k)^2 \tag{4.32}$$

$$y = 36(f_h N_A(\gamma_k^2 - \gamma_h^2) - N_A\gamma_k^2) + 72 N_A\gamma_h\gamma_k + 24(\gamma_h^2\gamma_k + \gamma_h\gamma_k^2) - 16(\gamma_h^3 + \gamma_k^3) \tag{4.33}$$

For materials where there are more than two inequivalent lattice sites, equation 4.27 can be easily extended by adding additional terms for each inequivalent site leading to increasing polynomial degree solutions. For polynomial degree greater than 3, a numerical solution must be obtained to solve for the acceptor concentration and care must be taken to ensure that the 'positive' physical solution between 0 and N_A is the one obtained. This is applicable in n-type 6H-SiC where nitrogen incorporates into three different sites: one hexagonal site and two inequivalent cubic sites where $f_h = f_{k1} = f_{k2} = \frac{1}{3}$ leading to a quartic equation for p.

This modification can also be used to model systems where multiple acceptor dopant species are present such as p-type 4H-SiC doped with a deep B well and a shallow Al adjustment at the surface. The ionization energy difference between Al and B is quite large ($> 100meV$) so the solution to the cubic equation may differ

significantly from the solution of either dopant species individually depending on the ratio of their concentrations. For the situation of different doping species, the fraction f must be solved for by using the individual doping concentrations N_{Al} and N_B: $f_{Al} = N_{Al}/(N_{Al} + N_B)$ and $f_B = 1 - f_{Al}$.

4.3 Doping-Dependent Ionization Energy

For a more accurate calculation of incomplete ionization, one must include the effects of doping-dependent ionization energy which lowers the energy required to ionize the dopant atoms as the doping concentration increases. This effect turns out to significantly affect the resulting p/N_A ratio for high doping, and in particular semiconductors like SiC where the low-doped ionization energy is quite high.

The doping-dependent ionization energy can be experimentally measured through various techniques including CV, thermal admittance spectroscopy, Hall and 4-point resistivity fits, donor-acceptor pair luminescence, free-carrier concentration spectroscopy, Raman spectroscopy, deep-level transient spectroscopy, IR absorption, etc. The experimental data from the literature confirms that increasing doping concentration lowers the ionization energy, by moving the acceptor density of states towards the valence band. This effect is caused by the increased screening from mobile holes in the valence band which distribute themselves such that the Coulombic energy of the system is decreased, resulting in a lower acceptor ionization energy [92]. The same effect is explained for the case of mobile electrons screening donor states in Si in other works [92–95].

To develop an empirical model of the doping-dependent ionization energy in Al-doped 4H-SiC, a comprehensive review of experimentally measured ionization energies was first performed. The experimentally determined energies from the literature are presented in Figure 4.8. The spread in the ionization energies at any given doping concentration may be partially explained by the varied techniques used to extract the energies. Some techniques may be capturing different parts of the acceptor density of states which may not necessarily be a single discrete energy level. Other contributing factors to these discrepancies might include different fabrication techniques and differing degrees of counter-doping among the various research groups. For this work, the ionization energy is considered to be the mean (center) of the acceptor density of states. The empirical model of the ionization energy is extracted from the experimental data by minimizing the least-squares error.

A well-behaved logistical equation is used to parameterize the doping-dependent ionization energy (Equation 4.34) [96–98] and the experimental data is used to determine the optimal parameters. This model contains three parameters, ΔE_{A0} as the isolated dopant ionization energy, N_E as the reference doping where the ionization energy is half of its isolated value, and a characterizing the degree of the doping dependence. The ionization energy based on this model is shown in black in Figure 4.8. *This is the parameterized form of $\Delta E_A(N_A)$ that is used in the rest of this work.*

$$\Delta E_A(N_A) = \frac{\Delta E_{A0}}{1 + \left(\frac{N_A}{N_E}\right)^a} \tag{4.34}$$

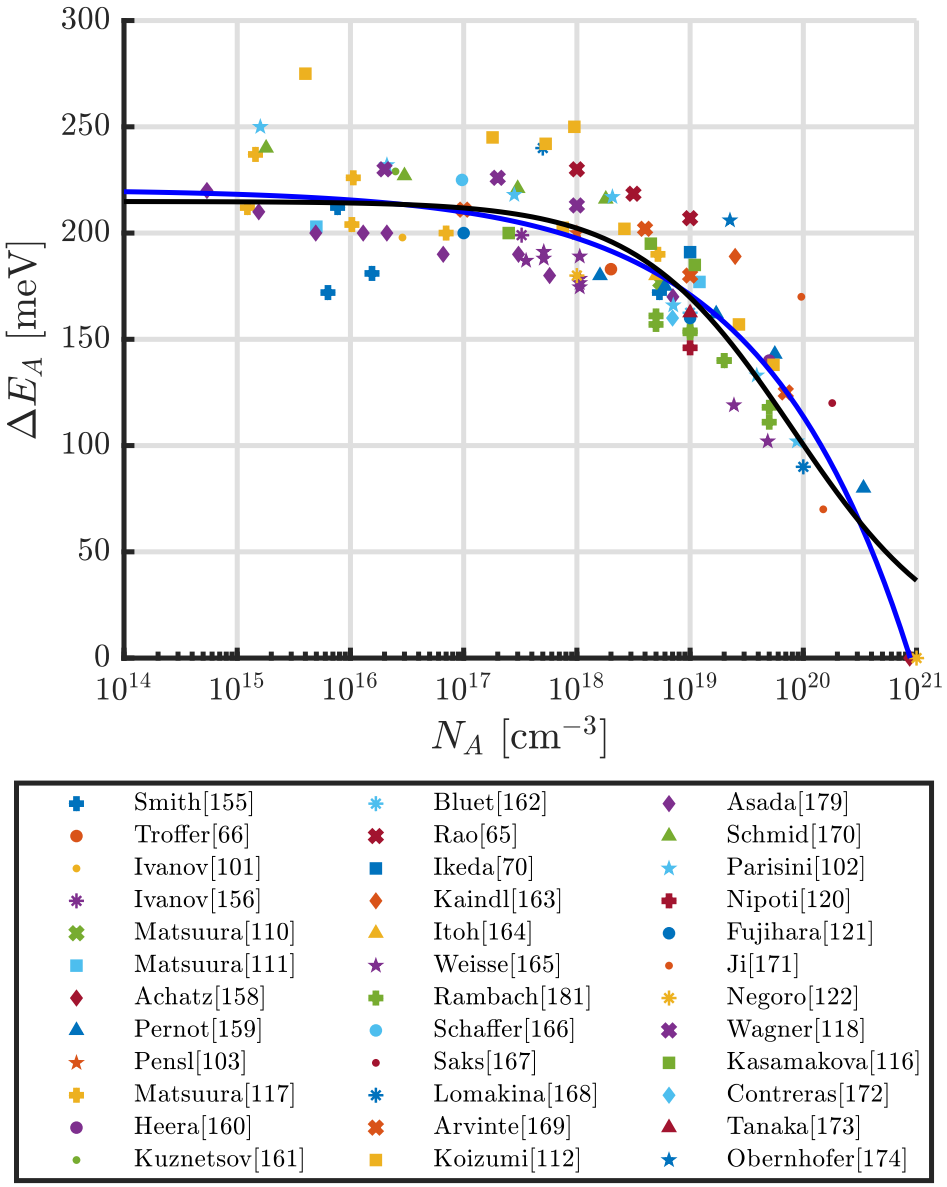

Figure 4.8: Doping density-dependent fit to experimental acceptor ionization energy for 4H-SiC doped with Al. The blue line is the Pearson-Bardeen model and the black line is the logistical parameterization.

In earlier literature works, ionization energies may also be fit using the Pearson-Bardeen model which takes the form $\Delta E_A(N_A) = \Delta E_{A0} - \alpha(N_A)^{1/3}$ instead of the form in Equation 4.34. The Pearson-Bardeen model is based on the average impurity separation distance ($N^{1/3}$). The Pearson-Bardeen formula is not used in my incomplete ionization model because at high enough doping, it predicts that the ionization energy eventually becomes negative and continues past the valence band edge. Instead, the logistical expression in Equation 4.34 is used so that the center of the impurity band asymptotically approaches the valence band edge. This property gives better control of how the high-doped regions behave so that they can be tuned with other parameters of the incomplete ionization model in accordance to the experimental data. The logistical formula may also be potentially more physically sound because the change in ionization energy is mainly due to screening and thus should tend towards zero [92]. Figure 4.8 shows the logistical parameterization in black and the fit using the Pearson-Bardeen parameterization is in blue. Both models agree well for doping concentrations less than $3 \times 10^{20}\text{cm}^{-3}$. Later discussion will address doping concentrations at and above this level, where a different mechanism dominates the p/N_A fraction such that the exact ionization energy in this region is not as important.

4.4 Acceptor Density of States

As mentioned earlier, the acceptor density of states is not always best described by a single energy level, but instead by a density of states function which

is spread in energy space. This is particularly true in the case of higher doping when the interactions between dopant atoms become significant. When the doping concentration is increased, the number of dopants in close proximity to each other also increases, causing greater quantum-mechanical interaction. The overlap of the dopant-state wavefunctions along with the Pauli-Exclusion principle lifts the degeneracy of the single dopant energy levels and broadens them from series of localized δ-function states (all of equal energy) into a quasi-continuous doping band [93, 99]. The width of this band is calculated by adapting work from Lee et al. which was performed on donor states [100].

In this work, the acceptor density of states spread by wavefunction overlap $\rho_{i0}(E)$ is taken as a single rectangle function centered at $E_A(N_A)$ which integrates to the total acceptor density N_A (with respect to the energy variable E). A single impurity band is used in this model because the vast majority of experimental evidence reports no significant ionization energy variation (to within analysis resolution of a few meV) amongst Al substitution of inequivalent silicon lattice sites (hexagonal and cubic) in 4H-SiC [65, 69, 70, 85, 101–103]. The energy bandwidth (width of the rectangle function) of the donor states is characterized by the parameter B which is calculated using the tight binding model, hydrogenic s-orbitals, and assuming that the dopants are randomly distributed. Based on the work of Lee et al. [100], we implement the following set of equations for $\rho_{i0}(E)$ and B for acceptors in SiC.

$$\rho_{i0}(E) = \begin{cases} N_A/B, & -\frac{B}{2} \leq E - E_A(N_A) \leq \frac{B}{2} \\ 0, & \text{otherwise} \end{cases} \tag{4.35}$$

$$B = 2\int_0^\infty J(R) 4\pi N_A R^2 \exp\left(-\frac{4}{3}\pi N_A R^3\right) dR \tag{4.36}$$

$$J(R) = \frac{q^2\xi}{4\pi\epsilon_r\epsilon_0}(1+\xi R)\exp(-\xi R) \tag{4.37}$$

Under the tight binding approximation, the dopant band width B is related to the energy transfer integral $J(R)$ between nearest neighbor dopant states a distance R apart. $J(R)$ is calculated by using hydrogenic s-orbitals to evaluate the energy transfer integral. In this calculation, $\xi = (1/a_0)(E_A/E_0)^{1/2}$ is the scaled inverse radius for the acceptor state, a_0 is the Bohr radius, and E_0 is the ground state energy of the hydrogen atom [91]. By assuming the dopants are uniformly randomly distributed, the nearest neighbor distance R will follow a Poisson distribution [104]. The bandwidth B is then calculated by finding twice the average value of $J(R)$ and the band is centered symmetrically about E_A [99].

4.5 Disorder Effects and Band Tailing

In addition to the impurity density of states spreading due to wavefunction overlap, the band is further spread due to the effects of lattice disorder and subsequent potential fluctuations arising from the randomly distributed ionized dopants. At any given point in a doped crystal, the potential will differ from that of a pure crystal due to the Coulomb potential produced the dopant ions. Random fluctuations within the local concentration of the dopant atoms causes a potential fluc-

tuation about its mean value on a mesoscopic scale. A less significant potential deviation is also created by the local strain induced by the dopant ions and clusters changing the periodic crystal structure, but we will be neglecting this smaller effect in this work. Depending on the local atomic configuration of the dopant ions, the potential throughout the crystal and thus the energy reference for the quantum states will fluctuate about its mean value. [93, 94, 100, 104, 105].

These potential fluctuations lead to a distortion or smearing of the states near the conduction and valence band extrema as the energy reference of these states varies locally but the macroscopic density of states formulae represent spatial averages over the entire lattice. If the potential varies slowly with respect to the dopant wavefunction, the local impurity states are also shifted with respect to this energy - leading to impurity band tailing [92, 94, 100, 105, 106]. This effect is incorporated by separately averaging the standard valence band density of states formula and the rectangular acceptor density of states over the local potential energy distribution inside the crystal (denoted as $P(V)$) [92–94, 100, 104, 105]. The averaging is accomplished by means of convolution integrals, given in Equations 4.43 through 4.46.

$$P(V) = \frac{1}{(2\pi)^{1/2}\sigma} \exp\left(-\frac{V^2}{2\sigma^2}\right) \tag{4.38}$$

$$\sigma = \left(\frac{N_A^-}{8\pi^2\epsilon_r^2\epsilon_0^2} q^4 \lambda\right)^{1/2} \tag{4.39}$$

$$\lambda^{-2} = \lambda_h^{-2} + \lambda_i^{-2} \tag{4.40}$$

$$\lambda_h = \left(\frac{\epsilon_r\epsilon_0 k_B T}{q^2 p}\right)^{1/2} \tag{4.41}$$

$$\lambda_i = \left(\frac{\epsilon_r\epsilon_0 k_B T}{q^2 p(1 + p/N_A)}\right)^{1/2} + \Gamma\left(\frac{4}{3}\right)\left[\frac{4}{3}\pi N_A\right]^{-1/3} \tag{4.42}$$

The standard deviation of the Gaussian potential distribution is characterized by the screening length λ. The screening length is itself comprised of hole and ionic components. The hole screening length comes from the standard Debye length in a semiconductor. The ionized impurity screening length also comes from the Debye length but is increased by the average distance between acceptor atoms.

With this modification, the density of impurity and valence band density of states become $\rho_i(E)$ and $\rho_v(E)$ respectively. The resulting density of states looks a slightly smeared version of the input - causing tail states to appear at the band edges, as shown in Figure 4.9. The variation of the local potential corresponds to the local occupancy of the acceptor states causing regions of higher-than-average acceptor occupancy (local negative charge) and lower-than-average acceptor occupancy (local positive charge) due to the spatially-independent Fermi energy. Because the local potential energy of the system affects the local shift in the conduction and valence bands in the same manner, the local band gap E_g remains unchanged [94].

$$\rho_i(E) = \int_{-\infty}^{+\infty} \rho_{i0}(E - V)P(V)dV \tag{4.43}$$

$$\rho_v(E) = \int_{-\infty}^{E-E_V} \rho_{v0}(E - V)P(V)dV \tag{4.44}$$

$$\rho_{i0}(E) = \begin{cases} N_A/B, & -\frac{B}{2} \leq E - E_A(N_A) \leq \frac{B}{2} \\ 0, & \text{otherwise} \end{cases} \tag{4.45}$$

$$\rho_{v0}(E) = \frac{4\pi(2m_p^*)^{3/2}}{h^3}\sqrt{E_V - E} \tag{4.46}$$

With these resulting dopant density of states $\rho_i(E)$ and valence band density of states $\rho_v(E)$, the only remaining unknown in my model is the Fermi level E_F which can be solved for numerically and then used to compute the ratio p/N_A.

The full visualization of the density of states under various circumstances or levels of approximation is depicted in Figure 4.10. For the acceptor density of states, in the case of low doped samples there will be a single energy level at energy E_A which will spread out due to wavefunction overlap as the doping density increases. Both the acceptor and valence band density of state functions then smear out when disorder effects begin to appear due to randomly arranged dopant clusters and lattice disorder at even higher doping concentrations.

4.6 Theoretical Incomplete Ionization Model

The theoretical incomplete ionization model described in this work is derived from physical principles and includes the effects discussed in the previous sections: doping-dependent ionization energy, dopant band spreading due to wavefunction

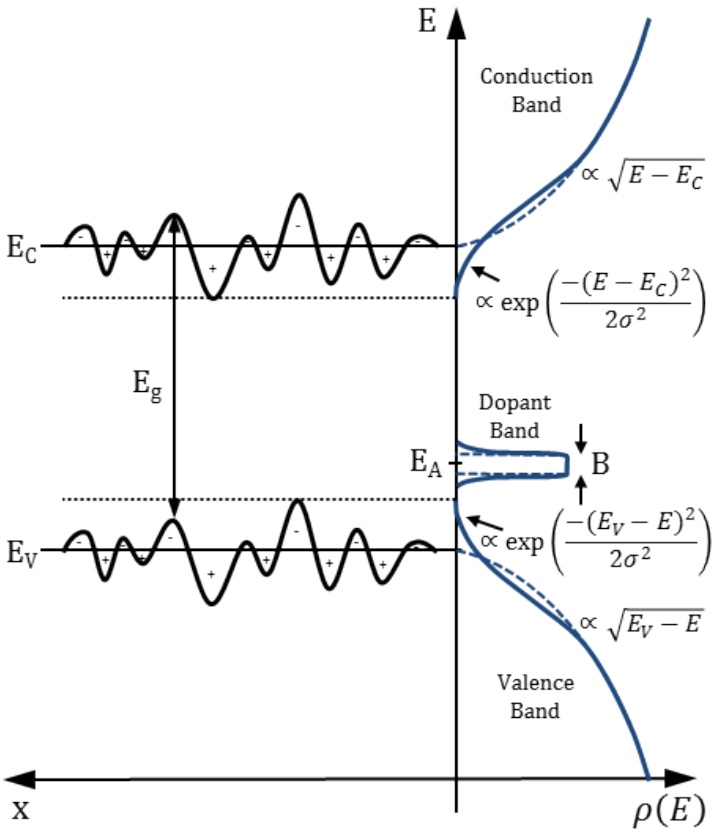

Figure 4.9: P-doped semiconductor density of states diagram. Left: Shows the position-dependent variation of the local band structure (negative of potential). Right: Dashed blue lines show the standard valence band density of states and the rectangular acceptor band density of states. After the inclusion of disorder effects, the resulting density of states with band tailing is shown with solid blue lines. Note: Image is not to scale - depending on the doping concentration, the doping band will be significantly closer to and may even overlap the valence band density of states tail. The doping band width B as well as its height will also vary considerably depending on the doping density.

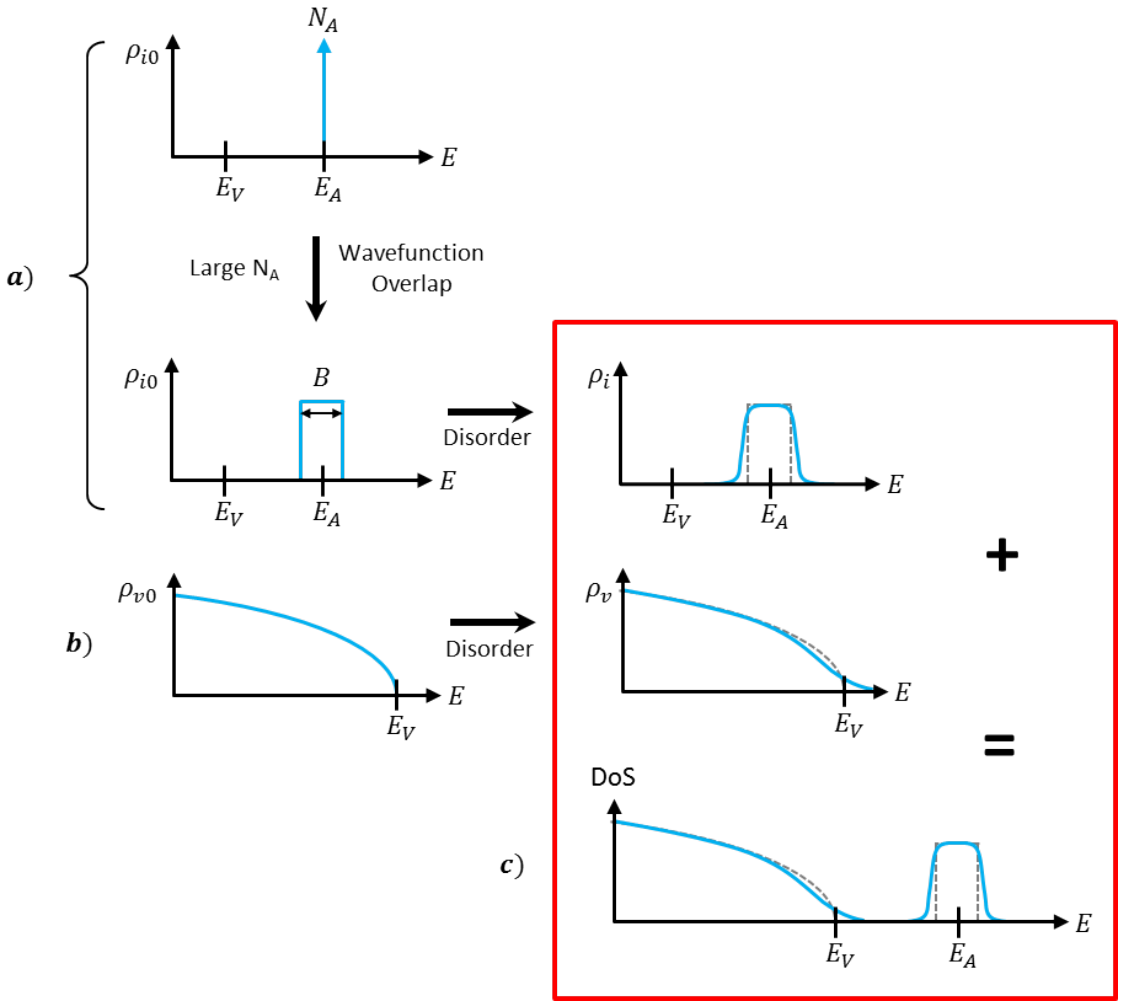

Figure 4.10: Evolution of the density of states under various conditions: **Row a)** Acceptor density of states starts as a single energy level at low doping, spreads due to wavefunction overlap at higher concentrations, then smears due to disorder **Row b)** Valence band density of states smearing due to disorder effects **row c)** Combined picture of the valence band and acceptor density of states

overlap, and density of states smearing due to disorder. To solve for the ionization ratio, charge neutrality is invoked in order to relate the hole concentration p to the ionized acceptor concentration N_A^- which are in turn both described by integral equations involving an occupation probability function and a density of states. In this work uncompensated p-type doping is considered, so N_D^+ is set equal to zero in the charge neutrality equation. Additionally, because this model is used to treat 4H-SiC, the intrinsic carrier concentration is extremely low (from $300 - 800$K $n_i \approx 10^{-8} - 10^{10}\text{cm}^{-3}$) so $n = n_i^2/p$ is assumed to be negligible.

Forms of impurity band conduction have been observed in SiC at high doping concentrations and in compensated samples [99,107], suggesting the need for a modification to the standard charge neutrality and incomplete ionization equations. To include this effect, the total number of mobile holes p is rewritten as a sum of 'normal' valence band conducting holes p^v and holes conducting via an impurity band mechanism p^i. Adopting this new form of p, the charge neutrality equation must also be rewritten because only the valence band holes contribute positive charge. The fraction of unionized acceptor states which contribute impurity conducting holes is quantified by the fraction $(1 - \beta)$. With these modifications, the ratio p/N_A given by Equation 4.51 is no longer technically the 'ionization fraction' because there are more mobile holes than ionized acceptors due to the additional impurity conduction holes (although this distinction is not always made).

$$p = p^v + p^i \tag{4.47}$$

$$p^v + N_D^+ = n^c + N_A^- \tag{4.48}$$

$$p^i = (1-\beta)N_A^0 \tag{4.49}$$

$$N_A = N_A^0 + N_A^- \tag{4.50}$$

$$\frac{p}{N_A} = \beta\frac{p^v}{N_A} + (1-\beta) \neq \frac{N_A^-}{N_A} \tag{4.51}$$

Impurity conduction effects have also been observed in Si [97,98,108], which is where this modification to the incomplete ionization formula was originally applied [97,98]. In these papers, the parameter β is obtained using the empirical expression in Equation 4.52 which is also applied in this work.

$$\beta(N_A) = \frac{1}{1+\left(\frac{N_A}{N_b}\right)^d} \tag{4.52}$$

Here, N_b characterizes the doping level at which the impurity conduction begins to dominate, and d characterizes the rate at which the conduction increases in the regime of the impurity conduction mechanism.

To ensure that p^v is correct in the case of high doping when the Fermi Level approaches the valence band edge, the full Fermi-Dirac integral (Eq. 4.53) is used to calculate the valence band hole carrier concentration in stead of using the Maxwell-Boltzmann approximation. The unknown Fermi level E_F is determined by solving the charge neutrality equation (Eq. 4.55). As mentioned earlier, there is no counter doping present, and the free electron concentration is neglected. The integral used to compute the ionized acceptor states (Eq. 4.54) uses a modified Fermi-Dirac function

due to the degeneracy g_A associated with filling the state in different ways. In the case of 4H-SiC, $g_A = 4$ due to the valence band maximum exhibiting a heavy-hole light-hole degeneracy, which allows for the creation of either a heavy-hole or a light-hole in the valence band, in addition to the choice of spin 'up' or spin 'down' for an electron filling the acceptor state [65, 66, 72, 98, 102, 103, 108–118].

$$p^v = \int_{-\infty}^{E_V} \frac{\rho_v(E)}{1 + \exp\left(\frac{E_F - E}{k_B T}\right)} dE \tag{4.53}$$

$$N_A^- = \int_{-\infty}^{\infty} \frac{\rho_i(E)}{1 + g_A \exp\left(\frac{E - E_F}{k_B T}\right)} dE \tag{4.54}$$

$$p^v = N_A^- \tag{4.55}$$

From the charge neutrality condition and integral equations, we have three equations and three unknowns p^v, N_A^-, and E_F. Plugging in equations 4.53 and 4.54 into equation 4.16, allows for the Fermi level E_F to be determined numerically using trapezoidal integration combined with the method of bisection for a given doping N_A. Once the correct Fermi level is found, we evaluate the integrals in equations 4.53 and 4.54 to calculate p^v and N_A^-. These values are then used in Equation 4.51 to find the ratio of mobile holes to acceptor doping p/N_A. For solving a compensated system (doped with both N_A and N_D), the slightly modified equations are discussed in the appendix.

I would like to emphasize for the sake of contrast with the model described in the next section that the only empirical inputs into this theoretical model are the logistical parameterization of the doping-dependent ionization energy $\Delta E_A(N_A)$

(Equation 4.34) and the impurity conduction parameter β (Equation 4.52) which are both extracted to match experimental data.

4.7 Experimental Incomplete Ionization Verification

In the previous section p/N_A was calculated from a largely theoretical standpoint. This section discusses the separate experimental technique used to verify the theoretically calculated p/N_A. This experimental technique described by Altermatt et al uses measured values of Hall mobility and resistivity over a range of doping densities from the literature [96–98]. With this data, a second p/N_A ratio is ultimately extracted and compared to the results from the theoretical technique. The core of this experimental method relies upon equating p/N_A to a ratio of mobilities μ_{Cond}/μ_{Hall} where the Hall mobility is measured directly and the conductivity mobility is derived from resistivity measurements.

Resistivity data (taken with 4-point measurements) is converted into a corresponding conductivity mobility value μ_{Cond} using Equation 4.56. The derived conductivity mobility is then divided by the measured Hall mobility μ_{Hall} to obtain experimentally obtained values of p/N_A. The hall correction factor r assumed to be 1 in this work [103, 119–122].

$$\mu_{Cond} \equiv \frac{1}{q\rho N_A} \tag{4.56}$$

$$\mu_{Hall} = \frac{\sigma R_H}{r} = \frac{1}{rq\rho p} \tag{4.57}$$

$$\frac{\mu_{Cond}}{\mu_{Hall}} = \frac{rp}{N_A} \approx \frac{p}{N_A} \tag{4.58}$$

Because the fraction μ_{Cond}/μ_{Hall} is used to obtain p/N_A, each of these mobilities must be representable as continuous functions of the doping N_A. To achieve this, each set of data is separately fit to an empirical function using the least-squares method. The experimentally-derived p/N_A is then compared to the p/N_A calculated using the theoretical model.

For clarity, the theoretical model does rely on a small degree of experimental input, namely, the experimental $\Delta E_A(N_A)$ and $\beta(N_A)$ which were presented in the previous section. The experimental data used in the theoretical model is, however, largely unrelated to the data which forms the experimental model because the different data sets are measuring completely different physical properties. This should allow the experimental model to act as a valid check on the result from the theoretical model.

$$\mu_{Hall}(N_A) = \frac{\mu_{Hall0}}{1 + \left(\frac{N_A}{N_H}\right)^b} \tag{4.59}$$

$$\mu_{Cond}(N_A) = \frac{\mu_{Cond0}\left(-\gamma + \sqrt{\gamma^2 + 2\gamma N_A}\right)}{\left(1 + \left(\frac{N_A}{N_C}\right)^c\right) N_A} + \mu_{Imp} \tag{4.60}$$

$$\gamma(N_A) = \frac{N_V}{2g_A} \exp\left(-\frac{\Delta E_A(N_A)}{k_B T}\right) \tag{4.61}$$

$$\mu_{Imp}(N_A) = \mu_{Imp0} \exp\left(\frac{-(N_A - N_{Imp})^2}{2\sigma_{Imp}^2}\right) \tag{4.62}$$

The Hall mobility is fit using the standard Caughey-Thomas [123] form often used in literature [71, 72, 112, 114, 115, 117, 122, 124–126]. The fit for conductivity mobility is derived partially from physical considerations, the details of which are described in the Appendix (Section B.1.1). With the analytical forms for μ_{Hall} and μ_{Cond} given by Equations 4.59-4.62, their ratio provides an analytical form for p/N_A. The result of this calculation is presented in Figure 4.14 later in this work.

The parameters used in the theoretical and experimental models are presented in Table 4.1. With the parameters in this table, the Hall mobility, ionization energy, and the hole concentration can be determined for a given acceptor doping density. Later in this work I will present a more usable approximate expression for calculating the p/N_A as a function of both acceptor concentration and temperature.

The plots of the physically-motivated empirical fits of μ_{Hall} and μ_{Cond} are shown in Figures 4.11 and 4.12 along with the respective experimental data from literature. The experimentally measured resistivity values are also plotted in Figure 4.13, which highlights the change in the conduction mechanism in the high doping regime. In this figure, at an Al doping concentration of approximately $10^{20} cm^{-3}$ a

Table 4.1: Parameters characterizing Al-doped 4H-SiC

	Parameter	Value
$\Delta E_A(N_A)$	ΔE_{A0} [meV]	214.86
	N_E [cm^{-3}]	8.12×10^{19}
	a	0.632
$\mu_{Hall}(N_A)$	μ_{Hall0} [cm^2/Vs]	109.6
	N_H [cm^{-3}]	2.92×10^{18}
	b	0.6335
$\mu_{Cond}(N_A)$	μ_{Cond0} [cm^2/Vs]	109.83
	N_C [cm^{-3}]	2.92×10^{18}
	c	0.5891
	μ_{Imp0} [cm^2/Vs]	1.355
	N_{Imp} [cm^{-3}]	2.65×10^{20}
	σ_{Imp} [cm^{-3}]	9.06×10^{19}
	N_V(300K) [cm^{-3}]	2.49×10^{19}
	g_A	4
$\beta(N_A)$	N_b [cm^{-3}]	4.5×10^{20}
	d	2.9

different conduction mechanism (likely a form of impurity or hopping conduction) seems to dominate as the slope of the trend changes. This concentration at which this slope change occurs agrees well with an estimated value of the critical concentration for impurity conduction [127] $N_{crit} = (2.2a_0)^{-3}\exp(1-\epsilon_r) \approx 1 \times 10^{20} cm^{-3}$ for 4H-SiC, where $\epsilon_r = 9.76$ [71]. The black dashed line in Figure 4.13 is generated using the resistivity equation provided by Heera et al. [10] with our own data as input.

From the data presented in Figure 4.11, the spread in experimental mobility

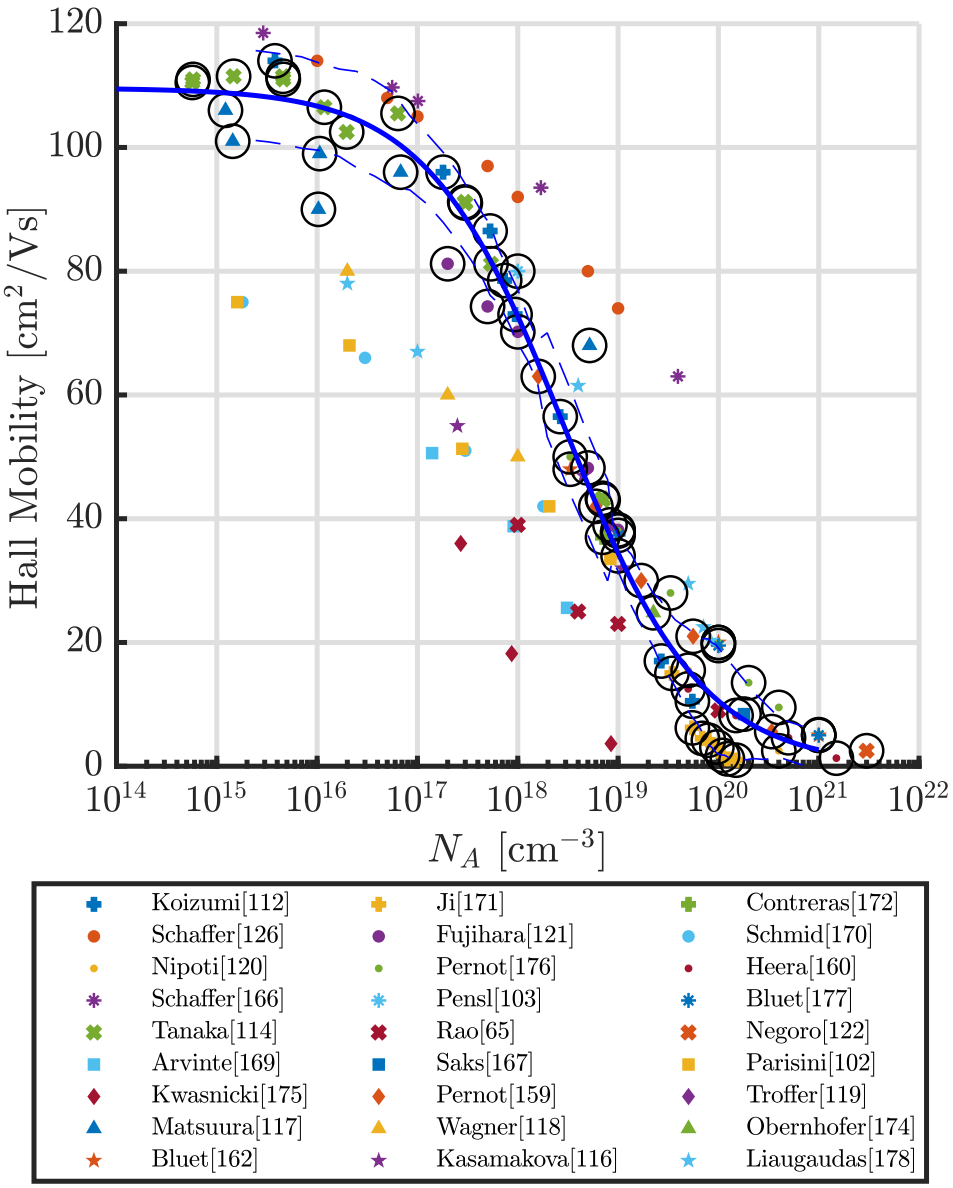

Figure 4.11: Hall mobility fit to experimental measurements of 4H-SiC doped with Al

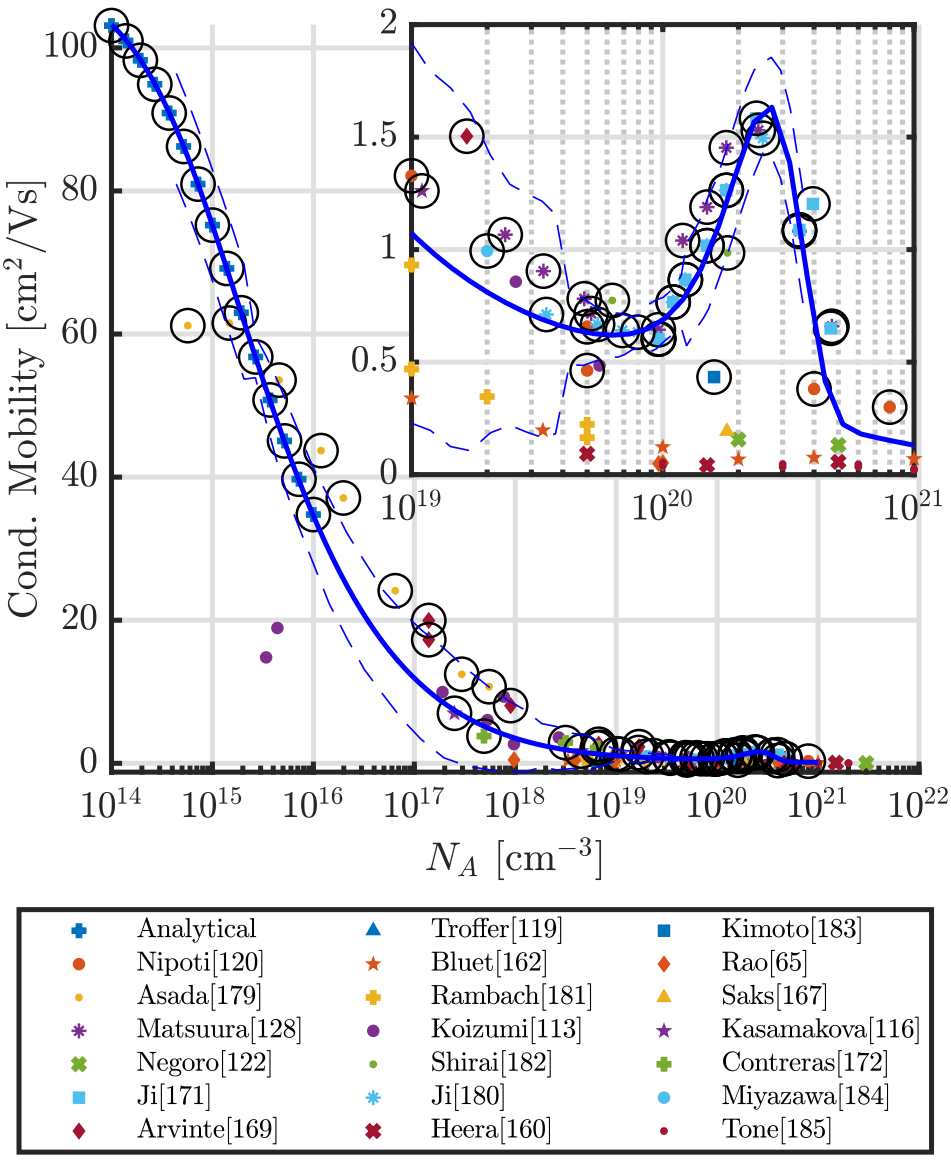

Figure 4.12: Conductivity mobility derived from experimental measurements of resistivity

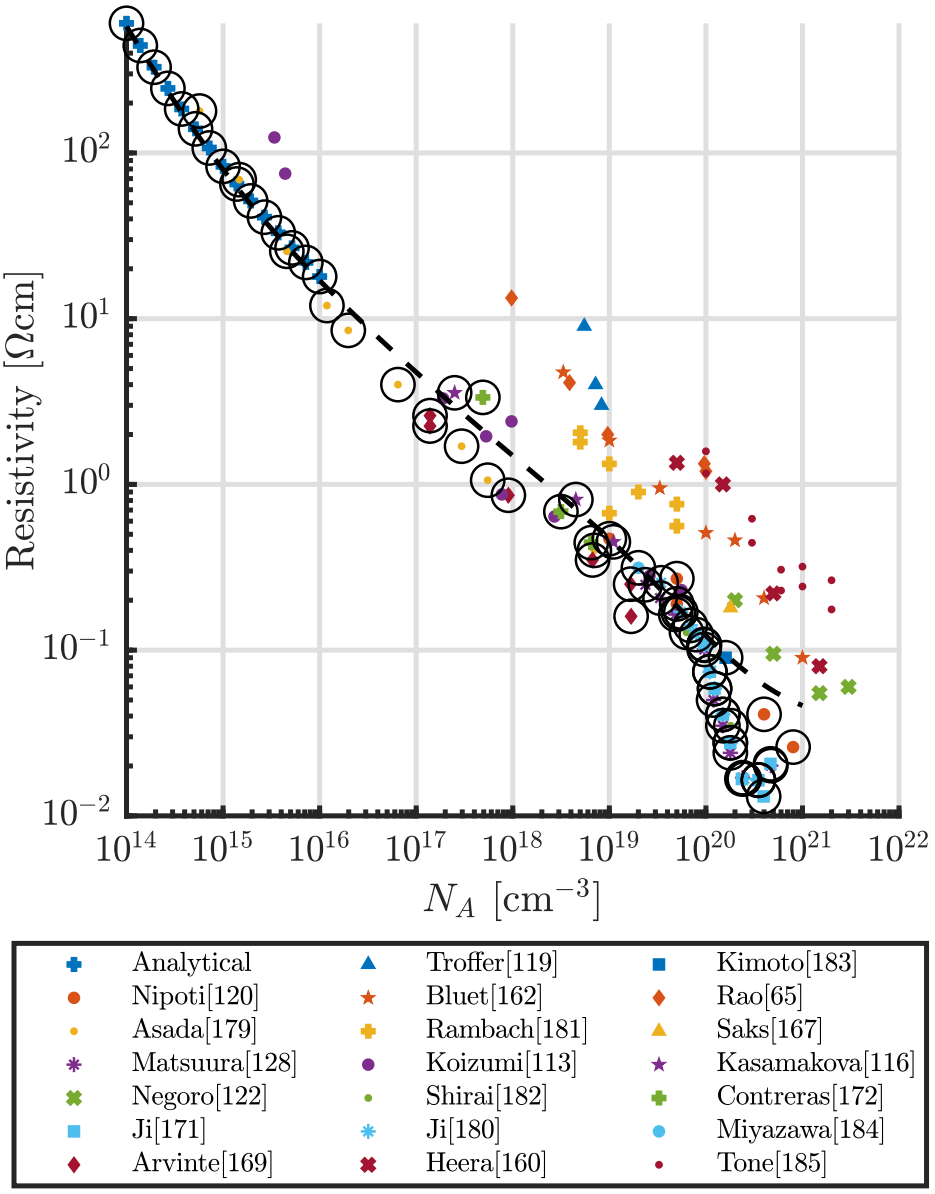

Figure 4.13: Resistivity fit to experimental measurements of 4H-SiC doped with Al. Dashed black line comes from using the predicted resistivity from Heera [10] using our values for mobility and ionization energy.

values is immediately obvious - likely due to the large differences in fabrication methods and parameters. This spread is also readily apparent in the resistivity data plotted in Figure 4.13. Interestingly, it turns out that all of the scattered data that lies above the dashed trend line in this plot for $N_A > 10^{18} cm^{-3}$ comes from devices doped using ion implantation as opposed to in situ doping via epitaxial growth. This suggests that it is difficult to repair the lattice damage caused by implantation and/or fully activate the implanted dopants.

To ensure a robust fit to the experimental data using Equations 4.59-4.62, outlier points are excluded on a paper-by-paper basis. The remaining data points, which are included in the least-squares error calculation, are outlined by black circles in Figures 4.11-4.13. The standard deviation $\pm\sigma_{err}$ of a 10 data point moving window is also plotted, shown as blue dashed lines.

Conductivity mobility (resistivity) data for extremely low doping concentrations is mostly unavailable due to difficulties obtaining completely pure samples, but is required because of how it will affect the quality of the fitting function in this region. For this reason, we add resistivity data points to the low doping region that are calculated using the simple charge neutrality condition valid for low doping [10] described in the Appendix 3 (Section B.1.1). These resistivity data points are labeled as Analytical in Figures 4.12 and 4.13.

The experimental incomplete ionization fraction is calculated by dividing the conductivity mobility fit curve (Equation 4.60) by the Hall mobility fit curve (Equation 4.59) as described in Equation 4.58. The resulting p/N_A fraction is presented as the solid blue line in Figure 4.14. The standard deviation error bars $\pm\sigma_{err}$ calcu-

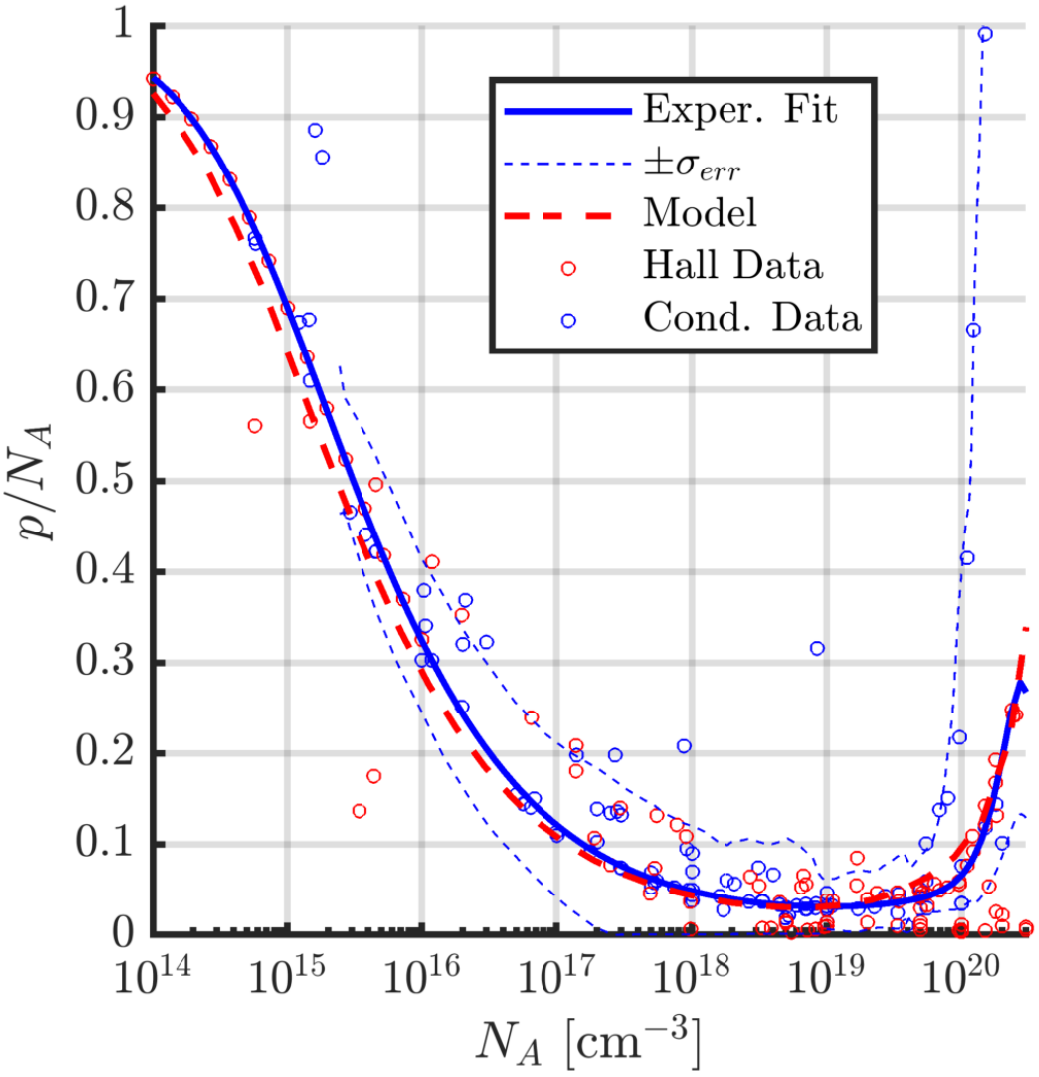

Figure 4.14: Incomplete ionization ratio p/N_A for 4H-SiC doped with Al at $T =$ 300K. Experimental data fit $(\mu_{Cond}(N_A)/\mu_{Hall}(N_A))$ is shown in solid blue. Our theoretical model, calculated with Equation 4.51 is shown in dashed red.

lated using a sliding window of 10 data points are also plotted as blue dashed lines in this figure. The upper and lower bounds are calculated by dividing the $\pm\sigma_{err}$ of the Conductivity curve by the $\mp\sigma_{err}$ of the Hall curve. The discrete points shown are the 'extracted' discrete p/N_A values calculated using: $\{\mu_{Cond}\}^*/\mu_{Hall}(\{N_A^{Cond}\}^*)$ (red circles) and $\mu_{Cond}(\{N_A^{Hall}\}^*)/\{\mu_{Hall}\}^*$ (blue circles) where $\{\}^*$ indicates the set of data points from the discrete measurements, and the functions indicate data calculated from the empirically fitted curves (Equations 4.59 and 4.60). In addition to the standard deviation lines, these data points help give some indication of the spread in the data about the direct division of the two fitted functions.

Result Comparison: Now that p/N_A has been extracted using experimental measurements, this result is used to confirm the values calculated using the theoretical model presented in Sections 4.3-4.6. The theoretical model results are plotted as the red dashed line in Figure 4.14 and for comparison, the experimental model predicts the solid blue line. Upon comparing the theoretical results with the empirically fitted, good agreement is found to within several percent.

4.8 Temperature Dependence

Because the theoretical model from Sections 4.3-4.6 is fully temperature dependent, it can be used to predict the p/N_A ratio at elevated temperatures, which will often be the more relevant operating regime for SiC devices. Figure 4.15 shows our predicted p/N_A for elevated temperatures, although these values are not yet confirmed with experimental data.

Due to the non-analytical form of p/N_A derived using the theoretical model

described in Sections 4.3-4.6, and the significant number of parameters needed to express the experimental data, a more usable form of p/N_A for device designers is desirable. The results of the temperature-dependent theoretical model are closely approximated by the analytical expression in Equation 4.63. Optimal parameters used in this expression are obtained by utilizing a genetic algorithm. The form of this expression is derived from an expression presented by Kuzmicz [108]. This parameterization was obtained for the following doping and temperature ranges, respectively: $10^{14}\text{cm}^{-3} \leq N_A \leq 3\times10^{20}\text{cm}^{-3}$ and $300\text{K} \leq T \leq 800\text{K}$. The benefit of using this expression enables scientists and engineers can simply evaluate Equation 4.63 for their given temperature and doping conditions directly instead of having to iteratively solve the nonlinear system of integrals described in Sections 4.3-4.6 for each doping and temperature point.

$$\frac{p}{N_A} \approx 1 - A\exp\left[-\left(B\left|\ln(N_A/N_0)\right|\right)^C\right] \tag{4.63}$$

Starting with the expression used by Kuzmicz [108] for Si, a temperature dependence to the parameter C is added to help better match the theoretical model results of p/N_A for p-type 4H-SiC. The values of A, B, C, and N_0 were optimized for Al-doped 4H-SiC using a genetic algorithm with a squared error fitness function. This parameterization is plotted in Figure 4.15 with a dashed line and agrees well with the theoretical model results with a significant reduction in computational effort. The full temperature dependent parameters A, B, C, and N_0 were found to

be:

$$A(T) = 0.9611 \left(\frac{T}{300} \right)^{-0.2343} \tag{4.64}$$

$$B(T, N_A) = \begin{cases} 0.0978 \left(\frac{T}{300} \right)^{0.7748} & N_A < N_0 \\ 0.3702 - 0.0347 \left(\frac{T}{300} \right) & \text{otherwise} \end{cases} \tag{4.65}$$

$$N_0(T) = 2.7248 \times 10^{19} \left(\frac{T}{300} \right)^{0.968} \text{cm}^{-3} \tag{4.66}$$

$$C(T) = 5.4738 - 1.2263 \left(\frac{T}{300} \right) \tag{4.67}$$

Plotting the theoretical model data in a different manner, Figure 4.16 shows the total mobile hole concentration p calculated by multiplying the theoretical model results in Figure 4.15 by N_A. From these high temperature calculations, the temperature dependence of hole concentration seems to diminish as the impurity band conduction mechanism begins to dominate at around $2 \times 10^{20} cm^{-3}$ for all temperatures considered. Further experimental measurements at elevated temperature are needed to confirm this prediction.

4.9 Results and Conclusion

From the gathered resistivity data, a consistent relationship between acceptor doping concentration N_A and resistivity is observed for epitaxially grown layers doped with Al. In contrast, samples which are doped by implantation consistently exhibit on the order of 10× higher resistivity compared to epitaxially grown layers of the same doping concentration but even among this data there is a large spread in values. This result is likely attributable to residual damage sustained during the implantation process as well as incomplete high temperature activation of dopant

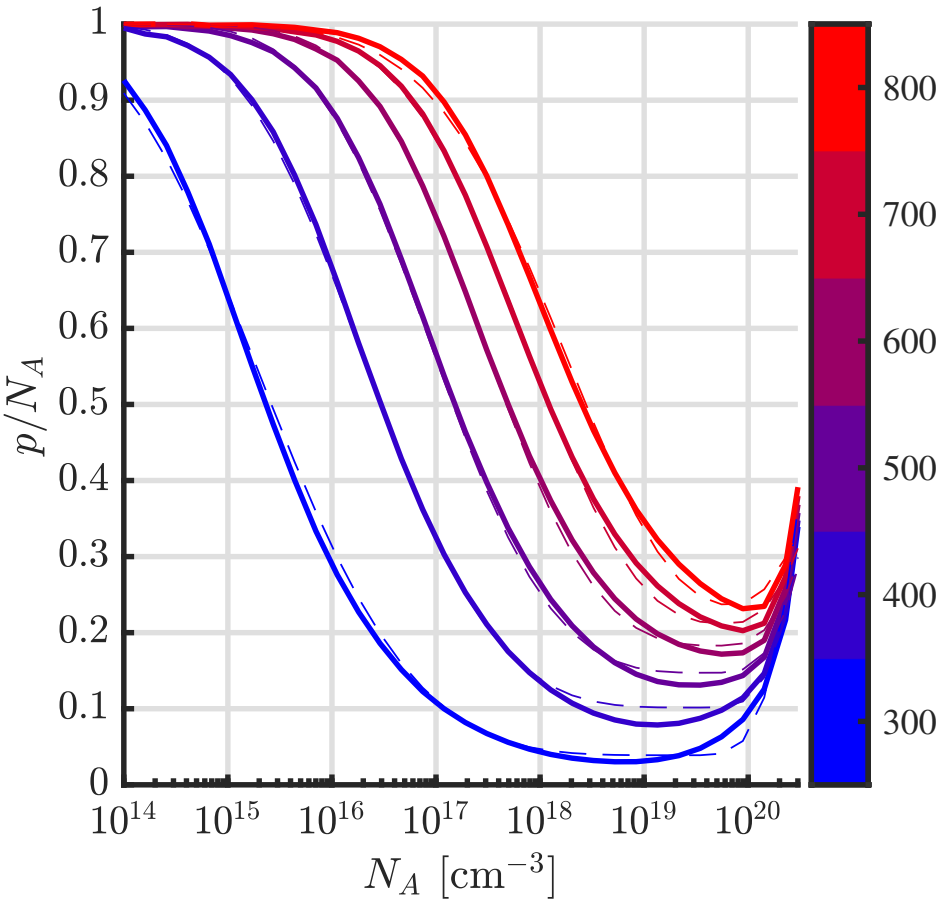

Figure 4.15: Incomplete ionization ratio p/N_A calculated using our Model at elevated temperatures $T = 300K - 800K$ (solid line) compared to our empirical parameterization (dashed).

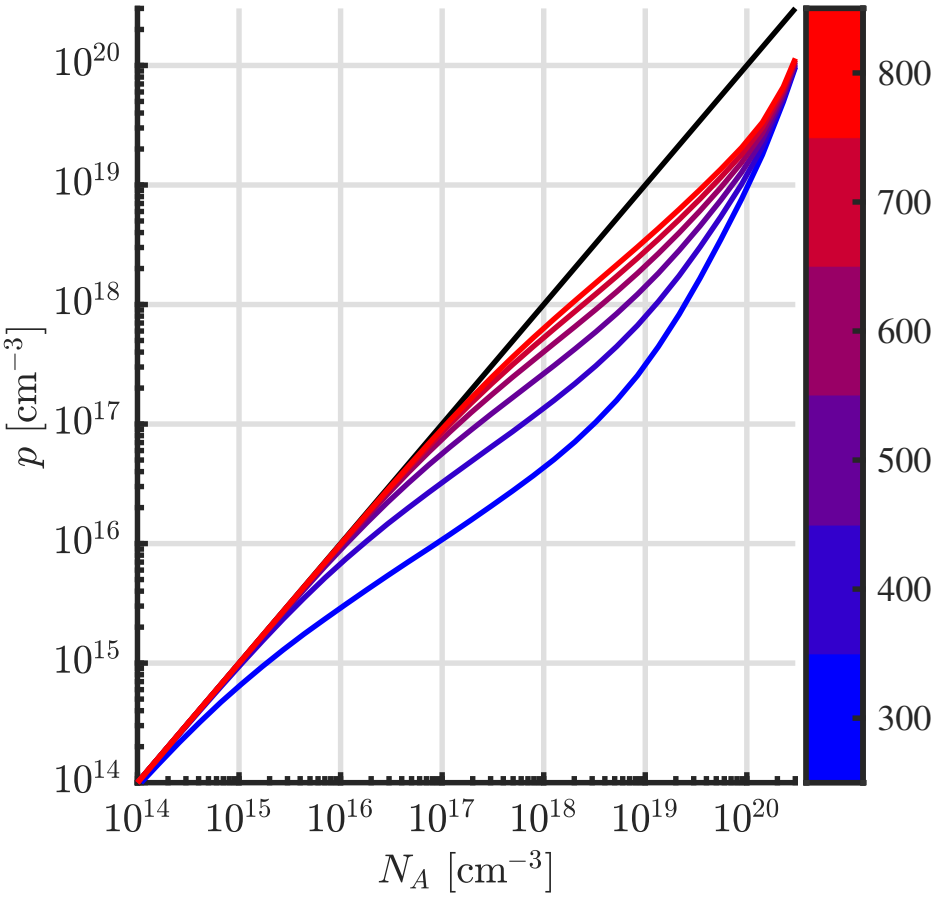

Figure 4.16: Hole concentration in 4H-SiC doped with Al calculated using our Model at elevated temperatures $T = 300K - 800K$.

atoms into lattice sites. Both of these issues are apparently unable to be fully rectified by the annealing process which generally follows implantation.

At an Al doping concentration greater than 10^{20}cm^{-3} the start of a parallel form of conduction is observed which is likely a type of impurity band conduction known as variable range hopping [128, 129]. The parallel conduction mechanism causes the resistivity to rapidly decrease with increasing doping concentration. This increase in conduction is quickly counteracted by the solid solubility limit of Al in 4H-SiC [130] which is around $2 \times 10^{20}\text{cm}^{-3}$. Beyond this limit the resistivity is observed to increase with further doping instead of decrease. The specific mechanism is not investigated in this work but may potentially be attributed to multiple effects including the formation of precipitated clusters of Al [64, 130, 131] which would increase scattering due to the non-crystalline structure as well there is a potential that holes conducting via impurity states may exhibit a higher effective mass.

Both the theoretical model and experimental data indicate that Al doping concentrations between 10^{17}cm^{-3} and 10^{20}cm^{-3} typically result in mobile hole concentrations equal to 10% or less of the doping concentration. This poses a challenge for semiconductor device designers trying to achieve low resistivity p-type regions in devices. The minimum p/N_A ratio predicted by the theoretical model is below 30% even at temperatures as high as 800K.

Chapter 5: Transport Model Validation and Genetic Algorithm Application

5.1 The Monte Carlo Method

In principle, to simulation carrier motion within a semiconductor we would need to solve the Boltzmann transport equation (BTE). The BTE, shown in Equation 5.1 is a nonlinear differential equation which provides us with a probability distribution function f_k in 3 dimensions of space, 3 of momentum, and one of time [132–134].

$$\frac{\partial f_k}{\partial t} = -\frac{1}{\hbar}\nabla_k E \cdot \nabla_r f_k + \frac{eF}{\hbar} \cdot \nabla_k f_k + \left(\frac{\partial f_k}{\partial t}\right)_{scatter} \tag{5.1}$$

$$\left(\frac{\partial f_k}{\partial t}\right)_{scatter} = \frac{V}{(2\pi)^3}\sum_i^M \int \left[f_{k'}(1-f_k)S_i(k',k) - f_k(1-f_{k'})S_i(k,k')\right] d^3k'$$

In this equation, the distribution function is evolved in time due to the effects of drifting and scattering in an applied field. Due to the complexity associated with solving for this function in a 6-dimensional phase-space directly, we instead employ the use of the Monte Carlo Method to obtain a solution instead. The aim of the this technique is to model electron transport by generating numerical results statistically through a repeated random sampling process. This method allows us to take calculated scattering rates and follow an electron on it's trajectory as it travels through a crystal, scattering via random mechanisms with appropriately

weighted probabilities. During the flight of the electron through the crystal, we also collect statistics about its energy, velocity, and valley occupation. Generally, it is assumed that each scattering particle acts independently from all other carriers, so the statistics generated from following one carrier undergoing many events should be representative of the ensemble of many carriers all mutually scattering.

Figure 5.1 lays out the flowchart the Monte Carlo algorithm follows. To simplify, first a total scattering rate is calculated for an electron given its initial energy. Then, a flight time is randomly determined from an exponential distribution. This flight time represents the amount of time the electron is drifting under the effect of the electric field and accelerating uninhibited. During the flight the electron's **k** vector changes according to 3.17. At the end of the flight the electron scatters according to a randomly chosen mechanism with probability proportional to each mechanism's individual scattering rate. After deciding the mechanism, the electron's energy changes by an amount determined by the phonon energy associated with the mechanism. Finally, the electron's **k** vector is updated to the new **k'** direction after scattering interaction with a phonon of wavevector **q**. Since there are generally many vectors which all have the same energy, the new vector is again chosen randomly from a distribution associated with the decided mechanism, and is based off the analytical form of the scattering rate. Certain mechanisms tend to prefer directional, anisotropic scattering and others are more isotropic. Finally, the entire process is then started anew and repeated many times to accrue sufficient data to produce meaningful averages and smooth distributions.

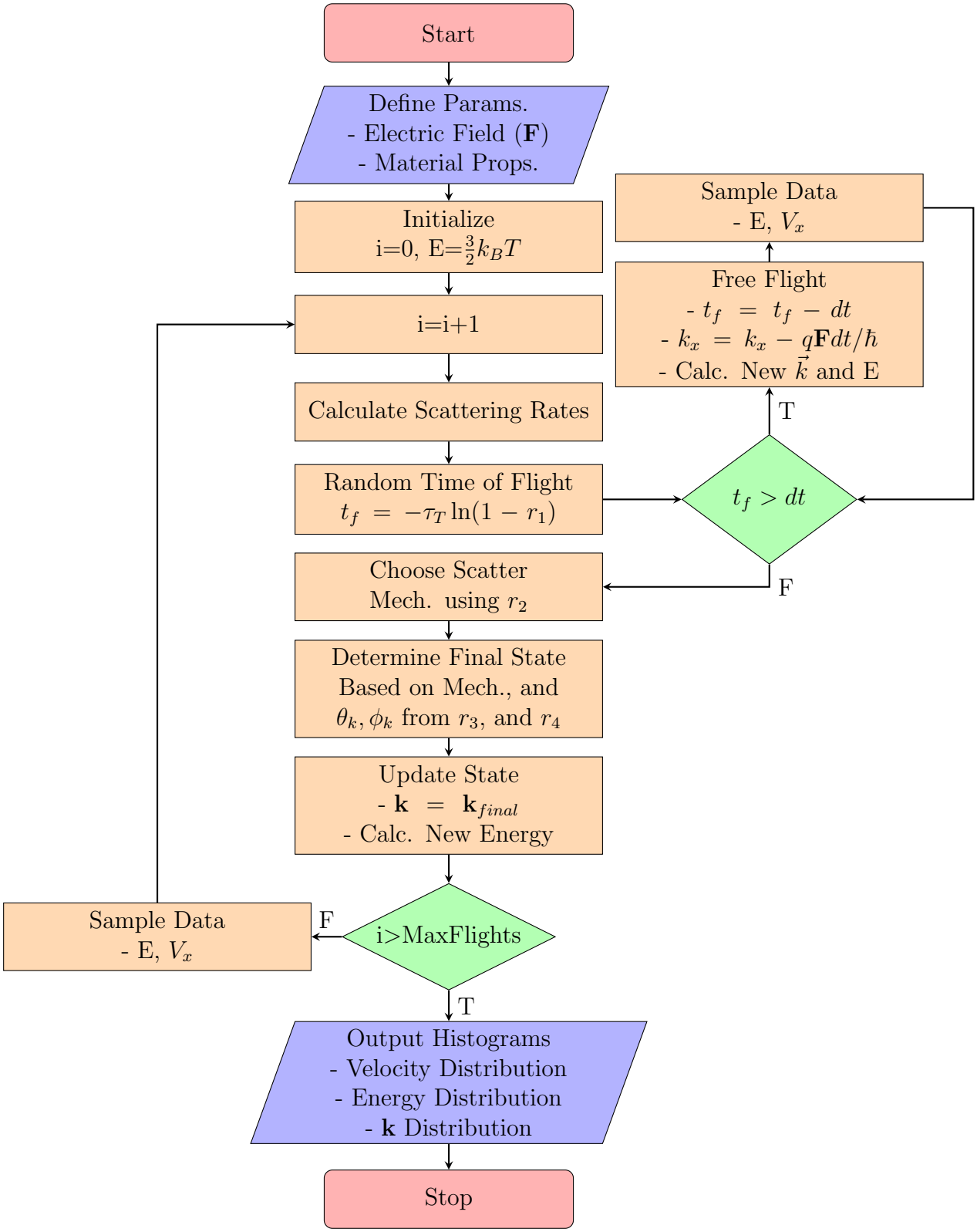

Figure 5.1: Flowchart of Monte Carlo Algorithm for a single field configuration using 4 random numbers r_1, r_2, r_3, and r_4

Calculations are performed using the algorithm for different strength electric fields. Averages are then taken for each calculation and plotted against the strength of the field. Of particular interest are the plots of average energy and average drift velocity (in the direction of the field). The derivative of the velocity with respect to field strength produces a plot of the differential field-effect mobility as a function of field. From the velocity plot, we can see material properties such as possible velocity overshoot and eventual saturation as the field gets too large.

Figure 5.2 shows the scattering rates of all mechanisms which we consider in the Monte Carlo simulation. The work done currently only includes the 3D mechanisms and is in good agreement with work previously done in the literature [40]. To maintain realism within our approximation, three subbands are chosen to account for a well configuration at the onset of inversion where there is 1.4 eV of band-bending in the SiC ($10^{16} cm^{-3}$). The lowest three subbands for a well with surface field of 2MV/cm are 0.37, 0.66, and 0.89 eV above the conduction band minimum, allowing the electrons to have enough room to gain kinetic energy while remaining inside the well for relatively small applied lateral electric field. More subbands can be included depending on the actual well configuration being studied.

The 3D Monte Carlo simulation was performed for 4H-SiC with transport on the (0001) interface. Figure 5.3 shows the results of the time-averaged electron velocity determined as a function of applied lateral field. The velocity is taken to be the component only in the direction of the field so that the mobility extracted

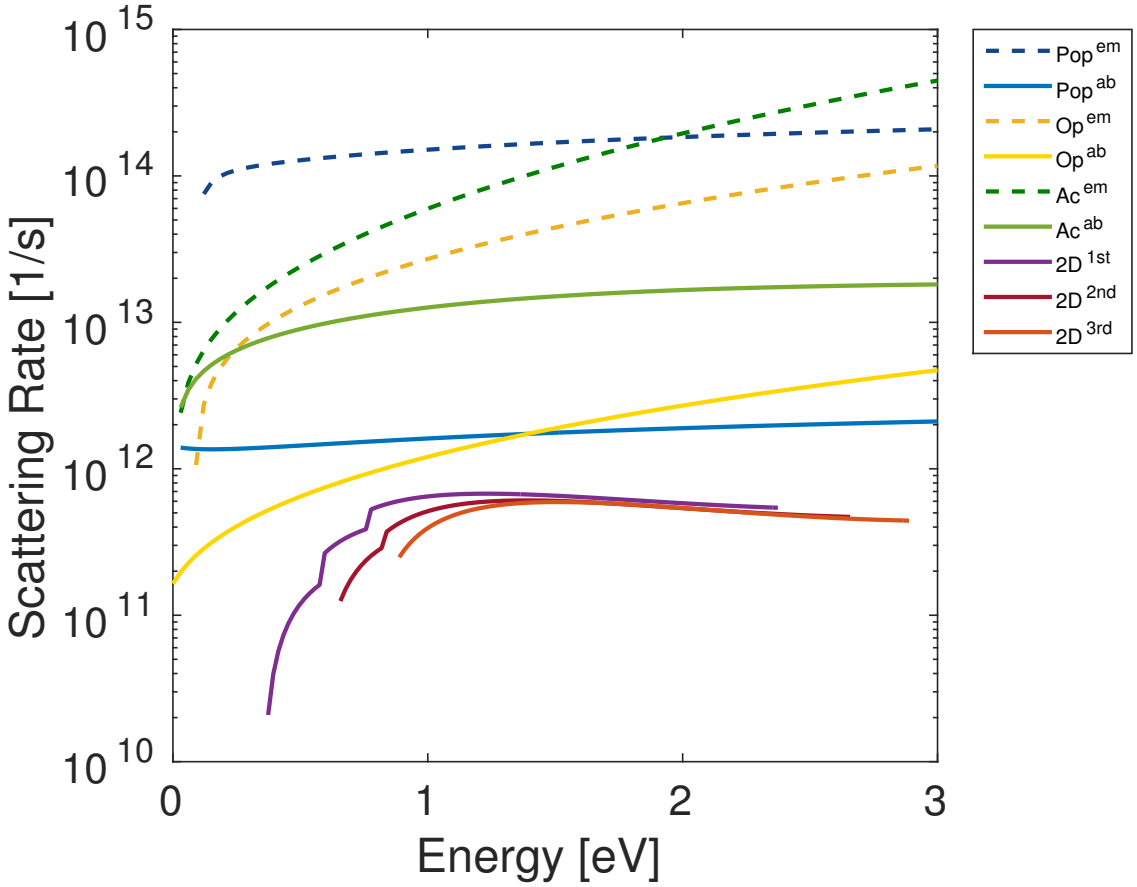

Figure 5.2: Scattering rates for electrons with different total energy. Rates associated with phonon emission are shown as dashed lines and solid lines are used for absorption. The 2D Atomic Roughness scattering rates out of the first three subbands are also shown for a surface field of 2MV/cm.

directly relates to the field as Equation 5.2.

$$\nu_{drift} = -\mu \mathbf{F} \tag{5.2}$$

For low electric fields, the drift velocity is known to increase linearly with applied field. From the results obtained, we see a velocity overshoot peak of approximately 1.7e7 cm/s at around 700kV/cm. The resulting value of this velocity peak agrees with its theoretically expected value which can be derived by equating the kinetic energy of the electron to the energy of the most probable phonon,

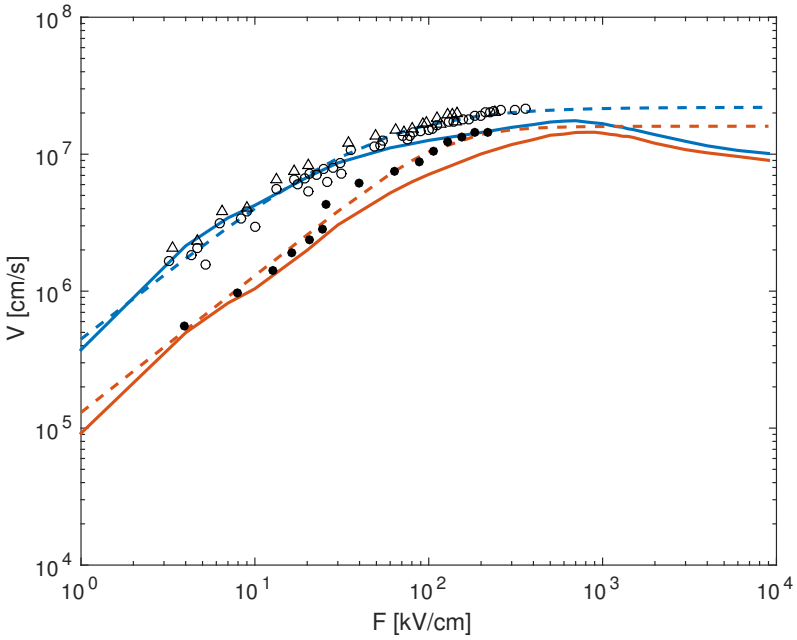

Figure 5.3: Average electron velocity (in the direction of the applied lateral field) plotted against field strength. Monte Carlo simulation results are solid lines and data-fitted curve from [11] is shown with the dashed line. Curves shown are for different temperatures: Blue 300K, Red 600K

and solving for the velocity the electron achieved before phonon interaction. To get the average velocity between scattering events simply divide the emission velocity by two. For SiC, polar-optical phonon emission accounts for the highest scattering rate and thus is the most probable interaction type. Using the values from the MC simulation results in a velocity saturation prediction of 1.7e7 cm/s.

$$\frac{m^*\nu_{emit}^2}{2} \approx \hbar\omega_{pop} \tag{5.3}$$
$$v_{sat} = \frac{1}{2}\sqrt{\frac{2\hbar\omega_{pop}}{m^*}} = 1.7e7 cm/s$$

Experimental data exists only up to 400kV/cm, where the velocity is fitted to saturate at 2.2e7 cm/s [11] (red curve in Figure 5.3), which agrees fairly well with our simulation results. Beyond this point, the results of the Monte Carlo show that the velocity overshoots and begins to decrease as it saturates due to the increasing

scattering rate of inelastic acoustic phonons. In an inelastic scattering event, kinetic energy of the electrons goes into the energy of the phonon, reducing the electron's speed after the event.

Because this calculation only includes M valley, all electrons exist in the lowest conduction band and thus have potential energy defined to be zero. The energy then shown in the Figure 5.4 represents both average total and average kinetic energy of the electrons in the material. From the plot we see that at the breakdown field of SiC (3MV/cm), the electrons have 1.7eV of kinetic energy which is reasonably small compared to the SiC/SiO_2 conduction band offset barrier of 2.7eV [135]. Additionally, from the distributions presented in Figure 5.5, at 3MV/cm the vast majority of electrons are still below 2.7eV but at this point the validity of the simulation begins to break down. At 700kV/cm where the average velocity is shown to peak, the energy distribution shows that almost all electrons have less than 1eV of energy. From the three energy distributions shown, we see that there is quite a drastic field dependence on the shape and spread of electron energies. At low fields the distribution is similar to an exponential-decay and as field increases, the distribution peaks at higher and higher energies. The tail also follows the same trend and extends to higher energy as the distribution broadens. At the breakdown field, we see the energy distribution has transformed to a nearly Gaussian shape because the electron is scattering so frequently and constantly changing energy.

Absolute field effect mobility is calculated by dividing the electron velocity at a given field by the value of the field. To extract differential mobility the derivative

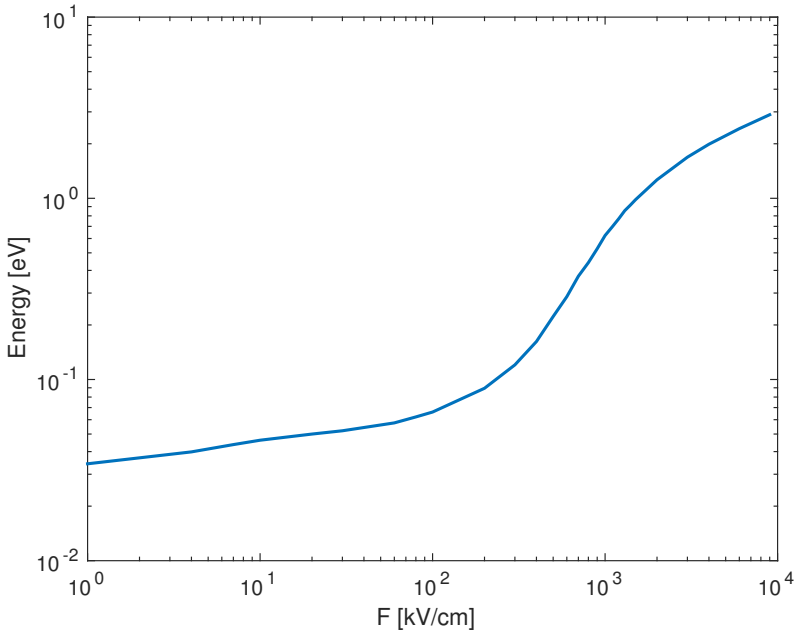

Figure 5.4: Plot of average electron energy for given lateral field strength. Zero energy corresponds to electrons at the conduction band minimum. Only M-Valley scattering is considered in this simulation.

of the average velocity vs field plot is taken. The results of both calculations are shown in Figures 5.6 and 5.7 respectively.

5.2 Conclusions and Future Work

Results of this Monte Carlo simulation closely match the experimental velocity data available for SiC from [11], and the MC simulation results of [40]. To extend this work, I plan to add the effects of 2D interface scattering within the quantum well to account for atomic and surface roughness scattering. Additionally, these simulations were performed assuming transport along the (0001) face (Si-face). Because my method for extracting an atomic roughness perturbation potential is general, the next step planned is to create and relax an a-face aligned interface supercell using

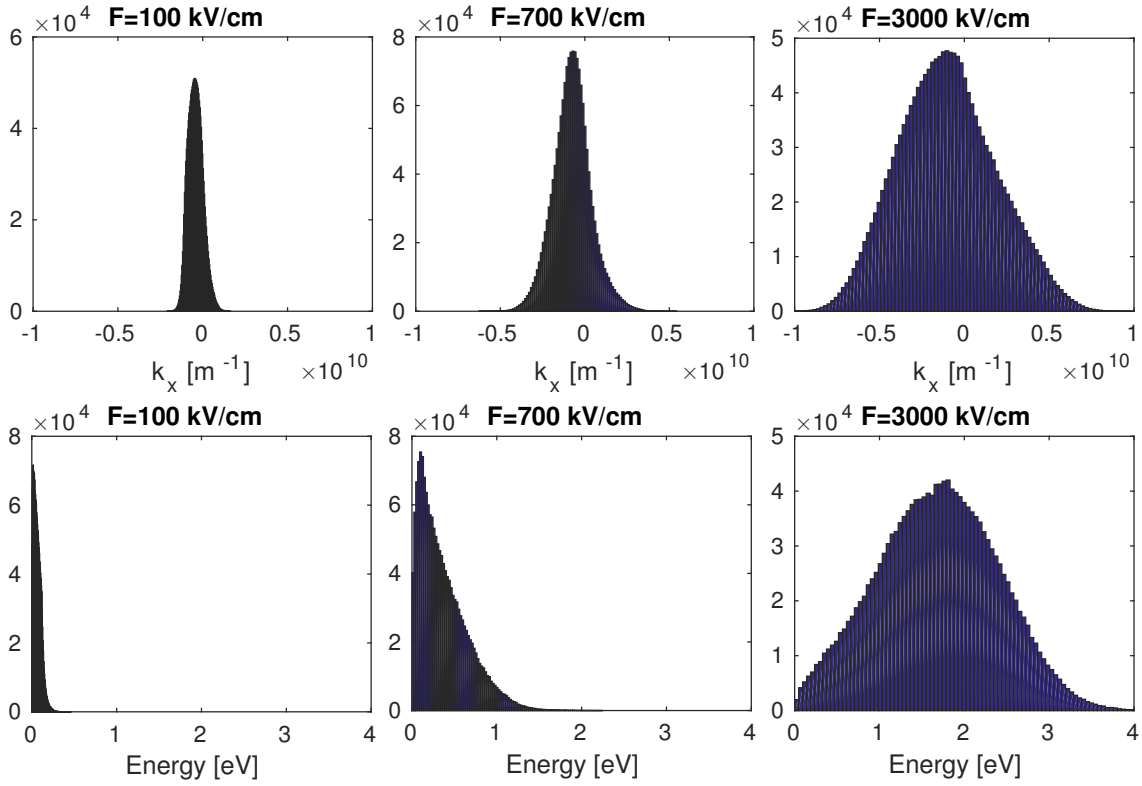

Figure 5.5: Distributions of wavevector component in the direction of applied lateral field (top) and electron energy (bottom) for various lateral field magnitudes.

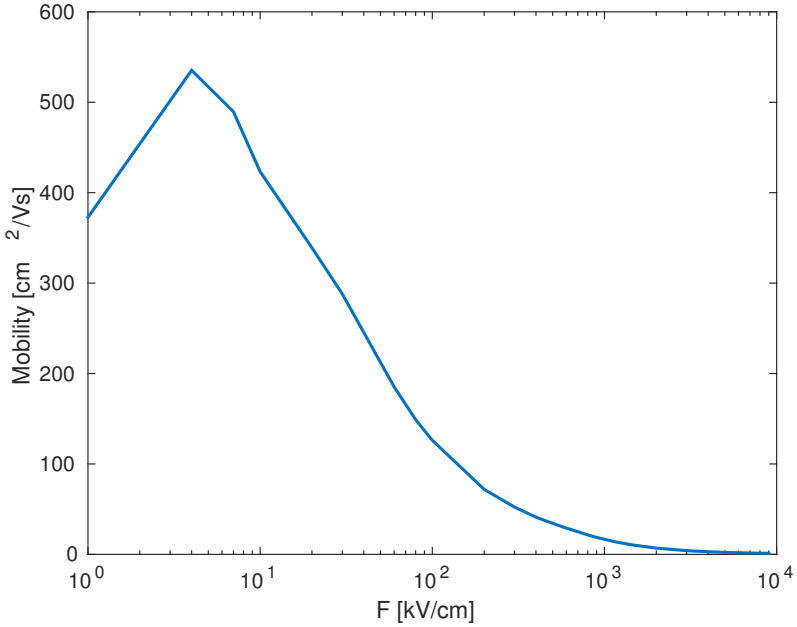

Figure 5.6: absolute field mobility for electrons plotted against applied lateral field, taken as $\nu(F)/F$.

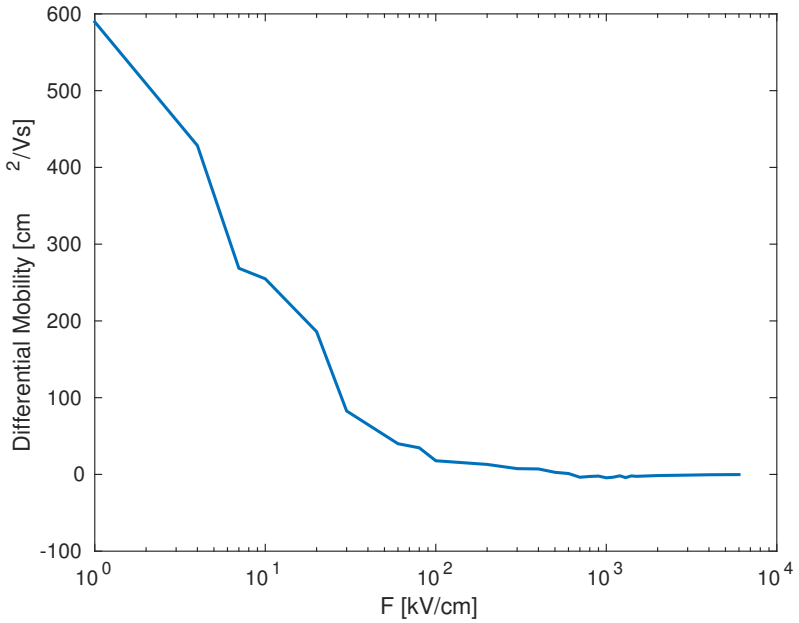

Figure 5.7: Differential electron field mobility as a function of field, extracted from Monte Carlo simulation results.

DFT. This work will allow for a comparison to be made between various interfaces to predict the mobility achievable in an ideal-case scenario where there is no surface roughness scattering due to the presence of a miscut.

5.3 Genetic Algorithm For Parameter Extraction

5.3.1 Method Overview

To develop a more usable form of the p/N_A results from Section 4.8 without the need to solve the complete iterative system of integrals, a genetic algorithm was designed an applied to determine optimal parameters for an empirical formula. In general, a genetic algorithm is a stochastic technique which uses concepts from biological evolution in order to optimize a function. For my purposes, the genetic algorithm is used to optimize a set of parameters for an empirical function to best

fit experimental data.

Each parameter set is denoted as an 'individual' and each parameter's value as a 'gene' in the context of the genetic algorithm. An individual's 'chromosome' is the combination of all of its genes. In the algorithm, many individuals make up a 'generation' and each are tested by calculating a fitness function for a given individual $\mathcal{F}_i$ (Eq. 5.4). The fitness function creates an objective ranking of the individuals by determining the 'goodness-of-fit' for each parameter set. In this case the fitness function for each individual is taken to be the least-squares error between the empirical function using that individual's parameter set $f_{i,empirical}(x)$ and the experimental data set $f_{data}(x_j)$. A weighting function $w(x)$ may also be added to ensure that fitting preferentially favors certain more sensitive or important regions or minimizes the impact of regions where experimental data is unreliable. The sum in Equation 5.4 is taken over the j experimental data points.

$$\mathcal{F}_i = \sqrt{\sum_j \left[w(x_j) \left(f_{i,empirical}(x_j) - f_{data}(x_j) \right)^2 \right]} \tag{5.4}$$

In the genetic algorithm, to limit memory usage, the population size is fixed such that each generation has the same number of individuals. Each generation of individuals is primarily made from 'breeding' the individuals from the previous generation to create new individuals. Mimicking the biological process of sexual reproduction, different genes are randomly taken from each parent and combined to create offspring. After each generation is created, old individuals die out and are replaced by their children and the cycle is repeated until a satisfactory fitness

level is achieved. The basic flow diagram of the genetic algorithm is shown below in Figure 5.8.

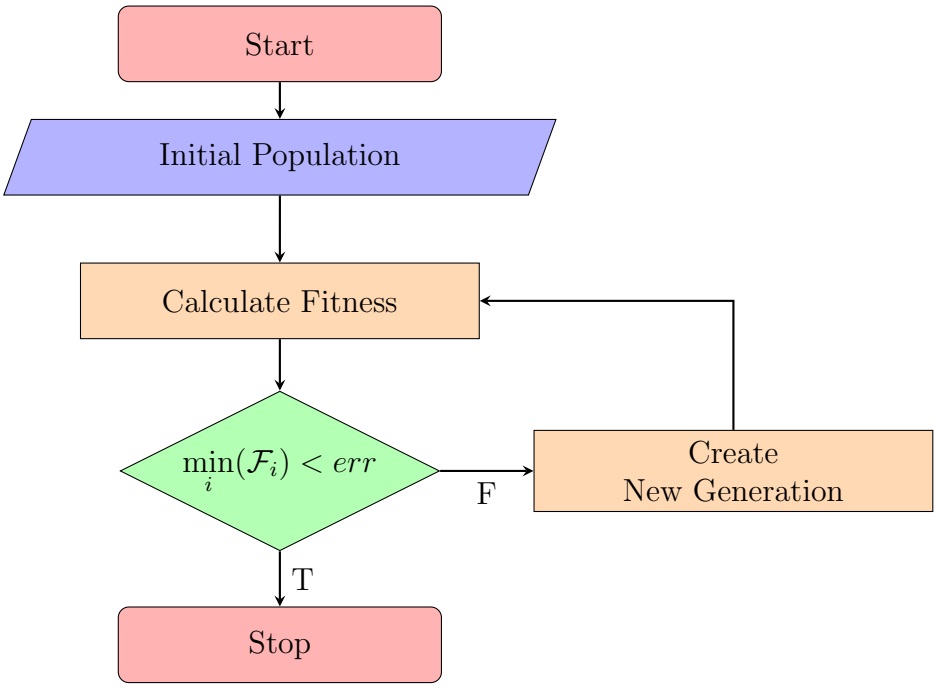

Figure 5.8: Flowchart of the basic Genetic Algorithm process.

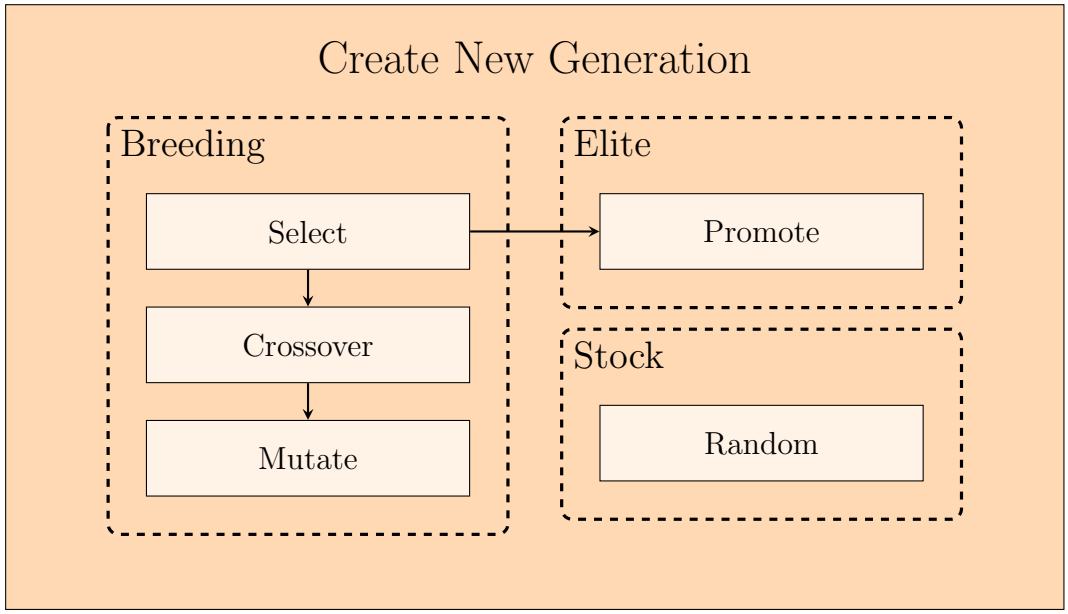

Figure 5.9: Operations performed to create a new generation of individuals in a genetic algorithm.

In the algorithm flowchart Figure 5.8, the initial population is created by assigning each individual's genes (parameter values) by selecting randomly from within the bounds of reasonable values set for each parameter. The fitness of each individual in the generation is then evaluated to assign a qualitative ranking of how well each individual fits the experimental data. The best fitness among the generation is then used to determine the if the algorithm is to stop by comparing it to a desired threshold value. If sufficient fitness is not achieved among any of the individuals of this generation, a new generation is created and the process is repeated. Figure 5.9 diagrams the process of creating a new generation showing its component groupings.

Every generation is based off of the previous generation except for the initial

population. The main bulk of the generation is created with a breeding process which selects parent individuals from the previous generation and 'breeds' them to create individuals in the new generation. Parents are selected randomly from the previous generation but preference is given to individuals with better fitness. This effect can be easily achieved by implementing a hard cutoff where the best X individuals act as the 'elite parent pool' from which the parents of a set number of children in the next generation are chosen. The remaining children are created by choosing completely random parents without any bias based on fitness. This ensures that the best X parents will have more representation (through their offspring) in the following generation. For simplicity of implementation, every pair of parents has one child, and individuals are not monogamous. Additionally, there is a chance that duplicate pairs may appear in which case that pair of parents ends up with multiple children. After selection of the parents, their child is generated with a two-step process: crossover and mutation, the details of which will be described later. Additionally, during the selection process, the best X individuals can also be promoted directly from the current generation into the new generation in a process known as 'Elitist Selection'. By adding this feature to the generation creation process, the current best solution is never forgotten, ensuring that the fitness function monotonically improves with each generation.

Earlier, it was mentioned that individuals with better fitness were selected more frequently to be parents. Doing this ensures that better individuals produce more children and, in effect, biases the algorithm to stay near solutions which are known to be good via the breeding process. However, this can eventually lead to

convergence issues. It is possible and indeed likely that many of the best individuals will start to become near-clones of each other i.e. the best individuals will have very similar genes. In effect, this causes the gene pool to stagnate and keeps the algorithm stuck in a local minimum of the fitness function rather than moving toward the global minimum. To help combat a stagnated gene pool, new 'stock' individuals are introduced to each generation as a supplement to all of the offspring made by breeding the previous generation's individuals. These 'stock' individuals have no parents and are created instead with purely random genes (like the initial population individuals) to promote genetic diversity further down the generations. The likelihood that these individuals themselves give highly fit solutions is low but they may introduce genes that aren't currently available elsewhere in the population that can lead to highly fit individuals after breeding.

5.3.2 Breeding Process Details

The breeding process selects two individuals as parents and mixes their genes to create an offspring. The selection of parent individuals is performed randomly but bias is given towards selecting individuals with better fitness. To generate a child from a given a pair of parents, the crossover operator is applied. Crossover is performed by generating a random bit array, with length equal to the number of genes in an individual. These bits then determine from which parent each gene of the child is to be taken i.e. for a '1' take parent 1's gene and for a '0' take parent 2's gene. Written mathematically: $G_{i,Child} = r_i G_{i,P1} + (1 - r_i) G_{i,P2}$ where r_i is the

i^{th} bit in the crossover array and the G_i terms are the i^{th} genes of the child and parent individuals. Due to the large number of possible crossover arrays, even if two individuals share the same parents, they will likely differ significantly from each other.

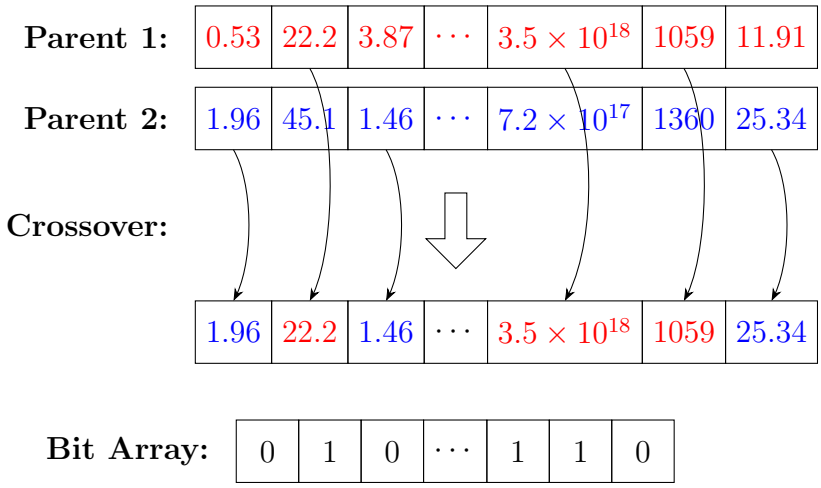

Figure 5.10: Random binary bit array used to generate an offspring from two parent individuals

After crossover, each new offspring is then subject to a mutation stage which adds some random spreading or broadening to the genes (parameter values). This can help to fine-tune the parameters in later generations once most of the major convergence has been achieved mainly due to crossover in the early generations. A simple way to add mutation is to multiply each of the child's genes by a random Gaussian variable centered at 1 using set standard deviations σ_i for each parameter $\mathcal{N}(\mu = 1, \sigma_i^2)$. As a note, for parameters which may span many orders of magnitude (such as doping concentrations, reference doping values, electron concentrations, oxide charge, etc.), it may be better to apply mutation to the log of the parameter

and then re-exponentiate to recover the final mutated value.

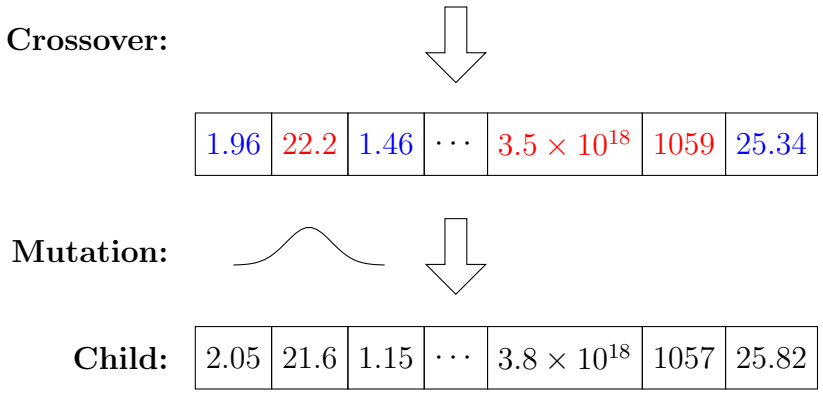

Figure 5.11: Random mutation applied after the crossover to finally create the offspring.

An alternative breeding strategy which could also be used is to form each child's genes via a random linear combination of it's parents genes instead of choosing the exact value of either parent. The crossover formula $G_{i,Child} = r_i G_{i,P1} + (1 - r_i) G_{i,P2}$ still applies, but now each r_i is a random variable which can vary continuously from 0 to 1 and is chosen from a distribution. In this strategy, r_i acts as more of a mixing fraction than a selector. For simplicity the distribution may be uniformly random to create more hybridized individuals, or it may have a more bimodal shape that is biased towards 0 and 1 to give more of a crossover effect (Fig. 5.12). Once again, for parameters that span many orders of magnitude this linear mixing should be performed on the log of the gene and then re-exponentiated to obtain the mixed value.

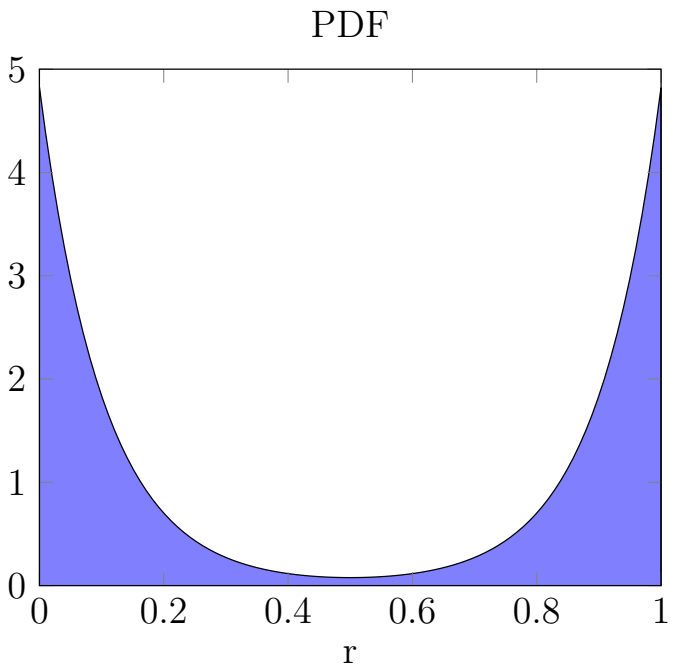

Figure 5.12: Example bimodal probability density function which could be used to pick random gene mixing fractions.

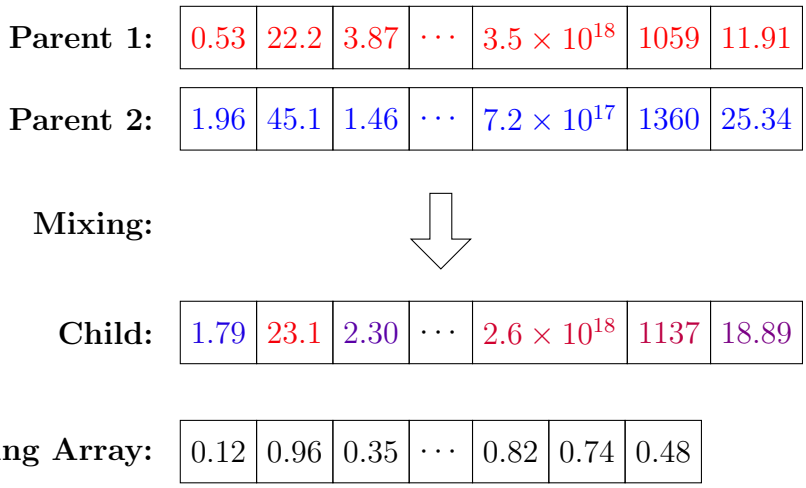

Figure 5.13: Child created using linear combinations of its parents' genes.

The values and rates of convergence achievable will depend on the problem being solved as well as the chosen form of the fitting function and the exact im-

plementation of the algorithm (size and proportions of individual groups in each generation, crossover and mutation functions, etc.). A good solution should be obtainable for most reasonable implementations given that the parameterized function has enough parameters to reasonably capture the shape of the data and the evolution is given enough generations to converge.

5.3.3 Genetic Algorithm Applied to Doping and Temperature-Dependent Hall Mobility

In researching incomplete ionization in Al-doped 4H-SiC, I gathered a large number of references and extracted thousands of measurements of Hall mobility taken under a wide range of doping and temperature conditions. As these conditions change, the hole concentration and the dominant scattering mechanisms vary. The combination of the way these two varying quantities interact give rise to dramatic variations in Hall mobility as a function of temperature and doping. Consequently, the shape of the Hall mobility function is complex and, given the large amount of experimental data, a genetic algorithm is the ideal choice for finding the optimal parameterization of an empirical Hall mobility fit. In this section I present my method and results for the temperature and doping-dependent Hall mobility function of Al-doped 4H-SiC.

Multiple runs of the algorithm have been performed starting from a new random population each time in order to demonstrate the convergence of the algorithm. The fitness of the current best individual is plotted against the generation number in

Figure 5.14 for each of these separate runs. Initially, the completely random initial populations (generation 1) give rise to a range of random fitness values from about 10 to 13 and within 10 generations, all lie between 8 and 9. Rapid improvements are made within the first 100 or less generations in all runs. Occasionally, large jumps in fitness can be seen which is when a 'breakthrough' is made. This generally occurs when a new individual is bred which overtakes the best elite candidate rather than the best candidate (or near-clones of it) making small improvements through slight mutation.

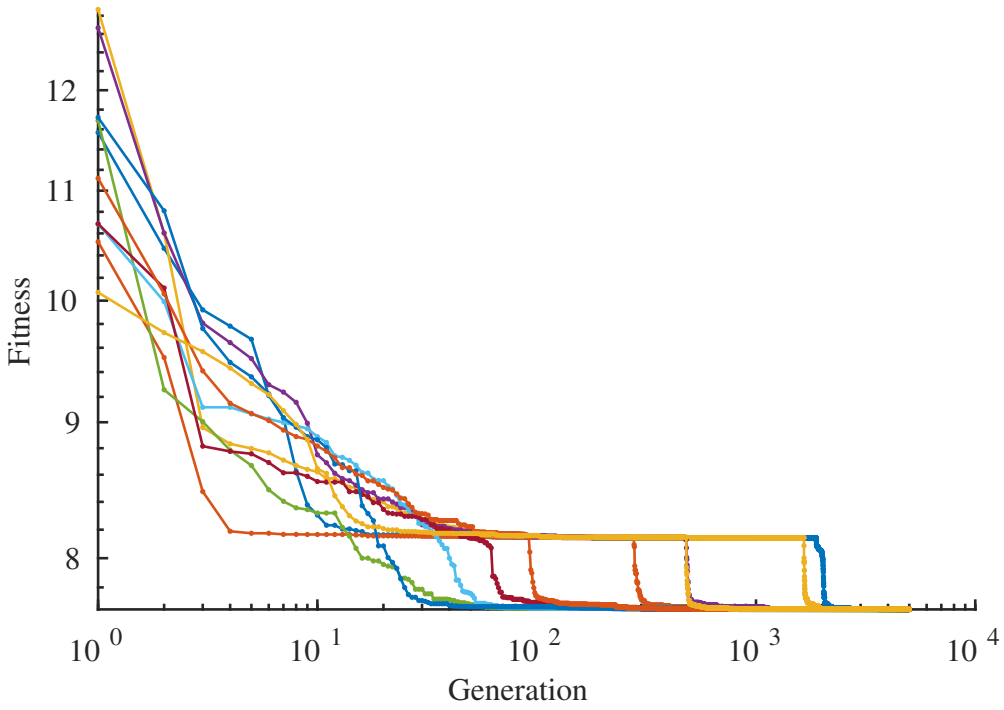

Figure 5.14: Fitness across generations for different runs of the algorithm.

It is interesting to note that for this particular fitting function and data set, about half of the runs got temporarily stuck in the same local minimum, where fitness stagnates at ~ 8.15 for a varying number of generations. It turns out that

this is a local minimum which contains nearly-optimized parameters for the majority of the fitting function, i.e. the mobility matches the data for most doping and temperature conditions, with the exception of the simultaneous high doping and low temperature region. As will be described later, the shape of the function in this specific region is mainly dominated via multiplication with a hyperbolic tangent function containing 4 parameters. Because the hyperbolic tangent goes to unity in every other region, these parameters are difficult for the algorithm to optimize. Changing the parameters in the hyperbolic tangent does not noticeably change the value of fitness as most of the data points exist outside this region where the fitting function is mostly insensitive to changes in these parameters. Only after the majority of the function has settled to near-optimized values does the fitness function have the sensitivity to determine how good or bad various values of the hyperbolic tangent parameters are. After this point, the algorithm can start to select better individuals which fit the data in this specific region and continue forward to the final fitting function which works across the entire space.

The Hall mobility function with the best fitness achieved is shown below in Figure 5.15, plotted against the scattered experimental data points taken from literature which is used to evaluate the fitness function. Vertical projection lines show the error between the fitting function and the experimental data. Not visible in the figure are the approximately equal number of data points which are underneath the fit surface which have an approximately equal amount of error to those above it.

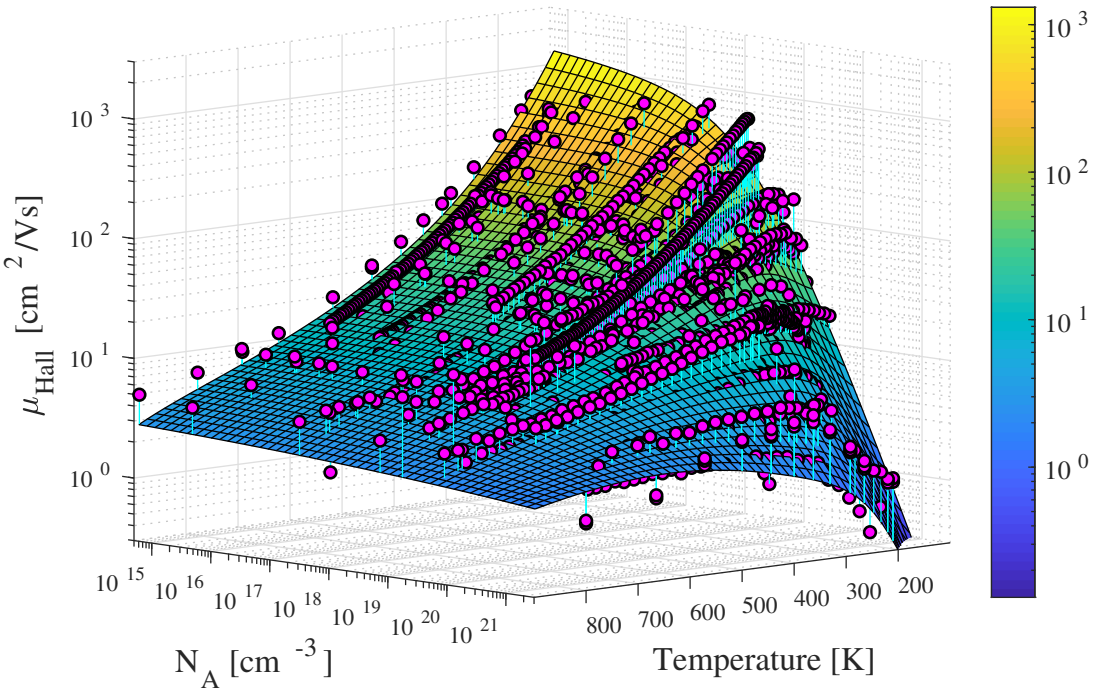

Figure 5.15: Genetic Algorithm fit of the doping and temperature-dependent Hall mobility of Al-doped 4H-SiC.

The empirical function used is a modified form of the Caughey-Thomas mobility model, with parameters given in Table 5.1:

$$\mu_{Hall}(N_A, T) = \mathcal{B}(N_A, T) \cdot \frac{\mu_0 \left(\frac{T}{T_{ref}}\right)^{-\gamma}}{1 + \left(\frac{N_A}{N_0 \exp\left(\frac{T}{T_0}\right)}\right)^{(\alpha - \beta T)}} \tag{5.5}$$

$$\mathcal{B}(N_A, T) = \frac{1}{2} \tanh\left(\Gamma \left[T - B\left(\frac{N_A}{N_{ref}}\right)^A\right]\right) + \frac{1}{2} \tag{5.6}$$

Table 5.1: Optimized parameters for empirical Hall mobility in Al-doped 4H-SiC obtained using a genetic algorithm

Parameter	**Value**
μ_0 [cm^2/Vs]	320.1
T_{ref} [K]	190.15
γ	2.926
N_0 [cm^{-3}]	3.8×10^{17}
T_0 [K]	108.6
α	0.959
β [K^{-1}]	9.5×10^{-4}
Γ [K^{-1}]	0.0139
B [K]	318.86
N_{ref} [cm^{-3}]	2.15×10^{23}
A	0.691

Chapter 6: Germanium Modeling

6.1 Introduction

Germanium is a group IV semiconductor commonly used in Short Wave Infrared (SWIR) optical devices due to its relatively small band gap of 0.66eV. Like silicon in the period above it, the conduction band minimum of germanium does not lie at the same point in k space as the valence band maximum, making it an indirect gap material and thus reducing its absorption efficiency. Unlike Si however, the direct gap of Ge is only slightly larger than its indirect gap energy. With clever bandgap engineering Ge is able to transition to a direct gap material. One such method showing promise is alloying Ge with Sn in various ratios. Using DFT we can calculate the effects the alloy has on the band structure for different percentages of tin and thus predict the percentage needed to transition germanium into a direct gap material.

Because the bandgap of Ge is indirect, it is an inefficient absorber of light meaning that incoming photons with energy close to the bandgap energy penetrate deeper into the material before being absorbed. If the absorbing material is made thick compared to the minority carrier diffusion length, generated carriers will be more likely to recombine before crossing the junction and thus will not be collected

- decreasing quantum efficiency. Additionally, thicker materials increase the chance of defects which can act as further sights of recombination. By using direct-gap semiconductors as the absorbing material, the active layer can be made thin and quantum efficiency can be kept high.

Absorption of light into a semiconductor is described by the Lambert-Beer Law (Equation 6.1), which uses a parameter known as the absorption coefficient which describes how the intensity of light with a given wavelength changes with depth into the material due to absorption. In Equation 6.1, I_0 is the monochromatic intensity at the surface, α is the absorption coefficient (a function of wavelength), and x is the depth into the semiconductor. The absorption coefficient α is also related to a material property known as the extinction coefficient κ by Equation 6.2.

$$I(x) = I_0 e^{-\alpha x} \tag{6.1}$$

$$\alpha = \frac{4\pi f \kappa}{c} \tag{6.2}$$

The absorption coefficient amalgamates details of the band structure and turns conduction band minima into kinks in the coefficient plot. As photon energies increase and, more states are available for valence band electrons to be excited to once the energy passes higher conduction band minima, making an excitation and thus an absorption more probable. Indirect minima show a quadratic dependence of the absorption on the energy and direct minima show an approximately square root dependence [136]. Figure 6.1 shows the absorption coefficient as a function of photon energy for select semiconductors which absorb in the visible and near-infrared. Here, we see that absorption starts in Ge and Si at 0.66eV and 1.15eV for

room temperature measurements, corresponding to their bandgap energies. For Ge absorption towards 0.8eV we see a transition into a rapidly increasing absorption due to the direct valley. The final bend corresponds to the second indirect minimum at 0.85eV. Further confirmation that the 0.8eV minimum is the direct gap value can be seen by looking at the low temperature curve. At low temperatures, it is less likely for an electron to be excited into an indirect minimum because there are less phonons available to assist the momentum transfer needed. Because of this, absorption starts closer toward the energy of the direct gap as the indirect transitions become increasingly unlikely.

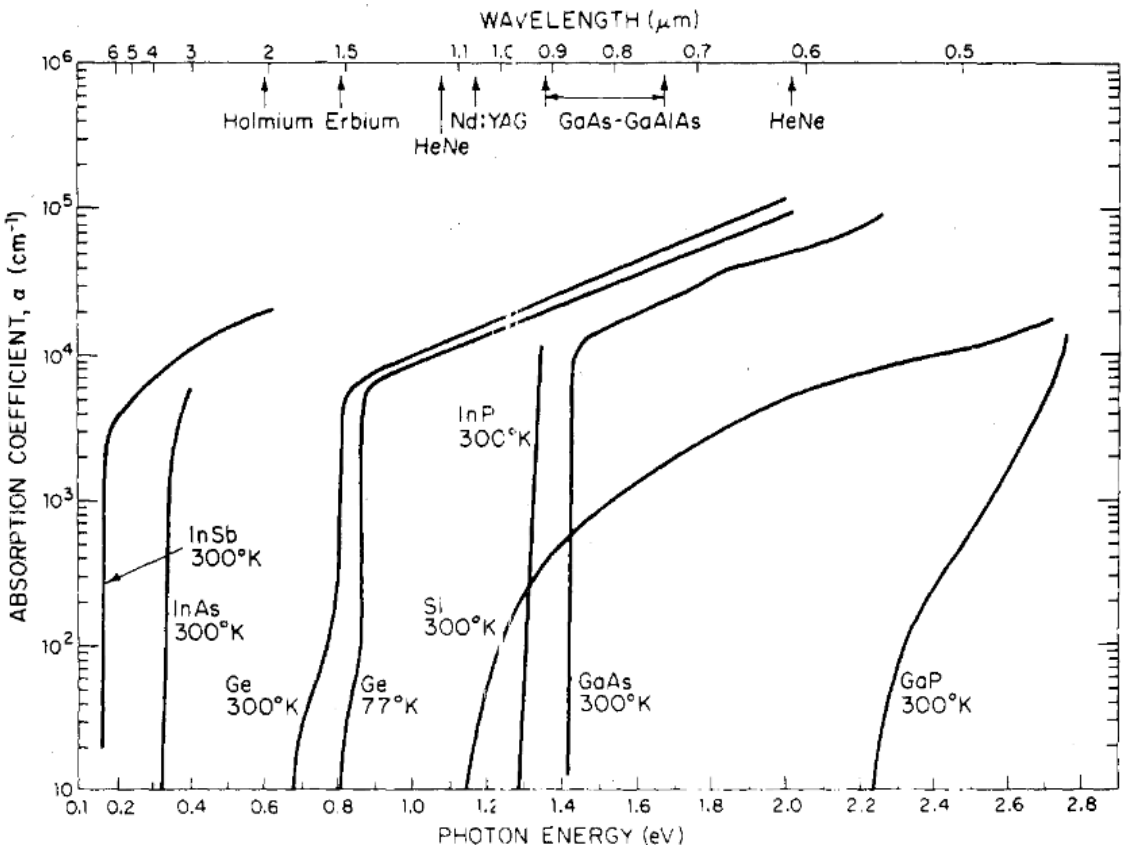

Figure 6.1: Absorption coefficient for various semiconductor materials. (Plot from [12])

As with most semiconductors and their alloys, the valence band maximum of germanium is located at the gamma point in the Brillouin Zone. The conduction band minimum for germanium is located at the L point for the conventional FCC lattice structure and is 140meV less than the direct gap energy [137]. This relatively small difference has been the motivation for band structure research and engineering to achieve a direct-gap form of the material for use in optical devices. The most promising techniques applied to achieve such a structure include applying strain and alloying with various other elements [138]. The obvious choice of alloy material has been tin due to its location in the period immediately below germanium. The alpha allotrope variant of tin has the same diamond crystal structure as germanium but acts like a semimetal with a negative band gap at the gamma point [138]. An elementary application of the simple linear form of Vegards law gives the indication that the transition from direct to indirect gap should occur at approximately a 21% uniform tin concentration [139]. Experimental and calculated results both show the presence of a bowing parameter which is needed to fit the non-linear experimental data for how the band gaps change with varying tin concentration [140]. In general, it is known that with increasing Sn concentration, both the direct and indirect gaps of $Ge_{1-x}Sn_x$ shrink but the direct gap does so at a faster rate. If the exact concentration of Sn needed to cause this transition can be determined, direct gap devices can be fabricated while still maintaining as much of the gap as possible.

6.2 DFT-Based Analysis of Ge

Band structure calculations in the past have predominately been performed using single-electron empirical pseudopotential methods with extrapolation to fit data to GeSn alloys [141]. We have performed calculations for specific compositional percentages of GeSn using Density-Functional Theory (DFT). Figure 6.2 shows the cells on which we have used to perform calculations, containing 12.5%, 6.25%, and 3.125% Sn. These cells were constructed using repeated 8 atom cubic unit cells.

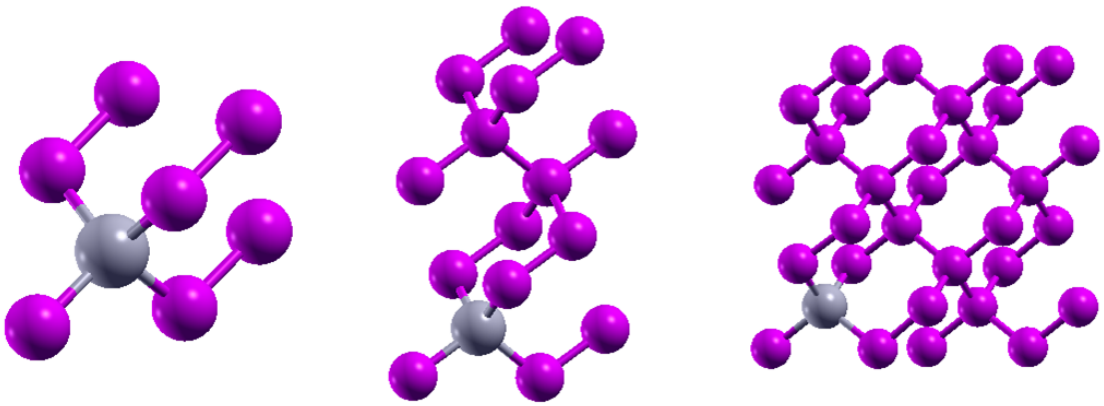

Figure 6.2: Atomic supercells of $Ge_{1-x}Sn_x$ used in DFT calculations for 12.5%, 6.25%, 3.125% Sn

Before we calculate the predicted band structure of the alloys however, we first needed to reproduce the experimentally known results of a pure Ge crystal. To do this we must chose not only an appropriate functional and pseudopotential, but also ensure the calculation results are converged with respect to the numerical discretization built in to the code. The accuracy of DFT results are highly dependent on the combination of the system being studied, the pseudopotential used, and the functional applied to the calculation [142]. Pseudopotentials act as an effective ionic

potential that each valence electron interacts with, and acts to stabilize calculations by treating sharp core potential as a smoother approximation within some defined radius. In doing this the high frequency components of core wavefunctions are supressed while leaving the electrically and chemically-important valence portion unchanged. By making this approximation, larger systems of atoms become solvable by reducing the number of plane waves needed in the wavefunction expansion within calculation. Different methods exist for generating pseudopotentials and accuracy is generally dependent on the configuration of the system being studied. After testing numerous pseudopotentials generated using different functionals and valence occupancies, we were able to use a pseudopotential generated using the Perdew-Burke-Ernzerhof (PBE) functional to obtain an accurate band structure of pure germanium crystal. The self-consistent calculation was performed using the hybrid PBE0 functional which allowed us to correct the indirect and direct bandgap energies to their experimental values by applying the appropriate mixing fraction of exact Hartree-Fock exchange energy. Calculations in DFT transform the set of Kohn-Sham equations for non-interacting particles by expanding the potentials and wave functions onto a finite basis of plane waves, the highest energy of which is set by a cutoff energy threshold. By adjusting this cutoff energy the number of plane waves in the expansion can be adjusted. There basis set should be sufficiently large to ensure good representation of the wave functions but this increase comes at the cost of increased computation time and memory usage. In addition to requiring a sufficient cutoff energy, calculations also should be performed at enough k points to adequately sample the BZ. During the calculation, integrals over the entire BZ

are needed to calculate the charge density at each iteration. This integration is approximated by taking a weighted sum over a finite set of special points in the irreducible wedge of the BZ with weights corresponding to the number of equivalent points in the entire BZ [143]. The BZ of Ge is the same truncated octahedron as that of Si, shown in Figure 6.3.

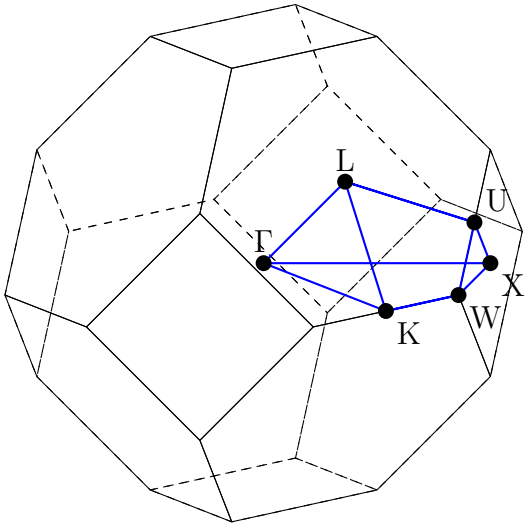

Figure 6.3: Brillouin Zone of an FCC lattice.

In addition to increasing the cutoff energy, increasing the number of k points increases the computation time. Ideally, we would use the Monkhorst-Pack k point grid as a way to select points in an unbiased manner and perform a relatively computation-heavy self-consistent field (SCF) calculation to obtain an accurate representation of the system potential. This potential can then be used as an input to an inexpensive non-self-consistent field (NSCF) calculation with k points selected along the path of the high symmetry points of the desired band structure plot. Unfortunately, Quantum Espresso does not support the ability to perform NSCF calculations using hybrid functionals, so our calculations had to be performed with

the desired k point path directly in the SCF calculations. To minimize integration errors, we used a long path length as well as a high k point density to attempt to cover the majority of the irreducible wedge.

While trying to tune the parameters used to obtain the experimental band gaps for the pure Ge crystal cell, we noticed that both the direct and indirect gap energies varied linearly with the mixing fraction as shown in Figure 6.4.

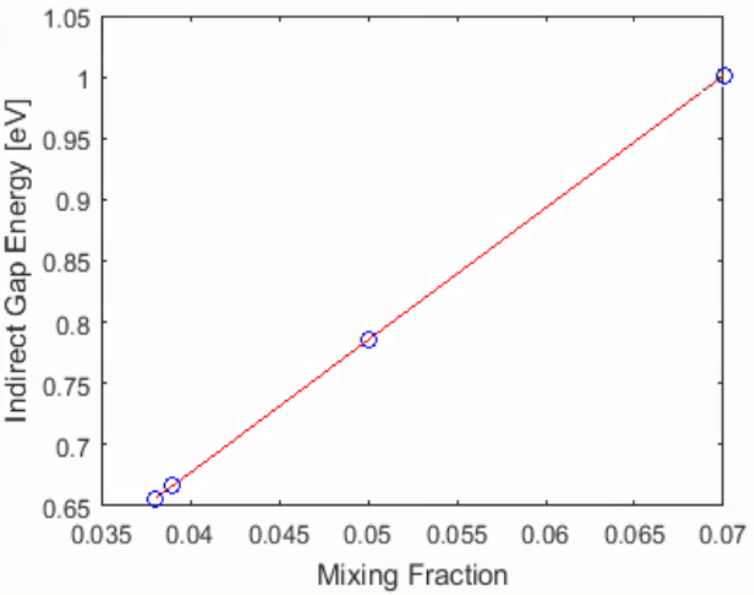

Figure 6.4: Indirect gap energy at the L point varying linearly with hybrid functional (PBE0) mixing fraction

The lattice constants of materials are not reliably reproducible with DFT in general, and the degree of error changes with both material and functional used. More specifically, the PBE functional used in this work is known to regularly overestimate the lattice constant in solids by up to 2% [144]. According to the results by [142], the lattice constant of Ge is overestimated by about 1.9% for the PBE functional. We started with calculating the band structure from the experimentally reported lattice constant of 5.646Å and then performed calculations for other

slightly deviated lattice parameters. By adjusting the lattice constant of the cell we effectively apply a hydraulic strain to the crystal. Figure 6.5 shows the resulting plot of the energy gap difference with respect to lattice constant which exhibits a linear relationship. We adjust the lattice constant to give the experimental gap difference of 140meV resulting in a lattice constant 1.3% strained from the experimental value of 5.646Å [138].

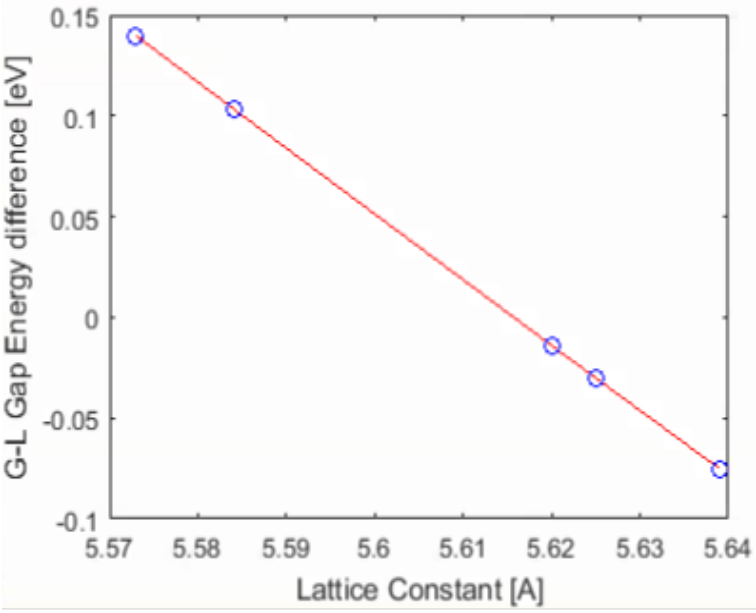

Figure 6.5: Gap Difference (E_Γ-E_L) varying linearly with lattice constant. Literature: 5.646Å Our Work: 5.573Å (1.3% difference)

The final band structure obtained of the pure germanium crystal is shown in Figure 6.6, with an indirect gap of 0.66eV and a direct gap of 0.80eV achieved using a lattice constant of 5.573Å. Our calculation was able to produce a band structure which matched the gap energies reported in literature [8] for the lowest direct and indirect valleys, with the rest of the valleys in moderately good agreement. The band structure diagram from literature is given in Figure 6.7 and a comparison of the gap

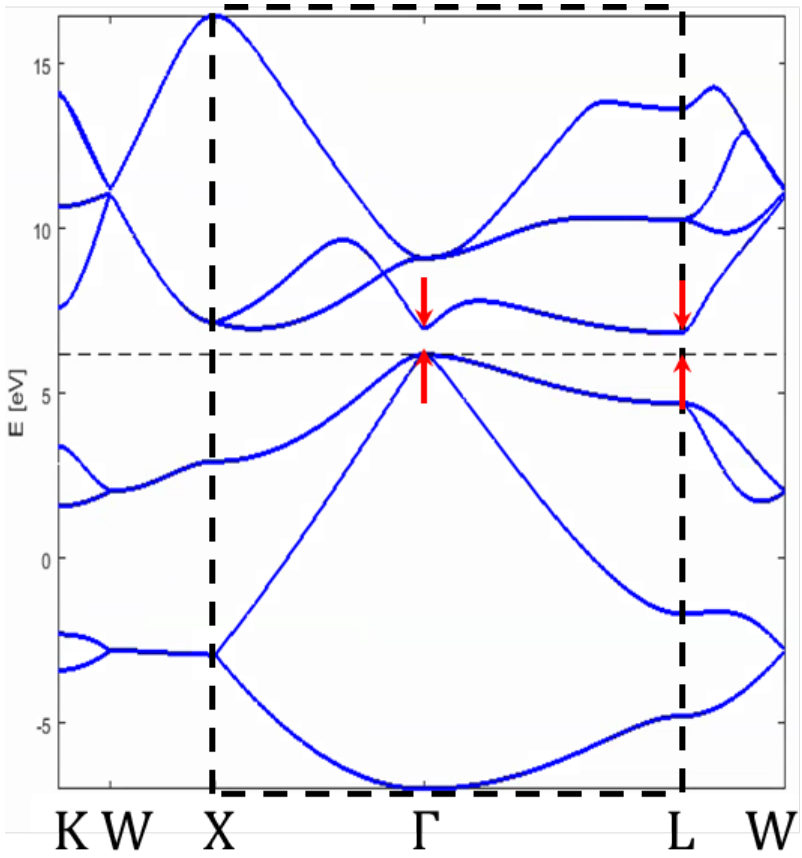

Figure 6.6: DFT calculated Ge band structure for 2 atom cell using the PBE0 hybrid functional. Dashed box shows the same section of the band structure given in the literature [8]. The key direct and indirect gaps are shown with red arrows.

energies in Table 6.1. This calculation was performed on a simple 2 atom cell with an FCC Bravais lattice and the results give confidence in using this pseudopotential

Table 6.1: Comparison of calculated energy gap values of Ge to those found in the literature.

Gap [eV]	**Calc.**	**Lit.** [8]
E_g (E_L)	0.659	0.66
$E_{\Gamma 1}$	0.799	0.8
ΔE	0.788	0.86
E_X	0.977	1.2
$E_{\Gamma 2}$	2.926	3.22
E_{so}	$\approx$0	0.29

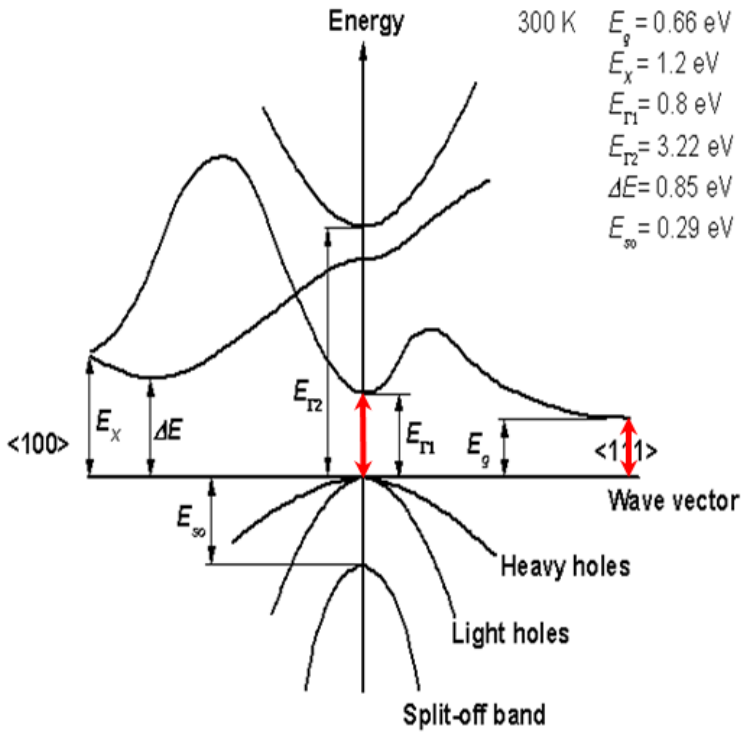

Figure 6.7: Ge band structure from [8]. The key direct and indirect gaps are shown with red arrows.

and functional for further, larger calculations on GeSn alloys.

6.3 DFT-Based Analysis of GeSn Alloys

To generate supercells with variable percentage of tin, we change the cell from an FCC Bravais lattice with a 2 atom basis to a simple cubic lattice with an 8 atom basis or a tetragonal lattice with a 16 or 32 atom basis, each with a single tin atom. As with the 2 atom cell, we tune the lattice constant and mixing fraction of an 8 atom cell which can be repeated to generate the other cells. The mixing fraction used to tune the gap values of the pure germanium 8 atom cell will be kept constant when tin is added and when the larger cells with tin are used.

Performing computations using larger supercells comes with the cost of signifi-

cantly increased computation time. The Virtual Crystal Approximation (VCA) is a work-around to this problem, wherein the characteristics from the pseudopotentials of both Ge and Sn are merged into a hybrid pseudopotential representing a non-existent atom which approximates a percent concentration of each atom, allowing for small atomic cells but introducing non-physical atoms [139, 141]. Because of the potentially limiting transferability inherent to certain kinds of pseudopotentials, care must be taken to ensure that pseudopotentials maintain accuracy. The effects of these approximations are evident in published results on the subject, where the various transition percentage predictions range greatly from 6-21% or more depending on the method used [138]. With access to the High-Performance Computing Cluster Deepthought2 at the University of Maryland, the computationally expensive, large supercell DFT calculations can be run massively parallelized with Quantum ESPRESSO [30] to obtain accurate band structures for different cell sizes and fractions of Sn. We believe that performing these ab initio calculations provides us more accurate information about the band structure of the system than is obtained using the VCA.

Calculation time is system dependent and increases greatly with an increase in the number of k points used, the number of bands in the calculation, and the number of plane waves. As an approximation, the time to complete a calculation increases proportional to the number of atoms per unit cell and is given by Equation 6.3 [143].

$$T_{cpu} \sim N_{iter} N_k \times (O(N_b N_{pw}^2) + O(N_b N_{pw} \log N_{pw}) + O(N_b^2 N_{pw})) \tag{6.3}$$

Where N_{iter} is the number of iterations required to achieve self-consistency, Nk is the number of k points specified, Nb is the number of bands, and Npw is the number of plane waves in the expansion. The number of k points required to achieve convergence generally decreases with an increase in the supercell size because of the inverse size relationship of real-space and reciprocal-space. In contrast, the number of bands required will increase as it is calculated by taking the number of atoms in the supercell and multiplying by the number of valence electrons per atom. The number of plane waves required to achieve convergence will also generally increase with an increasing supercell size. The number of iterations to achieve self-consistency is more difficult to predict but can be assumed to fall within 5 to 20. To complete calculations in a reasonable amount of time due to this highly-nonlinear time scaling, we use the multiple parallelization levels available in the Quantum Espresso PWscf program. Quantum Espresso is set up with different levels of parallelism forming a hierarchical structure. The top level divides the processors into pools, each of which takes care of the calculation at a group of k points. The next level, known as plane wave parallelization, distributes the wave function coefficients across the processors in each pool of plane wave processors, offering one of the biggest calculation speedups. Once the speedup for this level saturates, the final level of parallelization can extend the processor scaling. This level divides each group of plane wave processors in to task groups, each which perform the calculation on a group of electronic states. The plane wave groups can also be partitioned into linear algebra groups which parallelize diagonalization and matrix multiplication by distributing across groups of a square number of processors [143].

Through various trials we have been able to find optimal distributions of processors for each parallelization level and bring calculation times down significantly. For the two atom cell using hybrid functional DFT with 1500 k points and a cutoff energy of 100Ry, the calculation time was able to be reduced from multiple hours in a serial hybrid functional calculation to under 5 minutes in parallel using 144 processors. Similarly to the two atom cell, the 8, 16, and 32 atom cell calculations were parallelized to reduce their computation time while maintaining accuracy with respect to cutoff energy and number of k points. The band structures were obtained from these calculations and the direct and indirect gap energies were extracted for the various compositional percentages of the germanium-tin alloy. Plotting these energies, we extract the Sn percentage needed to transition from an indirect to a direct gap material shown in Figure 6.8. The transition at 8.5% tin is in agreement within the range predicted by various other methods [138] but we believe this value to be close to the true value.

In performing these calculations, we have ensured their convergence by increasing the number of k points and the cutoff energy used until the total energy of each system studied varied less than 0.01 Ry. The systems studied were representative of uniformly distributed tin in a GeSn crystal which we take to approximate a real world uniform distribution. From these calculations, we obtained the band structure for different compositional percentages of Sn and have extracted their various direct and indirect gap energies. By plotting these, we found the crossing point which indicates the transition from an indirect gap to occur at 8.5% Sn. At this

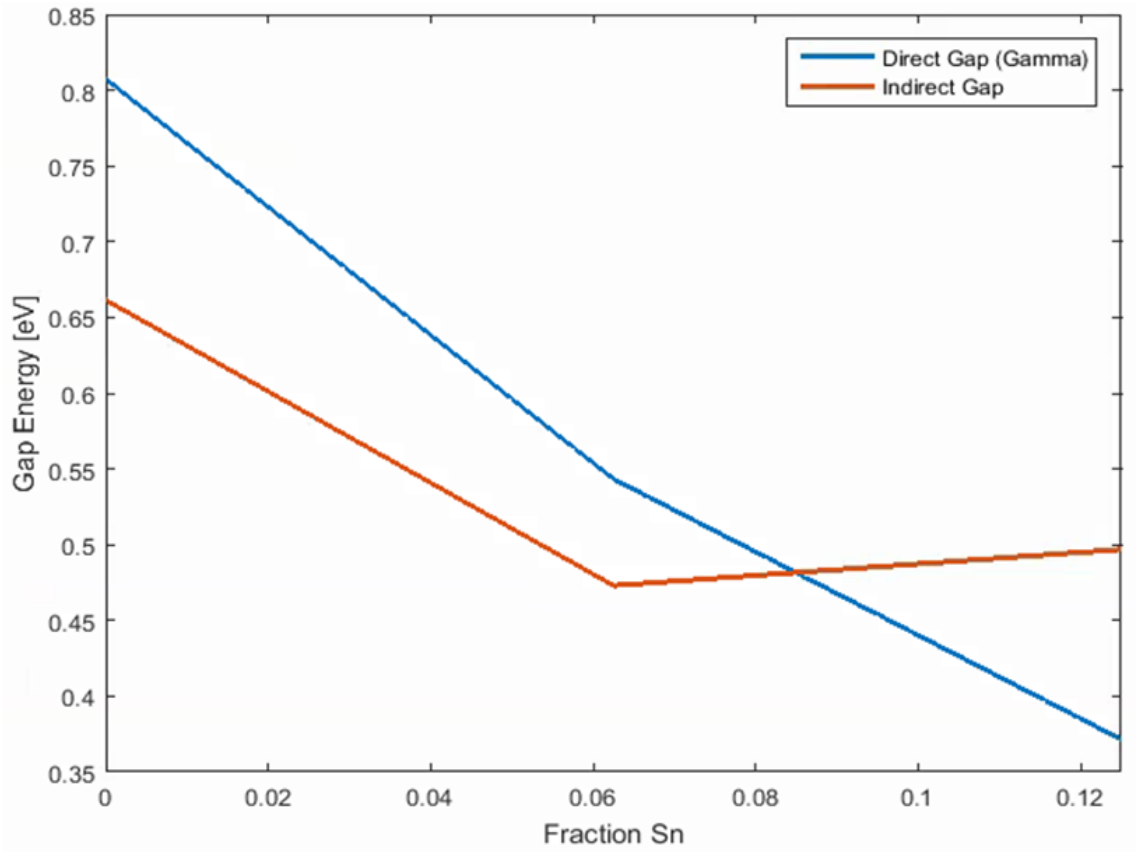

Figure 6.8: E_Γ and E_L calculated for different fractions of Sn

Sn concentration, and presumably all percentages higher than this, the material has undergone the transition into a direct gap material. By manufacturing the alloy directly at this transition percent, the band structure will be direct but will also have the added benefit of maintaining as much of the initial gap value as possible. This improvement will allow for optical Ge devices to be manufactured with greater quantum efficiency.

Appendix A: DFT Evolution and History

A.1 Hartree-Fock Method

Fock's extension of Hartree's theory, the Hartree-Fock method, attempts to solve the quantum many-body problem by first assuming that the total wavefunction can be approximated by a single Slater determinant. Electrons are treated as moving in an external potential from the ions plus a mean field formed by the other electrons in the system. Via application of the variational principle, a set of N-coupled equations of the form Eqn. A.1 can be derived and solved iteratively to produce the approximate orbitals. The effects of electron correlation (interaction of opposite spin electrons) are neglected in this formulation which results in a systematic error. However, the exchange effects of electrons with like-spin are accounted for in this theory.

$$\left(-\frac{1}{2}\nabla^2 + V_{ext}(\mathbf{r}) + \sum_{j\neq i}^{N}\int \frac{|\psi_j(\mathbf{r'})|^2}{|\mathbf{r}-\mathbf{r'}|}d\mathbf{r'}\right)\psi_i(\mathbf{r}) - \sum_{j\neq i}^{N}\int \frac{\psi_i(\mathbf{r'})\psi_j^*(\mathbf{r'})\psi_j(\mathbf{r})}{|\mathbf{r}-\mathbf{r'}|}d\mathbf{r'} = \epsilon_i\psi_i(\mathbf{r}) \tag{A.1}$$

In this formulation, a trial wavefunction is taken as an initial guess. Due to the variational theorem, the energy expectation of the system taken using the trial wavefunction will be greater than the energy of the true ground state of the system.

The energy is obtained by taking the expectation of the Hartree-Fock Hamiltonion with the Slater determinant total wavefunction, resulting in Equation A.2.

$$E^{HF} = -\frac{1}{2}\sum_{j=1}\int \phi_j^*(\mathbf{r})\nabla^2\phi_j(\mathbf{r})d\mathbf{r} + \frac{1}{2}\sum_{j=1,i=1}\int \frac{\phi_j^*(\mathbf{r})\phi_i^*(\mathbf{r'})\phi_j(\mathbf{r})\phi_i(\mathbf{r'})}{|\mathbf{r}-\mathbf{r'}|}d\mathbf{r}d\mathbf{r'} \quad \text{(A.2)}$$
$$-\frac{1}{2}\sum_{j=1,i=1}\int \frac{\phi_j^*(\mathbf{r})\phi_i^*(\mathbf{r'})\phi_i(\mathbf{r})\phi_j(\mathbf{r'})}{|\mathbf{r}-\mathbf{r'}|}d\mathbf{r}d\mathbf{r'} + \sum_{j=1}\int \phi_j^*(\mathbf{r})\phi_j(\mathbf{r})V_{ext}(\mathbf{r})d\mathbf{r}$$

Though this technique proved to be an improvement over solving the original many-body Schrdinger equation, there was still need for a practical application of the SCF technique due to the complexity still associated with the number of electrons.

A.2 Thomas-Fermi Model

In 1927 Thomas and Fermi created the first model for a quantum electronic system based purely on the electron density. With this model, instead of solving for the N wavefunctions of an N-electron system self-consistently, the problem was reduced to a function of only the 3 spatial dimensions of the density. Though initially formulated to apply to single atoms, the theory was later also applied to molecules, crystals and metals [145]. The simplified problem under this formulation allows solutions to be directly obtained from its variational Euler equation.

In their assumptions they consider an electron gas which satisfies Fermi statistics where electron-electron and electron-nucleus interactions are treated classically as purely Coulombic in nature. The kinetic energy contribution at each point in the system is determined by using the exact kinetic energy of a homogeneous electron gas with density equal to the value at that point, making this a local density approximation [31]. This kinetic energy per volume is then integrated over the entire

system to yield total kinetic energy, shown in equation A.3.

$$T[n(\mathbf{r})] = \frac{3}{5}\frac{\hbar^2}{2m_e}\left(3\pi^2\right)^{\frac{2}{3}}\int [n(\mathbf{r})]^{5/3} d^3r \tag{A.3}$$

The potential energy terms used in the Thomas-Fermi (TF) model are shown below in Equation (A.4). From the symmetric form of the electron-electron repulsion term we can see that despite double counting being accounted for by the $\frac{1}{2}$ term, there exists a self-interaction energy which is erroneously included.

$$\begin{aligned} U_{e-N} &= \int n(\mathbf{r}) V_N(\mathbf{r}) d^3r \\ V_N(\mathbf{r}) &= -\sum_{j=1}^{M} \frac{Z_j e^2}{|\mathbf{r} - \mathbf{R}_j|} \\ U_{e-e} &= \frac{1}{2} e^2 \int \frac{n(\mathbf{r}) n(\mathbf{r'})}{|\mathbf{r} - \mathbf{r'}|} d^3r d^3r' \end{aligned} \tag{A.4}$$

Furthermore, the TF model originally did not account for electron exchange energy which is required to obey the Pauli exclusion principle nor does it account for the effects of electron correlation. A correction to approximate exchange energy derived from a homogeneous electron gas model was eventually added by Dirac in 1930 [31].

Due mainly to the simplistic kinetic energy approximation and in part to the other approximations, the total energy functional given by the TF model (Eqn. (A.5)) ends up being quite inaccurate and predicts the total energy of a bonded system to be larger than its constituent parts, making molecules unstable [145]. This is obviously a serious issue and a poor result in most situations so other more

sophisticated theories were later developed.

$$E^{TF}[n(\mathbf{r})] = T[n] + E_{e-N}[n] + E_{e-e}[n] \tag{A.5}$$

$$E^{TF}[n(\mathbf{r})] = \frac{3h^2}{10m_e}\left(\frac{3}{8\pi}\right)^{\frac{2}{3}}\int [n(\mathbf{r})]^{5/3}d^3r + \int n(\mathbf{r})V_N(\mathbf{r})d^3r + \frac{1}{2}e^2\int\int \frac{n(\mathbf{r})n(\mathbf{r'})}{|\mathbf{r}-\mathbf{r'}|}d^3rd^3r'$$

Thomas-Fermi existed as a predecessor to DFT by creating approximate energy functionals of the electron density in an attempt to simplify the quantum many-body problem without the mathematical rigor and justification which came later from the work of Hohenberg and Kohn. This later work showed that a functional approach could be made to reproduce the exact energies of the system instead of mere approximations [146].

A.3 Hohenberg-Kohn Theory

In their revolutionary 1964 paper [147], Hohenberg and Kohn developed a theorem forging the groundwork for DFT. Their proofs gave deep insight to the quantum many-body problem and to potential solution techniques. First, they proved that there is a one-to-one mapping between the external ionic potential $V_{ext}(\mathbf{r})$ and the ground state density, as well as a one-to-one between the ground state density and the total wavefunction (Eqn. A.6). This property allows us to determine the potential from the density, from which we can construct a Hamiltonian. Since the Hamiltonian tells us everything about the system including the wavefunction solutions, the density determines all states of the system [31]. Their second proof shows that there exists a universal kinetic+interaction functional of the density $F[n(\mathbf{r})]$ (applying systems with any $V_{ext}(\mathbf{r})$) which obeys a variational principle.

This functional differs from the total ground state energy functional by the external ionic potential energy as shown in Equation A.7.

$$n(\mathbf{r}) = N \int \Psi^*(\mathbf{r}, \mathbf{r}_2, \ldots, \mathbf{r}_N)\Psi(\mathbf{r}, \mathbf{r}_2, \ldots, \mathbf{r}_N) d\mathbf{r}_2 \cdots d\mathbf{r}_N \tag{A.6}$$

$$E^{HK}[n(\mathbf{r}), V_{ext}(\mathbf{r})] = \int V_{ext}(\mathbf{r}) n(\mathbf{r}) d\mathbf{r} + F[n(\mathbf{r})] \tag{A.7}$$

$$E^{HK}_{GS}[n(\mathbf{r})] = \min_{n(\mathbf{r})} E^{HK}[n, V_{ext}]$$

$$N = \int n(\mathbf{r}) d\mathbf{r} \tag{A.8}$$

Because this functional obeys a variational principle, it enables us to hunt for densities which minimize this functional under the constraint that the density integrates total number of electrons in the system (Eqn. A.8). The configuration which minimizes the energy functional must then be the ground state density from which we can determine everything about the system using the first proof. By following this process, the problem is drastically simplified due to the reduction in dimensionality. Instead of searching for an unfathomably high dimensional wavefunction, we can simply work with the density, a function of only 3 spatial dimensions.

Though this theory lays the groundwork for greatly simplifying the problem, it unfortunately does not give any insight into form of the universal functional. Further theories go on to approximate the functional in various forms and generally use equations with clear physical origins which are relatively simple to evaluate. Other methods solve the problem self-consistently by recasting the problem from an energy

minimization into a Schrödinger-like equation which must be solved consistently such as in Kohn-Sham DFT.

Appendix B: Semiconductor Physics

B.1 Low Doping Limit of Hole Concentration

The following derivation reiterates the assumptions made to compute the hole concentration in the low-doping limit of non-compensated semiconductor which were presented in Section 4.2. This result is used in the derivation of the conductivity mobility parameterization in Section B.1.1.

To begin, charge neutrality is used to compute the hole concentration. For the system considered, it is assumed that there is no significant donor counter doping. Additionally, because intrinsic carrier concentration is so small in 4H-SiC, n_i is neglected. The resulting charge neutrality equation states that the hole concentration must equal the ionized acceptor concentration $p = N_A^-$. In general, both of these terms are functions of the unknown Fermi-level E_F, as is shown in Section 4.6. In the low doping limit, however, the governing equations can be manipulated using some approximations which allow us to remove E_F as an independent unknown variable and provide a closed-form analytical solution.

In the case of low doping, the Fermi level is within the bandgap far from the valence band edge so the tail of the true Fermi-Dirac occupancy function for holes is well approximated by the Maxwell-Boltzmann distribution. We apply this

approximation to the full integral in Equation B.1 which results in Equation B.2.

$$p = \frac{4\pi(2m_p^*)^{3/2}}{h^3} \int_{-\infty}^{E_V} \frac{\sqrt{E_V - E}}{1 + \exp\left(\frac{E_F - E}{k_B T}\right)} dE \tag{B.1}$$

$$p \approx \frac{4\pi(2m_p^*)^{3/2}}{h^3} \int_{-\infty}^{E_V} \sqrt{E_V - E} \exp\left(\frac{E - E_F}{k_B T}\right) dE \tag{B.2}$$

Equation B.2 has an exact solution which can be written as:

$$p \approx N_V \exp\left(\frac{E_V - E_F}{k_B T}\right) \tag{B.3}$$

$$N_V = 2\left(\frac{2\pi m_p^* k_B T}{h^2}\right)^{(3/2)} \tag{B.4}$$

Where N_V is the effective density of states in the valence band which depends on the hole effective mass m_p^* and the temperature T. Next, we create and evaluate the integral for the ionized acceptor density N_A^- using the modified Fermi-Dirac statistics by including the acceptor state degeneracy g_A. For low doped samples, dopant atoms are far apart and thus all impurity states introduced have virtually the same energy (assuming small or no inequivalent site energy-dependence). This creates a density of impurity states in the form of a delta-function at the ionization energy E_A i.e. $\rho_i(E) = N_A \delta(E - E_A)$.

$$N_A^- = \int_{-\infty}^{\infty} \frac{N_A \delta(E - E_A)}{1 + g_A \exp\left(\frac{E - E_F}{k_B T}\right)} dE \tag{B.5}$$

$$N_A^- = \frac{N_A}{1 + g_A \exp\left(\frac{E_A - E_F}{k_B T}\right)} \tag{B.6}$$

Finally, we can rewrite Equation B.6 in terms of the hole concentration given in Equation B.3, leaving us with a quadratic equation for the solution of the hole concentration p.

$$N_A^- = \frac{N_A}{1 + g_A \exp\left(\frac{E_V - E_F}{k_B T}\right) \exp\left(\frac{E_A - E_V}{k_B T}\right)} \tag{B.7}$$

$$N_A^- = p = \frac{N_A}{1 + \frac{g_A p}{N_V} \exp\left(\frac{E_A - E_V}{k_B T}\right)} \tag{B.8}$$

$$p = \frac{N_A}{1 + \frac{p}{2\gamma}} \tag{B.9}$$

$$p = -\gamma + \sqrt{\gamma^2 + 2\gamma N_A} \tag{B.10}$$

$$\gamma = \frac{N_V}{2g_A} \exp\left(-\frac{\Delta E_A}{k_B T}\right) \tag{B.11}$$

$$\Delta E_A = E_A - E_V \tag{B.12}$$

Here, γ is an auxiliary variable of known physical parameters, N_A is the acceptor doping density, N_V is the valence band effective density of states, ΔE_A is the acceptor ionization energy, and g_A is the acceptor state degeneracy equal to 4 in 4H-SiC.

B.1.1 Conductivity Mobility Parameterization

To develop a semi-empirical expression which parameterizes this work's definition of conductivity mobility (Equation B.13) we need to create an expression to

represent the resistivity term, as it is the only unknown parameter.

$$\mu_{Cond} \equiv \frac{1}{q\rho N_A} \tag{B.13}$$

Using the standard expression for resistivity (Equation B.14), the two unknowns are now the hole concentration p and the hole mobility μ_p.

$$\rho = \frac{1}{qp\mu_p} \tag{B.14}$$

The hole mobility μ_p is taken to have the same form as the Hall mobility $\mu_p = \mu_{Cond0}/(1+(N_A/N_C)^c)$ and p is calculated using the solution to the low doping charge neutrality equation of the form $p = -\gamma + \sqrt{\gamma^2 + 2\gamma N_A}$ calculated in Section 4.2. This expression is then substituted for ρ into the definition of conductivity mobility (Eq. B.13). This provides the first part of our empirical conductivity mobility in Equation 4.60. An additional impurity mobility term is then added which has the form of a Gaussian because of the approximate shape of the observed resistivity data for large N_A.

B.2 Modified Fermi-Dirac for Dopant States

To calculate the number of ionized acceptor states, we must multiply the acceptor impurity density of states $\rho_i(E)$ by the probability of electron occupancy of said states. The statistical occupation function is essentially a Fermi-Dirac distribution, except there is a degeneracy factor which appears because impurity states can only be singly charged as the acceptor may only accept one electron and a donor can

only loose one electron due to the large Coulombic energy associated with double ionization.

For an acceptor, the gained electron can either be spin up or spin down without changing the energy of the system (to a good approximation), which creates two degenerate configurations. Additionally, since we are dealing with acceptor states, the 'accepted' electron is coming from the valence band maximum located at the Γ-point, where there is a degeneracy of the light-hole and heavy-hole bands in SiC. This additional degeneracy multiples the previous degeneracy, leading to a 4-fold degeneracy which should be included into the Fermi-Dirac function for acceptor state occupancy.

As a starting point, the mathematical derivation using the micro-canonical ensemble for the standard Fermi-Dirac proceeds as follows:

Thermodynamics states that the most likely configuration for a system will be the macrostate with the largest number of microstates. First we will enumerate the total number of microstates of the system, then using Lagrange multipliers, we will apply the constraints of total particle number and total energy to find the occupancy function which defines this macrostate.

At each energy E_i, we want to fill the n_i degenerate states with m_i electrons where $0 \leq m_i \leq n_i$. We can represent the number of electrons in each state using an occupancy function f_i (a fraction < 1) which multiplies the n_i states $m_i = f_i n_i$. Here, f_i represents the probability of occupying $f_i n_i$ states at energy E_i.

To determine f_i, we first enumerate the number of ways these states and electrons can be arranged - knowing that each state can only hold one electron. The

number of distinct configurations C_i for each energy E_i is calculated by dividing the number of ways to rearrange all of the states, by the number of ways to rearrange the filled states, and by the number of ways to rearrange the empty states. This is equivalent to enumerating the number of ways to fill n_i states with m_i electrons:

$$C_i = \frac{n_i!}{m_i!(n_i - m_i)!} = \frac{n_i!}{(f_i n_i)!(n_i - f_i n_i)!} \tag{B.15}$$

Because the electrons and the states at a given energy are indistinguishable amongst themselves, the two factorial terms appear in the denominator. To find the most likely distribution of f across all energy states, we must multiply the number of configurations at each energy to get the total number of configurations or microstates for the entire system. Then, to obtain a more tractable solution, we apply Sterling's approximation $\ln(n!) \sim n\ln(n) - n$ which is valid due to the large number of electrons and states.

$$C = \prod_i C_i = \prod_i \frac{n_i!}{(f_i n_i)!(n_i - f_i n_i)!} \tag{B.16}$$

$$ln(C) = \sum_i \ln C_i = \tag{B.17}$$

$$\sum_i \left(n_i \ln(n_i) - (f_i n_i)\ln(f_i n_i) - (n_i - f_i n_i)\ln(n_i - f_i n_i)\right)$$

The system is also constrained by the total number of electrons N and the total energy U defined by:

$$N = \sum_i f_i n_i \tag{B.18}$$

$$U = \sum_i E_i f_i n_i \tag{B.19}$$

Finally we can determine the distribution f that maximizes the number of configurations, which thermodynamics ensures will be the most probable distribution in thermal equilibrium. To do this, we maximize the configuration function C (or $\ln(C)$) subject to our constraint equations using the method of Lagrange multipliers.

$$\frac{\partial}{\partial f_i}\left[\ln(C) - a\sum_j f_j n_j - b\sum_j E_j f_j n_j\right] = 0 \tag{B.20}$$

$$\ln\left(\frac{1-f_i}{f_i}\right) - a - bE_i = 0 \tag{B.21}$$

$$f_i = \frac{1}{1+\exp(a+bE_i)} \tag{B.22}$$

Further analysis of the units in the variational equation and relating the variational energy term to the change in energy due to the change in entropy allows us to notice that b must be $1/k_B T$ to satisfy $dU = \frac{1}{b}d(\ln(C)) = Td(k_B \ln(C)) = TdS$ from thermodynamics. Analogously it can be shown that a must be $-E_F/kT$ from $(-a/b)dN = \mu dN$, where E_F is called the Fermi energy and μ is the electro-chemical potential of the system. Finally, we rewrite our distribution function, known as the Fermi-Dirac distribution:

$$F(E) = \frac{1}{1+\exp\left(\frac{E-E_F}{k_B T}\right)} \tag{B.23}$$

This equation is valid for the occupancy of Fermions (namely electrons) which have only **one** way to occupy a state - such as in the conduction band of SiC and other semiconductors. Because the density of states used in conjunction with this formula already accounts for (i.e. 'labels') states with 'up' and 'down' spin, conduction band (and valence band) states can only be unoccupied or singly occupied and the spin of the electron is tied to the state. When determining the distribution function for acceptor or donor state occupancy, there are different ways in which the state may be occupied. These extra ways of occupying the state lead to a degeneracy (depending on how many extra ways) which must be included in the distribution formulation. The density of states associated with a doped impurity does not have spin association built in to it's states. For example, in the case of donors, a single doping level at E_D may have a Gaussian density of states $g_i(E)$ centered around E_D which integrates to the donor concentration N_D. With this density of states, each state is either singly occupied with either a spin-up or spin-down electron (independent of how every other state is occupied) or singly ionized with no electron present. Each state is not 'labeled' as a 'spin-up' or 'spin-down' state beforehand as is the case with the conduction band and valence band density of states via the factor of 2 included for spin in their values. Therefore each electron occupying a donor state may do so in **two** ways: with either spin 'up' and with spin 'down'. This choice manifests itself in increasing the total number of possible ways to fill the n_i donor states with the m_i donor electrons. The total number of ways to assign the states is thus doubled for each of the m_i electrons which occupy the donor states due to the choice of each being filled with a spin 'up' or spin 'down' electron. Any

electron chosen to not occupy a donor state will instead occupy a conduction band state. The total number of electrons in the system is limited-by and equal-to the total donor concentration.

So, for electrons occupying donor states:

$$C_i = \frac{2^{m_i} n_i!}{m_i!(n_i - m_i)!} = \frac{2^{f_i n_i} n_i!}{(f_i n_i)!(n - f_i n_i)!} \tag{B.24}$$

Carrying out the same derivation leads to the equation:

$$\ln\left(2 \cdot \frac{1 - f_i}{f_i}\right) - a - bE_i = 0 \tag{B.25}$$

which results in a modified Fermi-Dirac function to represent the probability of occupancy of donor states:

$$F_D(E) = \frac{1}{1 + \frac{1}{2}\exp\left(\frac{E - E_F}{k_B T}\right)} \tag{B.26}$$

This occupancy function can be used directly with the donor density of states to calculate the **unionized** donor concentration N_D^0 (i.e. number of donor states which are still are occupied by electrons). To calculate the often more useful **ionized** donor concentration N_D^+ we must use $1 - F_D(E)$:

$$1 - F_D(E) = \frac{1}{1 + 2\exp\left(\frac{E_F - E}{k_B T}\right)} \tag{B.27}$$

Similarly, for acceptors, there are two choices to make when filling each acceptor state with a hole. The electrons still in the valence band may not only be spin 'up' or spin 'down' but also may be residing in the heavy-hole or a light-hole band.

This effect occurs due to the light-hole/heavy-hole valence band degeneracy at the gamma point which is common among many semiconductors (including SiC). These choices multiply the number of ways to choose and fill m_i of n_i acceptor states with electrons by 4 for each of the $n_i - m_i$ holes:

$$C_i = \frac{4^{n_i - m_i} n_i!}{m_i!(n_i - m_i)!} = \frac{4^{n_i - f_i n_i} n_i!}{(f_i n_i)!(n - f_i n_i)!} \tag{B.28}$$

resulting in the modified Fermi-Dirac function for the electron occupancy of acceptor states for calculating N_A^-:

$$F_A(E) = \frac{1}{1 + 4\exp\left(\frac{E - E_F}{k_B T}\right)} \tag{B.29}$$

B.3 Valence Band Density of States

To derive the density of states in the valence band, we assume that the holes are free particles confined to a crystal with side lengths L. From Bloch's theorem, we know that the wavefunction may be expressed as:

$$\psi_{\mathbf{k}}(\mathbf{r}) = e^{i\mathbf{k}\cdot\mathbf{r}} u_{\mathbf{k}}(\mathbf{r}) \tag{B.30}$$

$$k_x L = 2\pi n_x \tag{B.31}$$

$$k_y L = 2\pi n_y \tag{B.32}$$

$$k_z L = 2\pi n_z \tag{B.33}$$

$$n = \ldots, -2, -1, 0, 1, 2, \ldots \tag{B.34}$$

with the stipulation that **k** must obey periodic boundary conditions with the crystal boundary. From this, we know that in reciprocal space, there is one state per $(2\pi/L)^3$. Using the dispersion relation for a free particle:

$$E_{\mathbf{k}} = \frac{\hbar^2|k|^2}{2m^*} \tag{B.35}$$

From this we can calculate the number of states N within a spherical volume of radius $|k|$. The number must be divided by 8 because we must account for the equivalence of $\pm k_{x,y,z}$ values, which represent a phase shift in the wavefunction but are actually the same state. To account for the spin degeneracy of the states we multiply by two.

$$N = \frac{2}{8}\frac{(4/3)\pi|k|^3}{(2\pi/L)^3} = \frac{V}{3\pi^2}|k|^3 = \frac{V}{3\pi^2}\left(\frac{2m^*E}{\hbar^2}\right)^{3/2} \tag{B.36}$$

Here, V is the volume of the crystal. To get the density of states $DoS(E)$ (per volume) we take the derivative of N with respect to E and divide by V:

$$\begin{aligned}\rho_{v0}(E) = \frac{dN}{dE} &= \frac{1}{2\pi^2}\left(\frac{2m^*}{\hbar^2}\right)^{3/2}\sqrt{E} \\ &= \frac{4\pi(2m^*)^{3/2}}{h^3}\sqrt{E}\end{aligned} \tag{B.37}$$

B.3.1 Dopant DoS Spreading

To approximate the band width of the acceptor impurity states, we use the tight binding model and assume hydrogenic s-like wavefunctions [91] ($\phi_0(r)$) to evaluate the energy transfer integral for states associated with atoms at locations R_i

and R_j.

$$\phi_0(r - R_i) = \sqrt{\frac{\xi^3}{\pi}} \exp(-\xi \left| r - R_i \right|) \tag{B.38}$$

$$\xi = \frac{1}{a_0} \left(\frac{E_A}{E_0} \right)^{1/2} \tag{B.39}$$

$$J\left(\left| R_i - R_j \right| \right) = \int \frac{q^2}{4\pi\epsilon_r\epsilon_0 \left| r - R_i \right|} \phi_0(r - R_i)\phi_0(r - R_j) d^3r \tag{B.40}$$

$$J(R) = \frac{q^2\xi}{4\pi\epsilon_r\epsilon_0}(1 + \xi R) \exp(-\xi R) \tag{B.41}$$

Here, $R = |R_i - R_j|$ is the distance between nearest neighbor dopant atoms, a_0 is the Bohr radius, ξ is the scaled inverse radius for the acceptor state, and E_0 is the ground state energy of the hydrogen atom. Assuming the dopants are uniformly randomly distributed in the crystal (reasonable assumption for a low to moderately doped box-like profile), the probability that the nearest neighbor dopant lies at a distance between R and $R + dR$ from a given dopant is given by an exponential distribution.

$$4\pi N_A \exp\left(-\frac{4}{3}\pi N_A R^3 \right) R^2 dR \tag{B.42}$$

This probability is derived from the Poisson probability distribution of finding m atoms in a volume w with uniform density n (taken from Kane [104]).

$$P(m, w) = \frac{(nw)^m}{m!} e^{-nw} \tag{B.43}$$

Averaging the energy transfer integral weighted by the nearest neighbor distance probability distribution leads to the total bandwidth of the impurity levels

B.

$$\langle J(R)\rangle = \int J(R) 4\pi N_A R^2 \exp\left(-\frac{4}{3}\pi N_A R^3\right) dR \tag{B.44}$$

$$B = 2\,|\langle J(R)\rangle| \tag{B.45}$$

B.4 Compensated Systems

For the case of compensated systems (containing both N_A and N_D concentrations), we must go back to the full charge-neutrality equation.

$$p + N_D^+ = n + N_A^- \tag{B.46}$$

$$p + N_D^+ = n_i^2/p + N_A^- \tag{B.47}$$

$$p^2 + (N_D^+ - N_A^-)p - n_i^2 \tag{B.48}$$

Here, p, N_D^+, and N_A^- are all functions of the unknown Fermi level E_F:

$$p = \int_{-\infty}^{E_V} \frac{\rho_V(E)}{1 + \exp\left(\frac{E_F - E}{k_B T}\right)} dE \tag{B.49}$$

$$N_A^- = \int_{-\infty}^{\infty} \frac{\rho_A(E)}{1 + g_A \exp\left(\frac{E - E_F}{k_B T}\right)} dE \tag{B.50}$$

$$N_D^+ = \int_{-\infty}^{\infty} \frac{\rho_D(E)}{1 + g_D \exp\left(\frac{E_F - E}{k_B T}\right)} dE \tag{B.51}$$

Here, $\rho_V(E)$, $\rho_A(E)$, and $\rho_D(E)$ are the valence band, acceptor, and donor density of states. As before, this equation can be solved using the quadratic formula for p. When these integrals are substituted into Equation B.48, it can be rewritten such

that only two integrals need to be solved for each iteration of the numerical solution.

$$p(E_F) = \frac{-D^*(E_F) + \sqrt{(D^*(E_F))^2 + 4n_i^2}}{2} \tag{B.52}$$

$$D^*(E_F) \equiv N_D^+ - N_A^- = \int_{-\infty}^{\infty} \frac{\rho_D(E)}{1 + g_D \exp\left(\frac{E_F - E}{k_B T}\right)} - \frac{\rho_A(E)}{1 + g_A \exp\left(\frac{E - E_F}{k_B T}\right)} dE \tag{B.53}$$

This equation can be solved numerically for E_F by using trapezoidal integration combined with the method of bisection for a given doping N_A and N_D.

Appendix C: Standard Component Mobility Formulations

C.1 Bulk Mobility

Bulk mobility is modeled using the dopant and temperature dependent Caughey-Thomas model described by Equation (C.1) [123].

$$\mu_B = \frac{\mu_{max}(\frac{300}{T})^{\alpha}}{1 + (\frac{D(T)}{N_{ref}})^{\beta}} \tag{C.1}$$

Where the values for bulk mobility parameters are: μ_{max} is 1071 cm^2/Vs; α is 2.4; N_{ref} is 1.9e17 cm^{-3}; and β is 0.4.

C.2 Surface Phonon Mobility

Surface phonons, which partially account for the reduction in MOSFET surface mobility, are calculated using the acoustic phonon deformation potential and surface field. The analytical form is described by Equation (C.2) [148], where ρ_{bulk} is the bulk material density of SiC; v_s is the velocity of sound in SiC; m^*, m_c, $m_\perp$ are the (2D) density of states, conductivity, and perpendicular effective masses, respectively; D_{ac} is the acoustic phonon deformation potential; e is the elementary charge; $\hbar$ is

the reduced Planck's constant; and k_B is Boltzmann's constant.

$$\mu_{SP} = \frac{A}{F_\perp} + \frac{B}{TF_\perp^{1/3}} \tag{C.2}$$
$$A = \frac{3}{2}\frac{\hbar^3 \rho_{bulk} v_s^2}{m^* m_c D_{ac}^2}$$
$$B = \frac{e\hbar^3 \rho_{bulk} v_s^2}{m^* m_c D_{ac}^2 k_B}\left(\frac{9\hbar^2}{4em_\perp}\right)^{(1/3)}$$

C.3 Combined Empirical Surface Roughness Mobility

The CESRM is described using the analytical fit given in Equation (C.3) [1]. Step roughness in epitaxially grown 4H-SiC miscut 8°from the (0001) plane is on average comprised of bunched steps resulting in an rms roughness height of between 0.38 nm [149] and 3.5 nm [51]. Compared to the single bilayer step height of 0.24 nm it is clear that the surface roughness typically accounted for in literature on this matter is predominantly affected by the large-scale step bunching effects rather than the smaller atomic-scale roughness limit we distinguish in this paper. Experimental measurements performed by Kimoto et al. for 3.5°off-angle wafers confirm that the most probable step consists of 4 Si-C bilayers for the Si-face [150]. For relevant 4H-SiC MOSFETs we use $\Gamma_{SR} = 3.5 \times 10^{12}$ V/s extracted by Potbhare et al. [1,51] In the calculation, Δ is the RMS surface height variation, L is the roughness correlation

length, q_{sc} is the screening wavevector, and α is the scattering angle.

$$\mu_{SR} = \frac{\Gamma_{SR}}{F_{\perp}^2} \tag{C.3}$$

$$\Gamma_{SR} = \left(\frac{\hbar^3}{2m_c m^* e \Delta^2 L^2}\right) \frac{1}{\Omega_{SR}}$$

$$\Omega_{SR} = \int_0^{\pi/2} \frac{\sin^3(\alpha)}{\left(\sin(\alpha) + \frac{q_{sc}}{\sqrt{8m^* k_B T/\hbar^2}}\right)\left(1 + \sin^2(\alpha) L^2 \frac{4m^* k_B T}{\hbar^2}\right)} d\alpha$$

C.4 Coulomb Mobility

Trapped and fixed charges caused by atomic defects at the interface create charged scattering sites which induce a Coulombic scattering effect for the channel electrons. The Coulomb mobility is treated using Equation (C.4) [1] where z is the depth into the device. The parameters for fixed interface sheet charge density N_f, interface trapped sheet charge density N_{it}, surface inversion sheet charge density N_{inv}, and inversion layer depth Z_{av} are given in Table C.1.

Inversion layer charge as a function of surface field was derived from the work of Arnold [2] and matched to the corresponding interface state density calculated by Potbhare et al. [1]. The inversion layer depth Z_{av} was taken to be the expected depth of the electron density using the lowest energy (1^{st}) Airy function solution $\psi_1(z)$. The resulting Coulomb mobilities are a function of z so the values reported in Table 3.3 are evaluated at their corresponding Z_{av}.

$$\mu_C = \frac{16\pi\bar{\epsilon}^2\hbar k_B T}{m^* e^3 (N_f + N_{it}) f(z)} \tag{C.4}$$

$$f(z) = \int_0^{pi/2} \left(1 - \frac{q_{sc}^2}{\frac{8m^* k_B T}{\hbar^2} sin^2(\alpha) + q_{sc}^2}\right) exp\left(-2z\sqrt{\frac{8m^* k_B T}{\hbar^2} sin^2(\alpha) + q_{sc}^2}\right) d\alpha$$

$$q_{sc} = \sqrt{\frac{e^2 N_{inv}}{\epsilon_{SiC} Z_{av} k_B T}}$$

Table C.1: Extrinsic Coulomb Scattering Mobility Parameters [1, 2]

$E_\perp$ $[MV/cm]$	0.1	0.5	1
N_f $[cm^{-2}]$	1.3×10^{12}		
N_{it} $[cm^{-2}]$	1×10^{12}	3.35×10^{12}	3.55×10^{12}
N_{inv} $[cm^{-2}]$	4×10^{10}	1.5×10^{12}	3.65×10^{12}
Z_{av} $[nm]$	3.77	2.21	1.75

Bibliography

[1] Siddharth Potbhare, Neil Goldsman, Gary Pennington, Aivars Lelis, and James M McGarrity. Numerical and experimental characterization of 4 h-silicon carbide lateral metal-oxide-semiconductor field-effect transistor. *Journal of Applied Physics*, 100(4):044515, 2006.

[2] Emil Arnold. Charge-sheet model for silicon carbide inversion layers. *IEEE Transactions on Electron Devices*, 46(3):497–503, 1999.

[3] Shizuo Fujita. Wide-bandgap semiconductor materials: For their full bloom. *Japanese journal of applied physics*, 54(3):030101, 2015.

[4] P.A. Tipler and R.A. Llewellyn. *Modern Physics*. W.H. Freeman and Company, 5 edition, 2008.

[5] Y Umeno, Y Kinoshita, and T Kitamura. Ab initio dft simulation of ideal shear deformation of sic polytypes. *Modelling and Simulation in Materials Science and Engineering*, 15(2):27, 2006.

[6] S. Adachi. *Properties of Group-IV, III-V and II-VI Semiconductors*. John Wiley & Sons, Ltd, 2005.

[7] C Persson and Ulf Lindefelt. Relativistic band structure calculation of cubic and hexagonal sic polytypes. *Journal of Applied Physics*, 82(11):5496–5508, 1997.

[8] Michael E Levinshtein, Sergey L Rumyantsev, and Michael S Shur. *Properties of Advanced Semiconductor Materials: GaN, AIN, InN, BN, SiC, SiGe*. John Wiley & Sons, 2001.

[9] Shahrzad Salemi. *Electronic Structure of SiC/SiO_2 by Density Functional Theory*. PhD thesis, University of Maryland, College Park, 2012.

[10] V. Heera, D. Panknin, and W. Skorupa. p-Type doping of SiC by high dose Al implantation - problems and progress. *Applied Surface Science*, 184(1-4):307–316, 2001.

[11] Imran A Khan and James A Cooper. Measurement of high-field electron transport in silicon carbide. *IEEE Transactions on Electron Devices*, 47(2):269–273, 2000.

[12] GE Stillman, VM Robbins, and N Tabatabaie. Iii-v compound semiconductor devices: Optical detectors. *IEEE Transactions on Electron Devices*, 31(11):1643–1655, 1984.

[13] B Jayant Baliga. Sic power devices: From conception to social impact. In *2016 46th European Solid-State Device Research Conference (ESSDERC)*, pages 192–197. IEEE, 2016.

[14] Devanarayanan Perinthatta Ettisserry. *INTEGRATED MODELING OF RELIABILITY AND PERFORMANCE OF 4H-SILICON CARBIDE POWER MOSFETS USING ATOMISTIC AND DEVICE SIMULATIONS*. PhD thesis, University of Maryland, College Park, 2015.

[15] Anant Agarwal and Sarah Haney. Some critical materials and processing issues in sic power devices. *Journal of Electronic Materials*, 37(5):646–654, 2008.

[16] Karl E Spear and John P Dismukes. *Synthetic diamond: emerging CVD science and technology*, volume 25. John Wiley & Sons, 1994.

[17] Robert Eisberg and Robert Resnick. Quantum physics of atoms, molecules, solids, nuclei, and particles. *Quantum Physics of Atoms, Molecules, Solids, Nuclei, and Particles, 2nd Edition, by Robert Eisberg, Robert Resnick, pp. 864. ISBN 0-471-87373-X. Wiley-VCH, January 1985.*, page 864, 1985.

[18] R. Serway, C. Moses, and C. Moyer. *Modern Physics*. Thomson Brooks, 5 edition, 2005.

[19] Hangseok Choi et al. Overview of silicon carbide power devices. *Fairchild semiconductor*, 2016.

[20] Robert K Willardson and Eicke R Weber. *SiC materials and devices*, volume 52. Academic Press, 1998.

[21] Yole Developpement. Sic, gan and other wider-bandgap materials present new choices for power electronics. *Market Focus: Power Electronics 91*, 9(8), 2015.

[22] Gang Liu, Blair R Tuttle, and Sarit Dhar. Silicon carbide: A unique platform for metal-oxide-semiconductor physics. *Applied Physics Reviews*, 2(2):021307, 2015.

[23] Lijuan Li, Canbing Li, Yijia Cao, and Feng Wang. Recent progress of sic power devices and applications. *IEEJ Transactions on Electrical and Electronic Engineering*, 8(5):515–521, 2013.

[24] Tristan Evans, Toshio Hanada, Yuki Nakano, and Takashi Nakamura. Development of sic power devices and modules for automotive motor drive use. In *2013 IEEE International Meeting for Future of Electron Devices, Kansai*, pages 116–117. IEEE, 2013.

[25] Wai-Kai Chen. *VLSI Handbook Second Edition*. Taylor & Francis Group, 2007.

[26] Takahide Umeda, Mitsuo Okamoto, Ryouji Kosugi, Shinsuke Harada, Ryo Arai, Yoshihiro Sato, Takahiro Makino, and Takeshi Ohshima. Sic mos interface states: Difference between si face and c face. *ECS Transactions*, 58(7):55–60, 2013.

[27] Siddharth Potbhare. *Modeling and characterization of 4H-SiC MOSFETS: High field, high temperature, and transient effects*. PhD thesis, University of Maryland, College Park, 2008.

[28] J. Fan and P.K. Chu. Silicon Carbide Nanostructures. *Engineering Materials and Process*, 2014.

[29] Subal Sahni. *Highly integrated Germanium Photo-detectors and III-V Hybrid Lasers for Silicon Photonic Applications*. PhD thesis, University of California Los Angeles, 2007.

[30] Paolo Giannozzi, Stefano Baroni, Nicola Bonini, Matteo Calandra, Roberto Car, Carlo Cavazzoni, Davide Ceresoli, Guido L Chiarotti, Matteo Cococcioni, Ismaila Dabo, Andrea Dal Corso, Stefano de Gironcoli, Stefano Fabris, Guido Fratesi, Ralph Gebauer, Uwe Gerstmann, Christos Gougoussis, Anton Kokalj, Michele Lazzeri, Layla Martin-Samos, Nicola Marzari, Francesco Mauri, Riccardo Mazzarello, Stefano Paolini, Alfredo Pasquarello, Lorenzo Paulatto, Carlo Sbraccia, Sandro Scandolo, Gabriele Sclauzero, Ari P Seitsonen, Alexander Smogunov, Paolo Umari, and Renata M Wentzcovitch. Quantum espresso: a modular and open-source software project for quantum simulations of materials. *Journal of Physics: Condensed Matter*, 21(39):395502 (19pp), 2009.

[31] Robert O Jones. Density functional theory: Its origins, rise to prominence, and future. *Reviews of modern physics*, 87(3):897, 2015.

[32] Douglas R Hartree. The wave mechanics of an atom with a non-coulomb central field. part i. theory and methods. In *Mathematical Proceedings of the Cambridge Philosophical Society*, volume 24, pages 89–110. Cambridge University Press, 1928.

[33] Vladimir Fock. Näherungsmethode zur lösung des quantenmechanischen mehrkörperproblems. *Zeitschrift für Physik*, 61(1-2):126–148, 1930.

[34] John C Slater. Note on hartree's method. *Physical Review*, 35(2):210, 1930.

[35] John P Perdew, Kieron Burke, and Matthias Ernzerhof. Generalized gradient approximation made simple. *Physical review letters*, 77(18):3865, 1996.

[36] John P Perdew. Density functional theory and the band gap problem. *International Journal of Quantum Chemistry*, 28(S19):497–523, 1985.

[37] D Volm, BK Meyer, DM Hofmann, WM Chen, NT Son, C Persson, Ulf Lindefelt, O Kordina, E Sörman, AO Konstantinov, et al. Determination of the electron effective-mass tensor in 4h sic. *Physical Review B*, 53(23):15409, 1996.

[38] P. Friedrichs, T. Kimoto, L. Ley, and G. Pensl. Silicon carbide volume 2: Power devices and sensors, 2009.

[39] G Pennington and N Goldsman. Simulation of electron transport in (0001) and $(11\bar{2}0)$ 4H-SiC inversion layers. *Journal of Applied Physics*, 106(6):063701, 2009.

[40] Mats Hjelm. *Monte Carlo simulations of homogeneous and inhomogeneous transport in silicon carbide*. PhD thesis, Royal Institute of Technology, Sweden, 2004.

[41] Mats Hjelm, Hans-Erik Nilsson, A Martinez, KF Brennan, and E Bellotti. Monte carlo study of high-field carrier transport in 4h-sic including band-to-band tunneling. *Journal of applied physics*, 93(2):1099–1107, 2003.

[42] Carlo Jacoboni and Lino Reggiani. The monte carlo method for the solution of charge transport in semiconductors with applications to covalent materials. *Reviews of modern Physics*, 55(3):645, 1983.

[43] Carlo Jacoboni and Paolo Lugli. *The Monte Carlo method for semiconductor device simulation*. SSprinter-Verlag, Vienna, Austria, 1989.

[44] Shinya Yamakawa, Hiroaki Ueno, Kenji Taniguchi, Chihiro Hamaguchi, Kazuo Miyatsuji, Kazuo Masaki, and Umberto Ravaioli. Study of interface roughness dependence of electron mobility in si inversion layers using the monte carlo method. *Journal of applied physics*, 79(2):911–916, 1996.

[45] Wolfgang J Choyke, Hiroyuki Matsunami, and Gerhard Pensl. *Silicon carbide: recent major advances*, volume 1. Springer Science & Business Media, 2013.

[46] SM Goodnick, DK Ferry, CW Wilmsen, Z Liliental, D Fathy, and OL Krivanek. Surface roughness at the si (100)-sio 2 interface. *Physical Review B*, 32(12):8171, 1985.

[47] Tsuneya Ando, Alan B Fowler, and Frank Stern. Electronic properties of two-dimensional systems. *Reviews of Modern Physics*, 54(2):437, 1982.

[48] L Farhang Matin, H Hasan Bouzari, and F Ahmadi. Solving schrodinger equation specializing to the stark effect in linear potential by the canonical function method. *Journal of Theoretical and Applied Physics*, 8(3):140, 2014.

[49] SM Goodnick, DK Ferry, CW Wilmsen, Z Liliental, D Fathy, and OL Krivanek. Surface roughness at the Si (100)-SiO2 interface. *Physical Review B*, 32(12):8171, 1985.

[50] Han Fu, KV Reich, and BI Shklovskii. Surface roughness scattering in multisubband accumulation layers. *Physical Review B*, 93(23):235312, 2016.

[51] Siddharth Potbhare, Neil Goldsman, Aivars Lelis, James M McGarrity, F Barry McLean, and Daniel Habersat. A physical model of high temperature 4H-SiC MOSFETs. *IEEE Transactions on Electron devices*, 55(8):2029–2040, 2008.

[52] Viktoryia Uhnevionak, Alexander Burenkov, Christian Strenger, Guillermo Ortiz, Elena Bedel-Pereira, Vincent Mortet, Fuccio Cristiano, Anton J Bauer, and Peter Pichler. Comprehensive study of the electron scattering mechanisms in 4H-SiC MOSFETs. *IEEE Transactions on Electron Devices*, 62(8):2562–2570, 2015.

[53] K Kojima, H Okumura, S Kuroda, and K Arai. Homoepitaxial growth of 4H-SiC on on-axis (0001) C-face substrates by chemical vapor depositon. *Journal of crystal growth*, 269(2-4):367–376, 2004.

[54] J Hassan, JP Bergman, A Henry, and E Janzén. On-axis homoepitaxial growth on Si-face 4H–SiC substrates. *Journal of Crystal Growth*, 310(20):4424–4429, 2008.

[55] Stefano Leone, Franziska C Beyer, Henrik Pedersen, Olof Kordina, Anne Henry, and Erik Janzén. High growth rate of 4H-SiC epilayers on on-axis substrates with different chlorinated precursors. *Crystal Growth & Design*, 10(12):5334–5340, 2010.

[56] Yasuto Hijikata, Hiroyuki Yaguchi, Sadafumi Yoshida, Y Takata, K Kobayashi, H Nohira, and T Hattori. Off-Angle dependence of characteristics of 4H-SiC-Oxide interfaces. In *Materials science forum*, volume 527, pages 1003–1006. Trans Tech Publ, 2006.

[57] Kenji Fukuda, Makoto Kato, Shinsuke Harada, and Kazutoshi Kojima. High inversion channel mobility of 4H-SiC MOSFETs fabricated on c (000-1) epitaxial substrate with vicinal (below 1^{o}) off-angle. In *Materials science forum*, volume 527, pages 1043–1046. Trans Tech Publ, 2006.

[58] Shinsuke Harada, Sachiko Ito, Makoto Kato, Akio Takatsuka, Kazutoshi Kojima, Kenji Fukuda, and Hajime Okumura. Isotropic channel mobility in UMOSFETs on 4H-SiC C-face with vicinal off-angle. In *Materials Science Forum*, volume 645, pages 999–1004. Trans Tech Publ, 2010.

[59] Hiroshi Yano, H Nakao, Tomoaki Hatayama, Yukiharu Uraoka, and Takashi Fuyuki. Increased channel mobility in 4h-sic UMOSFETs using on-axis substrates. In *Materials science forum*, volume 556, pages 807–810. Trans Tech Publ, 2007.

[60] T Kimoto and J.A. Cooper. *Appendix A: Incomplete Dopant Ionization in 4H-SiC*, pages 511–515. John Wiley & Sons, Ltd, 2014.

[61] Yu.A. Vodakov, E.N. Mokhov, M.G. Ramm, and A.D. Roenkov. Doping peculiarities of SiC epitaxial layers grown by sublimation sandwich-method. In *Springer Proc. Phys*, volume 56, pages 329–334, 1992.

[62] Yu.A. Vodakov, E.N. Mokhov, R.C. Marshall, J.W. Faust, and C.E. Ryan. Silicon Carbide, 1973. *University of South Carolina Press, Columbia, SC*, pages 508–19, 1974.

[63] Y.M. Tairov and Y.A. Vodakov. Group IV materials (mainly SiC). In J.I. Pankove, editor, *Electroluminescence*, pages 31–61. Springer Berlin Heidelberg, 1977.

[64] M.K. Linnarsson, U. Zimmermann, J. Wong-Leung, A. Schöner, M.S. Janson, C. Jagadish, and B.G. Svensson. Solubility limits of dopants in 4H–SiC. *Applied Surface Science*, 203:427–432, 2003.

[65] M.V. Rao, J.B. Tucker, M.C. Ridgway, O.W. Holland, N. Papanicolaou, and J. Mittereder. Ion-implantation in bulk semi-insulating 4H–SiC. *Journal of Applied Physics*, 86(2):752–758, 1999.

[66] T. Troffer, M. Schadt, T. Frank, H. Itoh, G. Pensl, J. Heindl, H.P. Strunk, and M. Maier. Doping of SiC by Implantation of Boron and Aluminum. *Physica Status Solidi (a)*, 162(1):277–298, 1997.

[67] I.G. Atabaev, Kh.N. Juraev, and M.U. Hajiev. Spectral Dependence of Optical Absorption of 4H-SiC Doped with Boron and Aluminum. *Journal of Spectroscopy*, 2018, 2018.

[68] J. Lutz, H. Schlangenotto, U. Scheuermann, and R. De Doncker. *Semiconductor Power Devices Physics, Characteristics, Reliability*. Springer International Publishing, 2 edition, 2018.

[69] S. Greulich-Weber. EPR and ENDOR Investigations of Shallow Impurities in SiC Polytypes. *Physica Status Solidi (a)*, 162(1):95–151, 1997.

[70] M. Ikeda, H. Matsunami, and T. Tanaka. Site effect on the impurity levels in 4H, 6H, and 15R SiC. *Physical Review B*, 22:2842, 09 1980.

[71] T Kimoto and J.A. Cooper. *Appendix C: Major Physical Properties of Common SiC Polytypes*, pages 521–524. John Wiley & Sons, Ltd, 2014.

[72] M. Bakowski, U. Gustafsson, and U. Lindefelt. Simulation of SiC high power devices. *Physica Status Solidi (a)*, 162(1):421–440, 1997.

[73] S.G. Sridhara, L.L. Clemen, R.P. Devaty, W.J. Choyke, D.J. Larkin, H.S. Kong, T. Troffer, and G. Pensl. Photoluminescence and transport studies of boron in 4H SiC. *Journal of Applied Physics*, 83(12):7909–7919, 1998.

[74] T. Troffer, C. Häßler, G. Pensl, K. Hölzlein, H. Mitlehner, and J. Völkl. Boron-related defect centers in 4H silicon carbide. In *International Conference on Silicon Carbide and Related Materials 1995*, number 142, pages 281–284. IOP Publishing Ltd., 1996.

[75] A.A. Lebedev. Deep level centers in silicon carbide: A review. *Semiconductors*, 33(2):107–130, 1999.

[76] S.G. Sridhara, L.L. Clemen, R.P. Devaty, W.J. Choyke, D.J. Larkin, H.S. Kong, T. Troffer, and G. Pensl. Photoluminescence and transport studies of boron in 4H SiC. *Journal of Applied Physics*, 83(12):7909–7919, 1998.

[77] M.M. Anikin, A. Lebedev, A.L. Syrkin, and A.V. Suvorov. Investigation of deep levels in SiC by capacitance spectroscopy methods. *Soviet Physics of Semiconductors*, 19(1):69–71, 1985.

[78] T. Troffer, G. Pensl, A. Schöner, A. Henry, C. Hallin, O. Kordina, and E. Janzén. Electrical characterization of the gallium acceptor in 4H-and 6H-SiC. *Materials Science Forum*, 264:557–560, 1998.

[79] G.L. Harris and INSPEC (Information service). *Properties of Silicon Carbide*. EMIS Datareviews Series. INSPEC, Institution of Electrical Engineers, 1995.

[80] A.-B. Chen and P. Srichaikul. Shallow Donor Levels and the Conduction Band Edge Structures in Polytypes of SiC. *Physica Status Solidi (b)*, 202(1):81–106, 1997.

[81] S. Kagamihara, H. Matsuura, T. Hatakeyama, T. Watanabe, M. Kushibe, T. Shinohe, and K. Arai. Parameters required to simulate electric characteristics of SiC devices for n-type 4HSiC. *Journal of Applied Physics*, 96(10):5601–5606, 2004.

[82] A.O. Evwaraye, S.R. Smith, and W.C. Mitchel. Shallow and deep levels in ntype 4HSiC. *Journal of Applied Physics*, 79(10):7726–7730, 1996.

[83] T. Kimoto, A. Itoh, H. Matsunami, S. Sridhara, L. L. Clemen, R. P. Devaty, W. J. Choyke, T. Dalibor, C. Peppermller, and G. Pensl. Nitrogen donors and deep levels in highquality 4HSiC epilayers grown by chemical vapor deposition. *Applied Physics Letters*, 67(19):2833–2835, 1995.

[84] W. Götz, A. Schöner, G. Pensl, W. Suttrop, W. J. Choyke, R. Stein, and S. Leibenzeder. Nitrogen donors in 4Hsilicon carbide. *Journal of Applied Physics*, 73(7):3332–3338, 1993.

[85] N. Donato and F. Udrea. Static and Dynamic Effects of the Incomplete Ionization in Superjunction Devices. *IEEE Transactions on Electron Devices*, 65(10):4469–4475, 2018.

[86] M. Laube, F. Schmid, G. Pensl, G. Wagner, M. Linnarsson, and M. Maier. Electrical activation of high concentrations of N+ and P+ ions implanted into 4HSiC. *Journal of Applied Physics*, 92(1):549–554, 2002.

[87] R. Wang, I.B. Bhat, and T.P. Chow. Epitaxial growth of n-type SiC using phosphine and nitrogen as the precursors. *Journal of Applied Physics*, 92(12):7587–7592, 2002.

[88] S. Rao, T.P. Chow, and I. Bhat. Dependence of the Ionization Energy of Phosphorous Donor in 4H-SiC on Doping Concentration. *Materials Science Forum*, 527-529:597–600, 01 2006.

[89] S.M. Sze and K.K. Ng. *Physics of Semiconductor Devices*. John Wiley & Sons, 2006.

[90] G.W. Neudeck and R.F. Pierret. *Advanced Semiconductor Fundamentals*. Pearson Education, New York, 2003.

[91] H. Brooks. Theory of the Electrical Properties of Germanium and Silicon. volume 7 of *Advances in Electronics and Electron Physics*, pages 85 – 182. Academic Press, 1955.

[92] E.F. Schubert. *Doping in III-V Semiconductors*. Cambridge University Press, 1993.

[93] H. Ikeda and F. Salleh. Influence of heavy doping on Seebeck coefficient in silicon-on-insulator. *Applied Physics Letters*, 96(1):012106, 2010.

[94] D.S. Lee and J.G. Fossum. Energy-Band Distortion in Highly Doped Silicon. *IEEE Transactions on Electron Devices*, 30(6):626–634, 1983.

[95] J.R. Lowney, A.H. Kahn, J.L. Blue, and C.L. Wilson. Disappearance of impurity levels in silicon and germanium due to screening. *Journal of Applied Physics*, 52(6):4075–4080, 1981.

[96] A. Schenk, P.P. Altermatt, and B. Schmithusen. Physical Model of Incomplete Ionization for Silicon Device Simulation. In *2006 International Conference on Simulation of Semiconductor Processes and Devices*, pages 51–54. IEEE, Sep. 2006.

[97] P.P. Altermatt, A. Schenk, and G. Heiser. A simulation model for the density of states and for incomplete ionization in crystalline silicon. I. Establishing the model in Si: P. *Journal of Applied Physics*, 100(11):113714, 2006.

[98] P.P. Altermatt, A. Schenk, and G. Heiser. A simulation model for the density of states and for incomplete ionization in crystalline silicon. II. Investigation of Si:As and Si:B and usage in device simulation. *Journal of Applied Physics*, 100(11):113715, 2006.

[99] V.I. Fistul. *Heavily Doped Semiconductors*. Plenum Press, New York, 1969.

[100] T.F. Lee and T.C. McGill. Variation of impurity-to-band activation energies with impurity density. *Journal of Applied Physics*, 46(1):373–380, 1975.

[101] I.G. Ivanov, A. Henry, and E. Janzén. Ionization energies of phosphorus and nitrogen donors and aluminum acceptors in 4H silicon carbide from the donor-acceptor pair emission. *Physical Review B*, 71:241201, Jun 2005.

[102] A. Parisini and R. Nipoti. Analysis of the hole transport through valence band states in heavy Al doped 4H-SiC by ion implantation. *Journal of Applied Physics*, 114(24):243703, 2013.

[103] G. Pensl and W.J. Choyke. Electrical and optical characterization of SiC. *Physica B: Condensed Matter*, 185(1-4):264–283, 1993.

[104] E.O. Kane. Thomas-Fermi Approach to Impure Semiconductor Band Structure. *Physical Review*, 131(1):79, 1963.

[105] T.N. Morgan. Broadening of Impurity Bands in Heavily Doped Semiconductors. *Physical Review*, 139(1A):A343, 1965.

[106] A.L. Efros. Electron localization in disordered systems (the anderson transition). *Soviet Physics Uspekhi*, 21(9):746, 1978.

[107] G. Busch and H. Labhart. Über den Mechanismus der elektrischen Leitfähigkeit des Siliciumcarbids. *Helvetica Physica Acta*, 19:463, 1946.

[108] W. Kuźmicz. Ionization of impurities in silicon. *Solid-State Electronics*, 29(12):1223–1227, 1986.

[109] S. Asada, T. Okuda, T. Kimoto, and J. Suda. Hall scattering factors in p-type 4H-SiC with various doping concentrations. *Applied Physics Express*, 9(4):041301, mar 2016.

[110] H. Matsuura, K. Sugiyama, K. Nishikawa, T. Nagata, and N. Fukunaga. Occupation probability for acceptor in Al-implanted p-type 4HSiC. *Journal of Applied Physics*, 94(4):2234–2241, 2003.

[111] H. Matsuura. The influence of excited states of deep dopants on majority-carrier concentration in a wide-bandgap semiconductor. *New Journal of Physics*, 4:12–12, mar 2002.

[112] A. Koizumi, J. Suda, and T. Kimoto. Temperature and doping dependencies of electrical properties in Al-doped 4H-SiC epitaxial layers. *Journal of Applied Physics*, 106(1):013716, 2009.

[113] A. Koizumi, N. Iwamoto, S. Onoda, T. Ohshima, T. Kimoto, K. Uchida, and S. Nozaki. Compensation-dependent carrier transport of Al-doped p-type 4H-SiC. In *Materials Science Forum*, volume 679, pages 201–204. Trans Tech Publ, 2011.

[114] H. Tanaka, S. Asada, T. Kimoto, and J. Suda. Theoretical analysis of Hall factor and hole mobility in p-type 4H-SiC considering anisotropic valence band structure. *Journal of Applied Physics*, 123(24):245704, 2018.

[115] M. Ruff, H. Mitlehner, and R. Helbig. SiC Devices: Physics and Numerical Simulation. *IEEE Transactions on Electron Devices*, 41(6):1040–1054, 1994.

[116] L. Kasamakova-Kolaklieva, L. Storasta, I. Ivanov, B. Magnusson, S. Contreras, C. Consejo, J. Pernot, M. Zielinski, and E. Janzén. Temperature-Dependent Hall Effect Measurements in Low Compensated p-Type 4H-SiC. *Materials Science Forum*, 457-460:677–680, 2004.

[117] H. Matsuura, M. Komeda, S. Kagamihara, H. Iwata, R. Ishihara, T. Hatakeyama, T. Watanabe, K. Kojima, T. Shinohe, and K. Arai. Dependence of acceptor levels and hole mobility on acceptor density and temperature in Al-doped p-type 4H-SiC epilayers. *Journal of Applied Physics*, 96(5):2708–2715, 2004.

[118] G. Wagner, W. Leitenberger, K. Irmscher, F. Schmid, M. Laube, and G. Pensl. Aluminum Incorporation into 4H-SiC Layers during Epitaxial Growth in a Hot-Wall CVD System. *Materials Science Forum*, 389-393:207–210, 01 2002.

[119] T. Troffer, M. Schadt, T. Frank, H. Itoh, G. Pensl, J. Heindl, H. P. Strunk, and M. Maier. Doping of SiC by Implantation of Boron and Aluminum. *Physica Status Solidi (a)*, 162(1):277–298, 1997.

[120] R. Nipoti, R. Scaburri, A. Hallén, and A. Parisini. Conventional thermal annealing for a more efficient p-type doping of Al implanted 4H-SiC. *Journal of Materials Research*, 28(1):1722, 2013.

[121] H. Fujihara, J. Suda, and T. Kimoto. Electrical properties of n- and p-type 4H-SiC formed by ion implantation into high-purity semi-insulating substrates. *Japanese Journal of Applied Physics*, 56(7):070306, jun 2017.

[122] Y. Negoro, T. Kimoto, H. Matsunami, F. Schmid, and G. Pensl. Electrical activation of high-concentration aluminum implanted in 4H-SiC. *Journal of Applied Physics*, 96(9):4916–4922, 2004.

[123] D.M. Caughey and R.E. Thomas. Carrier Mobilities in Silicon Empirically Related to Doping and Field. *Proceedings of the IEEE*, 55(12):2192–2193, 1967.

[124] D. Stefanakis and K. Zekentes. TCAD models of the temperature and doping dependence of the bandgap and low field carrier mobility in 4H-SiC. *Microelectronic Engineering*, 116:65–71, 2014.

[125] M. Roschke and F. Schwierz. Electron mobility models for 4H, 6H, and 3C SiC [MESFETs]. *IEEE Transactions on Electron Devices*, 48(7):1442–1447, 2001.

[126] W.J. Schaffer, G.H. Negley, K.G. Irvine, and J.W. Palmour. Conductivity Anisotropy in Epitaxial 6H and 4H SiC. *MRS Proceedings*, 339:595, 1994.

[127] E. McIrvine. Phenomenology of impurity conduction in semiconductors. *Journal of Physics and Chemistry of Solids*, 15:356–358, 1960.

[128] H. Matsuura, A. Takeshita, T. Imamura, K. Takano, K. Okuda, A. Hidaka, S. Ji, K. Eto, K. Kojima, T. Kato, S. Yoshida, and H. Okumura. Dependence of conduction mechanisms in heavily Al-doped 4H-SiC epilayers on Al concentration. *Applied Physics Express*, 11(10):101302, 2018.

[129] R.M. Hill. Variable-Range Hopping. *Physica Status Solidi (a)*, 34(2):601–613, 1976.

[130] M.K. Linnarsson, M.S. Janson, U. Zimmermann, B.G. Svensson, P.O.Å. Persson, L. Hultman, J. Wong-Leung, S. Karlsson, A. Schöner, H. Bleichner, and E. Olsson. Solubility limit and precipitate formation in Al-doped 4H-SiC epitaxial material. *Applied Physics Letters*, 79(13):2016–2018, 2001.

[131] M.K. Linnarsson, P.O.Å. Persson, H. Bleichner, M.S. Janson, U. Zimmermann, H. Andersson, S. Karlsson, R. Yakimova, L. Hultman, and B.G. Svensson. Precipitate formation in heavily Al-doped 4H-SiC layers. In *Materials Science Forum*, volume 353, pages 583–586. Trans Tech Publications Ltd., Zurich-Uetikon, Switzerland, 2001.

[132] Kazutaka Tomizawa. *Numerical Simulation of Submicron Semiconductor Devices*. Artech House, 1993.

[133] Hongchin Lin and Neil Goldsman. An efficient solution of the boltzmann transport equation which includes the pauli exclusion principle. *Solid-state electronics*, 34(10):1035–1048, 1991.

[134] Hongchin Lin, Neil Goldsman, and ID Mayergoyz. An efficient deterministic solution of the space-dependent boltzmann transport equation for silicon. *Solid-state electronics*, 35(1):33–42, 1992.

[135] V.V. Afanasev, M. Bassler, G. Pensl, M.J. Schulz, and E. Stein von Kamienski. Band offsets and electronic structure of sic/sio2 interfaces. *Journal of Applied Physics*, 79(6):3108–3114, 1996.

[136] Jenny Nelson. *The Physics of Solar Cells*. World Scientific Publishing Company, 2003.

[137] David S Sukhdeo, Hai Lin, Donguk Nam, Ze Yuan, Boris M Vulovic, Suyog Gupta, James S Harris, Birendra Dutt, and Krishna C Saraswat. Approaches for a viable germanium laser: tensile strain, gesn alloys, and n-type doping. In *2013 Optical Interconnects Conference*, pages 112–113. IEEE, 2013.

[138] S Gupta. *Germanium-Tin (GeSn) Technology*. PhD thesis, Stanford University, California, 2013.

[139] Suyog Gupta, Blanka Magyari-Köpe, Yoshio Nishi, and Krishna C Saraswat. Achieving direct band gap in germanium through integration of sn alloying and external strain. *Journal of Applied Physics*, 113(7):073707, 2013.

[140] Pairot Moontragoon, Zoran Ikonić, and Paul Harrison. Band structure calculations of si–ge–sn alloys: achieving direct band gap materials. *Semiconductor science and technology*, 22(7):742, 2007.

[141] Suyog Gupta, Blanka Magyari-Köpe, Yoshio Nishi, and Krishna C Saraswat. Band structure and ballistic electron transport simulations in gesn alloys. *SISPAD*, 2012.

[142] Philipp Haas, Fabien Tran, and Peter Blaha. Calculation of the lattice constant of solids with semilocal functionals. *Physical Review B*, 79(8):085104, 2009.

[143] Andrea Dal Corso. A pseudopotential plane waves program (pwscf) and some case studies. In *Quantum-Mechanical Ab-initio Calculation of the Properties of Crystalline Materials*, pages 155–178. Springer, 1996.

[144] Lianhua He, Fang Liu, Geoffroy Hautier, Micael JT Oliveira, Miguel AL Marques, Fernando D Vila, JJ Rehr, G-M Rignanese, and Aihui Zhou. Accuracy of generalized gradient approximation functionals for density-functional perturbation theory calculations. *Physical Review B*, 89(6):064305, 2014.

[145] Nandor L Balàzs. Formation of stable molecules within the statistical theory of atoms. *Physical Review*, 156(1):42, 1967.

[146] Nikita S Shah. *Ab Initio Molecular Dynamics Calculation Of Vibrational Properties Of Refractory Carbides*. PhD thesis, Bhavnagar, 2013.

[147] Pierre Hohenberg and Walter Kohn. Inhomogeneous electron gas. *Physical review*, 136(3B):B864, 1964.

[148] Claudio Lombardi, Stefano Manzini, Antonio Saporito, and Massimo Vanzi. A physically based mobility model for numerical simulation of nonplanar devices. *IEEE Transactions on Computer-Aided Design of Integrated Circuits and Systems*, 7(11):1164–1171, 1988.

[149] Gary Pennington, Siddharth Potbhare, Neil Goldsman, James M McGarrity, and Aivars Lelis. Impact of surface steps on the roughness mobility in 4h-sic. In *Semiconductor Device Research Symposium, 2005 International*, pages 143–144. IEEE, 2005.

[150] Tsunenobu Kimoto, Akira Itoh, Hiroyuki Matsunami, and Tetsuyuki Okano. Step bunching mechanism in chemical vapor deposition of 6H–and 4H–SiC {0001}. *Journal of Applied Physics*, 81(8):3494–3500, 1997.

[151] N.S. Saks, A.K. Agarwal, S.H. Ryu, and J.W. Palmour. Low-dose aluminum and boron implants in 4H and 6H silicon carbide. *Journal of Applied Physics*, 90(6):2796–2805, 2001.

[152] E.M. Handy, M.V. Rao, O.W. Holland, P.H. Chi, K.A. Jones, M.A. Derenge, R.D. Vispute, and T. Venkatesan. Al, B, and Ga ion-implantation doping of SiC. *Journal of Electronic Materials*, 29(11):1340–1345, 2000.

[153] M. Ikeda, H. Matsunami, and T. Tanaka. Site effect on the impurity levels in 4H, 6H, and 15R SiC. *Physical Review B*, 22(6):2842, 1980.

[154] S.S. Li and W.R. Thurber. The dopant density and temperature dependence of electron mobility and resistivity in n-type silicon. *Solid-State Electronics*, 20(7):609–616, 1977.

[155] S.R. Smith, A.O. Evwaraye, W.C. Mitchel, and M.A. Capano. Shallow acceptor levels in 4h- and 6h-sic. *Journal of Electronic Materials*, 28(3):190–195, Mar 1999.

[156] I.G. Ivanov, B. Magnusson, and E. Janzén. Analysis of the sharp donor-acceptor pair luminescence in 4H-SiC doped with nitrogen and aluminum. *Physical Review B*, 67:165211, Apr 2003.

[157] H. Matsuura, K. Aso, S. Kagamihara, H. Iwata, T. Ishida, and K. Nishikawa. Decrease in Al acceptor density in Al-doped 4H-SiC by irradiation with 4.6 MeV electrons. *Applied Physics Letters*, 83(24):4981–4983, 2003.

[158] P. Achatz, J. Pernot, C. Marcenat, J. Kacmarcik, G. Ferro, and E. Bustarret. Doping-induced metal-insulator transition in aluminum-doped 4H silicon carbide. *Applied Physics Letters*, 92(7):072103, 2008.

[159] J. Pernot, S. Contreras, and J. Camassel. Electrical transport properties of aluminum-implanted 4HSiC. *Journal of Applied Physics*, 98(2):023706, 2005.

[160] V. Heera, K.N. Madhusoodanan, W. Skorupa, C. Dubois, and H. Romanus. A comparative study of the electrical properties of heavily Al implanted, single crystalline and nanocrystalline SiC. *Journal of Applied Physics*, 99(12):123716, 2006.

[161] N.I. Kuznetsov and A.S. Zubrilov. Deep centers and electroluminescence in 4H–SiC diodes with a p-type base region. *Materials Science and Engineering: B*, 29(1-3):181–184, 1995.

[162] J.-M. Bluet, J. Pernot, J. Camassel, S. Contreras, J.L. Robert, J.F. Michaud, and T. Billon. Activation of aluminum implanted at high doses in 4H–SiC. *Journal of Applied Physics*, 88(4):1971–1977, 2000.

[163] W. Kaindl, M. Lades, N. Kaminski, E. Niemann, and G. Wachutka. Experimental characterization and numerical simulation of the electrical properties of nitrogen, aluminum, and boron in 4H/6H-SiC. *Journal of Electronic Materials*, 28(3):154–160, Mar 1999.

[164] H. Itoh, T. Troffer, and G. Pensl. Coimplantation Effects on the Electrical Properties of Boron and Aluminium Acceptors in 4H-SiC. In *Silicon Carbide, III-Nitrides and Related Materials*, volume 264 of *Materials Science Forum*, pages 685–688. Trans Tech Publications Ltd, 12 1997.

[165] J. Weisse, M. Hauck, T. Sledziewski, M. Tschiesche, M. Krieger, A.J. Bauer, H. Mitlehner, L. Frey, and T. Erlbacher. Analysis of compensation effects in aluminum-implanted 4H-SiC devices. In *Materials Science Forum*, volume 924, pages 184–187. Trans Tech Publ, 2018.

[166] W.J. Schaffer, H.S. Kong, G.H. Negley, and J.W. Palmour. Hall effect and CV measurements on epitaxial 6H- and 4H-SiC. *Institute of Physics Conference Series*, 137:155–159, 1994.

[167] N.S. Saks, A.V. Suvorov, and D.C. Capell. High temperature high-dose implantation of aluminum in 4H-SiC. *Applied Physics Letters*, 84(25):5195–5197, 2004.

[168] G.A. Lomakina, Yu.A. Vodakov, E.N. Mokhov, V.G. Oding, and Kholuyan. G.F. Comparative Study of the Electrical Properties of Three Polytypes of Silicon Carbide. *Soviet Physics Solid State*, 12(10):2356–2359, 1971.

[169] I.R. Arvinte. *Investigation of dopant incorporation in silicon carbide epilayers grown by chemical vapor deposition.* PhD thesis, Universite Côte d'Azur, 11 2016.

[170] F. Schmid, M. Krieger, M. Laube, G. Pensl, and G. Wagner. *Hall Scattering Factor for Electrons and Holes in SiC*, pages 517–536. Springer Berlin Heidelberg, Berlin, Heidelberg, 2004.

[171] S. Ji, K. Kojima, Y. Ishida, H. Tsuchida, S. Yoshida, and H. Okumura. Low Resistivity, Thick Heavily Al-Doped 4H-SiC Epilayers Grown by Hot-Wall Chemical Vapor Deposition. In *Silicon Carbide and Related Materials 2012*, volume 740 of *Materials Science Forum*, pages 181–184. Trans Tech Publications Ltd, 3 2013.

[172] S. Contreras, M. Zielinski, C. Konczewicz, L.and Blanc, S. Juillaguet, R. Müller, U. Künecke, P. Wellmann, and J. Camassel. Results of SIMS, LTPL and temperature-dependent Hall effect measurements performed on Al-doped α-SiC substrates grown by the M-PVT method. *Materials Science Forum*, 527-529:633–636, 2006.

[173] Y. Tanaka, N. Kobayashi, H. Okumura, R. Suzuki, T. Ohdaira, M. Hasegawa, M. Ogura, S. Yoshida, and H. Tanoue. Electrical and Structural Properties of Al and B Implanted 4H-SiC. *Materials Science Forum*, 338-342:909–912, 2000.

[174] M. Obernhofer, M. Krieger, F. Schmid, H.B. Weber, G. Pensl, and A. Schöner. Electrical and Structural Properties of Al-Implanted and Annealed 4H-SiC. In *Silicon Carbide and Related Materials 2006*, volume 556 of *Materials Science Forum*, pages 343–346. Trans Tech Publications Ltd, 8 2007.

[175] P. Kwasnicki. *Evaluation of doping in 4H-SiC by optical spectroscopies*. PhD thesis, Université Montpellier II - Sciences et Techniques du Languedoc, 12 2014.

[176] J. Pernot, J. Camassel, S. Contreras, J.-L. Robert, J.-M. Bluet, J.F. Michaud, and T. Billon. Control of Al-implantation doping in 4H–SiC. *Materials Science and Engineering: B*, 80(1):362 – 365, 2001.

[177] J.-M. Bluet, J. Pernot, T. Billon, S. Contreras, J.F. Michaud, J.-L. Robert, and J. Camassel. Al and Al/C High Dose Implantation in 4H-SiC. In *Silicon Carbide and Related Materials - 1999*, volume 338 of *Materials Science Forum*, pages 885–888. Trans Tech Publications Ltd, 5 2000.

[178] G. Liaugaudas, D. Dargis, P. Kwasnicki, H. Peyre, R. Arvinte, S. Juillaguet, M. Zielinski, and K. Jarasiunas. Optical Characterization of p-Type 4H-SiC Epilayers. *Materials Science Forum*, 821-823:249–252, 06 2015.

[179] S. Asada, J. Suda, and T. Kimoto. Analytical formula for temperature dependence of resistivity in p-type 4H-SiC with wide-range doping concentrations. *Japanese Journal of Applied Physics*, 57(8):088002, jun 2018.

[180] S. Ji, K. Kojima, Y. Ishida, S. Saito, T. Kato, H. Tsuchida, S. Yoshida, and H. Okumura. The growth of low resistivity, heavily Al-doped 4H–SiC thick epilayers by hot-wall chemical vapor deposition. *Journal of Crystal Growth*, 380:85–92, 2013.

[181] M. Rambach, A.J. Bauer, and H. Ryssel. Electrical and topographical characterization of aluminum implanted layers in 4H silicon carbide. *Physica Status Solidi (b)*, 245(7):1315–1326, 2008.

[182] T. Shirai, A. Danno, K.and Seki, H. Sakamoto, and T. Bessho. Solution Growth of p-Type 4H-SiC Bulk Crystals with Low Resistivity. In *Silicon Carbide and Related Materials 2013*, volume 778 of *Materials Science Forum*, pages 75–78. Trans Tech Publications Ltd, 5 2014.

[183] T. Kimoto, H. Yano, S. Tamura, N. Miyamoto, K. Fujihira, Y. Negoro, and H. Matsunami. Recent Progress in SiC Epitaxial Growth and Device Processing Technology. *Materials Science Forum*, 353-356:543–548, 2001.

[184] T. Miyazawa, K. Nakayama, A. Tanaka, K. Asano, S. Ji, K. Kojima, Y. Ishida, and H. Tsuchida. Epitaxial growth and characterization of thick multi-layer 4H-SiC for very high-voltage insulated gate bipolar transistors. *Journal of Applied Physics*, 118(8):085702, 2015.

[185] K. Tone and J.H. Zhao. A comparative study of C plus Al coimplantation and Al implantation in 4H and 6H-SiC. *IEEE Transactions on Electron Devices*, 46:612 – 619, 04 1999.

[186] C. Persson, A.F. da Silva, and B. Johansson. Metal-nonmetal transition in p-type SiC polytypes. *Physical Review B*, 63(20):205119, 2001.